



## 저작자표시-비영리-변경금지 2.0 대한민국

이용자는 아래의 조건을 따르는 경우에 한하여 자유롭게

- 이 저작물을 복제, 배포, 전송, 전시, 공연 및 방송할 수 있습니다.

다음과 같은 조건을 따라야 합니다:



저작자표시. 귀하는 원저작자를 표시하여야 합니다.



비영리. 귀하는 이 저작물을 영리 목적으로 이용할 수 없습니다.



변경금지. 귀하는 이 저작물을 개작, 변형 또는 가공할 수 없습니다.

- 귀하는, 이 저작물의 재이용이나 배포의 경우, 이 저작물에 적용된 이용허락조건을 명확하게 나타내어야 합니다.
- 저작권자로부터 별도의 허가를 받으면 이러한 조건들은 적용되지 않습니다.

저작권법에 따른 이용자의 권리는 위의 내용에 의하여 영향을 받지 않습니다.

이것은 [이용허락규약\(Legal Code\)](#)을 이해하기 쉽게 요약한 것입니다.

[Disclaimer](#)

**M. S. Dissertation**

**SAR Image-Based Detection of Vessels from Machine  
Learning Implementing an Automated Training Data  
Retrieval Algorithm**

훈련 자료 자동 추출 알고리즘과 기계 학습을 통한  
SAR 영상 기반의 선박 탐지

**February 2021**

**Graduate School of Earth and Environmental Sciences  
Seoul National University**

**Juyoung Song**

SAR Image-Based Detection of Vessels from Machine  
Learning Implementing an Automated Training Data  
Retrieval Algorithm

훈련 자료 자동 추출 알고리즘과 기계 학습을 통한  
SAR 영상 기반의 선박 탐지

지도 교수 김 덕 진

이 논문을 이학석사 학위논문으로 제출함

2021 년 2 월

서울대학교 대학원  
자연과학대학 지구환경과학부  
송 주 영

송주영의 이학석사 학위논문을 인준함

2021 년 2 월

위 원 장

조 양 기

(인)

부위원장

김 덕 진

(인)

위 원

임 정 호

(인)

# Abstract

Detection and surveillance of vessels are regarded as a crucial application of SAR for their contribution to the preservation of marine resources and the assurance on maritime safety. Introduction of machine learning to vessel detection significantly enhanced the performance and efficiency of the detection, but a substantial majority of studies focused on modifying the object detector algorithm. As the fundamental enhancement of the detection performance would be nearly impossible without accurate training data of vessels, this study implemented AIS information containing real-time information of vessel's movement in order to propose a robust algorithm which acquires the training data of vessels in an automated manner.

As AIS information was irregularly and discretely obtained, the exact target interpolation time for each vessel was precisely determined, followed by the implementation of Kalman filter, which mitigates the measurement error of AIS sensor. In addition, as the velocity of each vessel renders an imprint inside the SAR image named as Doppler frequency shift, it was calibrated by restoring the elliptic satellite orbit from the satellite state vector and estimating the distance between the satellite and the target vessel. From the calibrated position of the AIS sensor inside the corresponding SAR image, training data was directly obtained via internal allocation of the AIS sensor in each vessel. For fishing boats, separate information system named as VPASS was applied for the identical procedure of training data retrieval.

Training data of vessels obtained via the automated training data procurement algorithm was evaluated by a conventional object detector, for three detection evaluating parameters: precision, recall and F1 score. All three evaluation parameters from the proposed training data acquisition significantly exceeded that from the manual acquisition. The major difference between two training datasets was demonstrated in the inshore regions and in the vicinity of strong scattering vessels in which land artifacts, ships and the ghost signals derived from them were indiscernible by visual inspection. This study additionally introduced a possibility of resolving the unclassified usage of each vessel by comparing AIS information with the accurate vessel detection results.

**Keywords** – SAR, AIS, VPASS, Training data, Machine learning, Vessel detection

**Student Number:** 2019-27567

# List of Contents

<b>Chapter 1. Introduction .....</b>	<b>- 1 -</b>
<b>1.1 Research Background .....</b>	<b>- 1 -</b>
<b>1.2 Research Objective .....</b>	<b>- 8 -</b>
<b>Chapter 2. Data Acquisition .....</b>	<b>- 10 -</b>
<b>2.1 Acquisition of SAR Image Data.....</b>	<b>- 10 -</b>
<b>2.2 Acquisition of AIS and VPASS Information.....</b>	<b>- 20 -</b>
<b>Chapter 3. Methodology on Training Data Procurement.....</b>	<b>- 26 -</b>
<b>3.1 Interpolation of Discrete AIS Data .....</b>	<b>- 29 -</b>
<b>3.1.1 Estimation of Target Interpolation Time for Vessels.....</b>	<b>- 29 -</b>
<b>3.1.2 Application of Kalman Filter to AIS Data .....</b>	<b>- 34 -</b>
<b>3.2 Doppler Frequency Shift Correction .....</b>	<b>- 40 -</b>
<b>3.2.1 Theoretical Basis of Doppler Frequency Shift.....</b>	<b>- 40 -</b>
<b>3.2.2 Mitigation of Doppler Frequency Shift .....</b>	<b>- 48 -</b>
<b>3.3 Retrieval of Training Data of Vessels .....</b>	<b>- 53 -</b>
<b>3.4 Algorithm on Vessel Training Data Acquisition from VPASS         Information.....</b>	<b>- 61 -</b>
<b>Chapter 4. Methodology on Object Detection Architecture .....</b>	<b>- 66 -</b>
<b>Chapter 5. Results.....</b>	<b>- 74 -</b>
<b>5.1 Assessment on Training Data .....</b>	<b>- 74 -</b>
<b>5.2 Assessment on AIS-based Ship Detection.....</b>	<b>- 79 -</b>

5.3	Assessment on VPASS-based Fishing Boat Detection .....	91 -
<b>Chapter 6. Discussions.....</b>		<b>110 -</b>
6.1	Discussion on AIS-Based Ship Detection .....	110 -
6.2	Application on Determining Unclassified Vessels.....	116 -
<b>Chapter 7. Conclusion .....</b>		<b>125 -</b>
국문 요약문 -		128 -
<b>Bibliography -</b>		<b>130 -</b>

# List of figures

Figure 2-1 Spatial coverage of Sentinel-1 and Cosmo-SkyMed SAR data. ....	14 -
Figure 2-2 Illustration on individual maneuvering fashion of AIS sensor-installed vessel. ....	24 -
Figure 2-3 Abridged example of Dynamic and Static AIS information received from MOF, Korea. ....	25 -
Figure 3-1 Flowchart of the training data procurement algorithm for AIS information. ....	28 -
Figure 3-2 Schematic outline of defining target interpolation time for each vessel. -	33 -
Figure 3-3 Geometry of SAR antenna and the maneuvering target object. ....	42 -
Figure 3-4 Offset between vessels and their paths from dynamic AIS data. ....	47 -
Figure 3-5 Transformation of target motion into range-projected velocity. ....	49 -
Figure 3-6 Examples of false AIS signals from ground noted as green circle. .	56 -
Figure 3-7 Training data retrieval for the case $0 \leq \text{COG} < \pi/2$ . ....	57 -
Figure 3-8 Training data retrieval for the case $\pi/2 \leq \text{COG} < \pi$ . ....	58 -
Figure 3-9 Training data retrieval for the case $\pi \leq \text{COG} < 3\pi/2$ . ....	59 -
Figure 3-10 Training data retrieval for the case $3\pi/2 \leq \text{COG} < 2\pi$ . ....	60 -
Figure 3-11 Illustration on (a) VPASS information plotted to Cosmo-SkyMed SAR image, (b) group of non-fishing boats and (c) fishing boats in identical region in optical image from Google Earth. ....	64 -
Figure 3-12 Flowchart of the training data procurement algorithm for VPASS information. ....	65 -
Figure 4-1 Calculation of convolution in machine learning feature extraction. -	68 -
Figure 4-2 Schematic algorithm of EAST-based object detection architecture. -	73 -
Figure 5-1 Illustration on training data assessment using bounding boxes from binarization and cluster removal. ....	78 -



Figure 5-2 (a) Original and (b) enlarged azimuth ambiguity signals and their distance from the original ship scatterers.....	84 -
Figure 5-3 Distribution of width and height of detected bounding box from AIS-based ship detection. ....	89 -
Figure 5-4 Distribution of estimated length of the detected ships from Sentinel-1 SAR images. ....	90 -
Figure 5-5 Spectral distribution of training data on fishing boats from VPASS information. ....	93 -
Figure 5-6 Spectral distribution of training data on ships from AIS information. ...	94 -
Figure 5-7 Illustration of (a) schematic description of Radon transform, (b) cropped image of fishing boat candidate and (c) Radon transform of the cropped image.....	97 -
Figure 5-8 Description of annotation assessment and database-based evaluation on a (a) fishing boat chip and (b) non-fishing boat chip. ....	101 -
Figure 5-9 Assessment on annotation algorithm on airplane landing lights (a) in Cosmo-SkyMed SAR image with (b) cropped image from Google Earth and (c) photographic road view on the identical region. ....	102 -
Figure 5-10 Distribution of width and height of detected bounding box from VPASS-based fishing boat detection. ....	108 -
Figure 5-11 Distribution of estimated length of the detected fishing boats from Cosmo-SkyMed SAR images. ....	109 -
Figure 6-1 Typical illustration results of contrast between two different training datasets of AIS-based ship detection.....	113 -
Figure 6-2 Flowchart of discrimination of unclassified vessels from vessel detection results and dynamic AIS and VPASS information. ....	119 -
Figure 6-3 Typical examples of determination of unclassified ships from Sentinel-1 SAR images.....	123 -
Figure 6-4 Typical examples of determination of unclassified fishing boats from Cosmo-SkyMed SAR images. ....	124 -

## List of Tables

Table 2-1 Acquisition time of SAR image data .....	15 -
Table 2-2 Specifications of Sentinel-1 IW GRDH mode .....	18 -
Table 2-3 Specifications of Cosmo-SkyMed Stripmap Himage mode .....	19 -
Table 5-1 SAR Images selected for ship detection assessment.....	80 -
Table 5-2 AIS-based ship detection performances on two different training datasets. .....	88 -
Table 5-3 SAR Images selected for fishing boat detection assessment. ....	104 -
Table 5-4 VPASS-based fishing boat detection performances.....	107 -
Table 6-1 Determination of unclassified vessels on SAR images for testing..	122 -

# **Chapter 1.**

## **Introduction**

### **1.1 Research Background**

Maritime safety and preservation of oceanic resources can be ensured via stable monitoring of littoral and pelagic regions [1]. Recent studies on surveillance over such regions predominantly focused on vessels, with implications for both trade monitoring and managing illegal fisheries [2]. Continuous and robust monitoring of vessel movement has been widely conducted using a variety of apparatus, most of which have been failed to overcome the scarcity of information, especially small quantity of data [3, 4]. Hence, remote sensing devices were generally preferred for ship surveillance for their wide coverage, high accessibility and precision [5]. Conventional usages of remote sensing platforms for ship monitoring include hyperspectral, electro-optical, infrared imaging [6]; synthetic aperture radar (SAR) was considered stable and influential for its independence from weather conditions and sunlight [7, 8].

In SAR images, a substantial number of man-made structures often demonstrate high backscattering coefficient, especially double-bounce scattering [9]. In the case of vessels on the ocean, their discernibility generally increased as background ocean exhibited feeble backscattering [10].

Surveillance and monitoring vessels with SAR imaging were achieved by

detection and recognition of vessels, especially for ship traffic [11]. A rudimentary ship detection algorithm under such conditions focused on a vivid footprint of the object imprinted on the SAR image. Presenting a threshold on the calibrated SAR image intended to separate high backscattering pixels in the ocean, often improperly considered as a signal from ship, was examined [12], or an attempt to measure Radar Cross Section (RCS) of ships in a corresponding SAR image was made [5]. Given that backscatter and RCS could be affected by incidence angle, object length and shape, material and cross section, high probability of misdetection on ship-like scatterers remains in case of using such methodologies [13].

Another stream of research on spectral vessel characteristics involved statistical analysis, such as implementing principal component analysis (PCA) to classify destroyers [14] or comparing different parameters one other such as coherence, cross-correlation, entropy and generalized likelihood ratio test to derive the best performance parameter in ship detection [15]. Spectral and statistical analyses on ships not only enabled ship detection, but was also applied in recognition because superstructure of vessel was directly imprinted in each SAR image pixel; scattering features on different types of vessel could be used in segmenting chips of vessels from RADARSAT-2 SAR images [16]. For classifying ships in SAR image coverage, difference in polarimetric and spectral character between each class of ship was deliberated. To mitigate the obstacles in procuring fully-polarized SAR image data, a SAR simulation algorithm was implemented and tested for diverse bearing angle and incidence angle [17]. Furthermore, as a deterministic algorithm,

fuzzy logic, was subsequently proposed for single-polarimetric SAR images for discriminating ship chips inside ENVISAT SAR images [18]. However, discriminating vessels in SAR images with their spectral signatures could potentially lead to misdetection on ship-like structures, such as onshore facilities, small islets and group of sea scatterers, or derive an image-dependent result on detection and classification.

Attempts to exploit additional information elicited the usage of polarimetric SAR (PolSAR), which involved SAR imagery implementing various polarizations [19]. An algorithm was devised to mitigate the tradeoff between swath width and polarimetric information [20] and polarimetric algorithm derivation discriminating symmetric properties between artificial scatterers and the sea surface was tested [21]. Applying full-PolSAR data implementing the UAVSAR L-band dataset, a study managed to detect vessels via a complete polarimetric covariance difference matrix [22].

Conventional methodologies on ship detection had limitations that prevented them from being widely applied for full-size SAR images. Presenting a threshold value to the backscattering value of SAR images encompasses a risk of detecting ship-like structures in the ocean, especially in boisterous oceanic conditions which increase the background backscattering [10]. For identical exploitation of PolSAR on ship detection, quad-polarimetric data were required containing full information on four channels of scattering matrix, which was minimally accessible when relatively compared to single-pol or dual-pol SAR data [18]. Statistical vessel analysis often

inspected pixels corresponding to the target ships without including oceanic background [5]; it limited the hazard of detecting ground scatterers as ships.

In the case of detecting and recognizing vessels in full-sized SAR images both regarding ships and the contrast between ships and their background, machine learning and artificial intelligence imitating a humanisticological algorithm were employed; beginning with constant false alarm rate (CFAR), artificial neural network (ANN) and support vector machine (SVM) [23-26]. Among a number of machine learning algorithms, the convolutional neural network (CNN) was regarded as suitable for ship detection and recognition which offers optimized architecture for character extraction inside each image [27]. Implementing CNN for ship detection and recognition often involved architectural reform, an algorithmic mitigation that mitigates performance and efficiency on time and workload. Such reform was primarily owing to the procurement of a vessel's training data, because a detector based on CNN requires a significant quantity of training data [28]. Typical applications on such enhancement include modifying conventional faster region-base convolutional neural network (Faster R-CNN) to retrieve multiscale information [29], constructing a new grid CNN (G-CNN) model inspired by you only look once (YOLO) detection architecture [30] and rendering a hierarchical CNN (H-CNN) based ship detection algorithm to effectively discern ships from their ghost signals [31]. However, implementing CNN-based detection algorithm in ship detection contains fundamental limitations in gathering training data; signatures of ships are not always decisively discernable in SAR images, especially

in mid-to-low resolution SAR images.

Apart from monitoring vessels in SAR images, real-time and expeditious data for tracking ships has been implemented for such an objective: Automated Identification System (AIS). It operates as a measurement for vessel surveillance which is a ship identification sensor containing real-time information on its position, velocity and acquisition time. Such conditions allow AIS information to be widely implemented as a reliable information source for vessel surveillance, tracking and monitoring. Notwithstanding, AIS information corresponding to each ship was gathered in a discrete fashion, so precise interpolation with respect to targeted time was widely examined. A research that identified the contrast between linear interpolation, circular interpolation and Kalman filter was conducted and determined that the accuracy of circular interpolation and Kalman filter exceeded that of linear interpolation [32]. In addition, the methodology on interpolating AIS information in missing regions was analyzed using linear and cubic Hermit interpolation [33].

In addition to being solely implemented, AIS information was often accompanied by remote sensing data. Comparison between AIS information characteristics for each vessel and its SAR image signatures were conducted; combining TerraSAR-X SAR images with terrestrial and satellite AIS information was pursued [34]. Subsequent studies on such research field, data fusion between AIS information and vessels in SAR images, were often targeted to mitigated the difference between the two domains, presenting an unsupervised domain adaptation method proposed for

vessel classification by accurately matching ship length and beam [35] and adopting a knowledge transfer mechanism implementing parameters derived from ship length and beam [36]. A study further analyzed the velocity evaluation from SAR image data and AIS information via Doppler frequency shift of moving object [37].

An operation to render an uninterrupted connection between AIS information and vessels' signature in SAR images was recently conducted where an algorithm was proposed to assemble a dataset containing the chips of SAR images containing the signature of each vessel [38]. Designated as OpenSARShip, the database was established using a projected AIS signal on each SAR image, GF-3 and Sentinel-1, and retrieving a SAR image sector with respect to the projection. After interpolation and calibrating azimuth shift caused by the maneuvering vessel's velocity, the algorithm searches for the target vessel within a 300m radius from the projected AIS position. Inside the radius, the vessel demonstrating the smallest offset in length and beam is selected as the target vessel, of which the signature is yielded and saved in a separate database. In spite of the OpenSARShip database involving diverse application fields, the algorithm constructing it has limitations in restoration. In the procedure of comparing the length and beam of each vessel in the SAR image and AIS information, unlike the latter, which was directly obtained from AIS information, the former was manually procured via visual interpretation. Such cases, especially in low resolution SAR images, could cause confusion between vessel-like scatterers and vessels, resulting in a mismatch between the target vessels in the SAR image and corresponding AIS information. Moreover, when similar types of vessels



are present in close vicinity of each other, disorientation could be induced in determining the target vessel. Avoidance of such conditions requires compact, robust and tight training datasets extracted from manual inspection and involving unnecessary background or other scatterers.

## 1.2 Research Objective

Real-time surveillance and handling vessels that are not registered or permitted, monitoring and discriminating AIS-deprived vessels are imperative. Achieving such study objectives could involve estimating the number of vessels that access the major ports or trespass in the exclusive economic zone (EEZ). In addition, it could be effective if AIS information is accompanied by the detection results to discriminate illegal vessels from the others. It could be beneficial to ascertain the nation-wide trade and administration of national water bodies in a quantified manner, especially in Korea where major ports are located close to each other and illegal fishing boats prevail in the EEZ.

In order to effectively perform these objectives and fundamentally ameliorate the limitations of conventional vessel detection studies, this study deduced that rendering training data which securely and robustly contain the spectral characteristics of diversified vessels was crucial. Hence, an automated training data retrieval algorithm was devised and implemented on SAR images to improve the performance of a CNN-based vessel detection model. The proposed algorithm directly associates SAR images and AIS information corresponding to SAR images, considering discrete position, velocity and interior allocation of AIS sensor to train the intrinsic characteristics of a vessel. Furthermore, to demonstrate the effectiveness of applying such an algorithm to monitoring oceanic regions and to indicate this algorithm could be executed under any type of SAR image, training

data was acquired targeting a number of fishing boats in SAR images with high spatial resolution.

The remainder of the dissertation introduces the automated training data retrieval algorithm of vessels and detection of vessels in full-sized SAR images using the proposed algorithm. Explanation of the input data, SAR image data, SAR ancillary data, AIS and VPASS information, is described in Chapter 2. The detailed and explicit procedure of the training data retrieval algorithm from input data is presented in Chapter 3, which successively implements (i) accurate interpolation of discrete AIS information, both position and velocity, with respect to the target interpolation time of each vessel, (ii) mitigating the Doppler frequency shift, or azimuth shift, induced by the movement of each ship and (iii) direct retrieval of training data from AIS position and its allocation inside each ship. The chapter also contains a training data retrieval algorithm for fishing boats from VPASS information, while suggesting a supplementary algorithm for AIS information combining two algorithms proposed in advance. Chapter 4 introduces the architecture of the CNN-based training algorithm implemented for ship detection. The detection results and discussions for both AIS-based ships and VPASS-based fishing boats, examples of training data verification using binarization of backscattering coefficient are presented in Chapters 5 and 6, accompanied by the applications in discerning unclassified vessels. The concluding remarks are provided in Chapter 7.

## **Chapter 2.**

### **Data Acquisition**

Input data for this research consists of SAR image and AIS data, both of which essentially operate in establishing vessel training datasets. Information on these two data sources is described in the following sub-sections.

#### **2.1 Acquisition of SAR Image Data**

As the primary intent of the study is to successfully detect ships inside SAR image, it was essential to select SAR image data containing as many ships as possible. Given the tradeoff between spatial resolution and the scope of the SAR image, the author determined that wide coverage that can render mass training data could be decisive in the model's performance. For mid-resolution SAR image ensuring a wide swath and coverage, the Sentinel-1 interferometric wide (IW) mode image data was implemented, which is the general method of acquisition in the mid-latitude region .

Sentinel-1A and Sentinel-1B SAR satellites provide six days of temporal resolution under constellation, which is considered relatively high, without any monetary charge. Such conditions make Sentinel-1 SAR data highly available, accessible and user-friendly. Owing to the compromise between resolution and SAR

data coverage, spatial resolution of Sentinel-1 SAR is inferior to that of other commercial SAR satellites. In order to exploit the advantage of such a condition, the high possibility of including abundant ships, the research selected the spatial scope of the SAR data in the vicinity of major Korean harbors. The coverage of the Sentinel-1 SAR images included the southeast coast of Korea with Busan, the largest port in South Korea, Ulsan, Pohang and Geoje.

For detecting fishing boats whose magnitude was around 15~20m were mostly invisible in the Sentinel-1 IW mode SAR images which had 20m of spatial resolution. As a supplement, Cosmo-SkyMed SAR images covering the major harbors of southwestern Korea, Yeosu and Gwangyang, were implemented. With higher resolution than Sentinel-1 SAR, with four days of temporal resolution under constellation and the highest spatial resolution of 1 m when implemented without martial purposes, these SAR images were expected to effectively identify the target fishing boats compared to Sentinel-1 SAR images. For this research, Stripmap Himage mode of Cosmo-SkyMed SAR images with 3m of spatial resolution were implemented.

The detailed coverage and information of Sentinel-1 SAR image data in both ascending path (Sentinel-1A) and descending path (Sentinel-1B) with Cosmo-SkyMed image data are described in Figure 2-1 and Table 2-1, where the fundamental information of Sentinel-1 IW GRDH mode and Cosmo-SkyMed Stripmap mode is respectively presented in Tables 2-2 and 2-3.

As the study intended to directly associate SAR image data and AIS information, the SAR image ought to have an adequate configuration where AIS information for each ship could be easily projected. In addition, each SAR image pixel should represent the precise backscattering coefficient of the corresponding physical environment. This implies that the SAR image after radiometric and geometric calibration is suitable as training and test image data and the SAR image data should be eligible for such calibration.

In addition to the SAR image data, ancillary data of each SAR image data was necessary for projecting AIS information on the corresponding SAR image. The explicit duration of satellite image acquisition time and heading angle was imperative for resolving the accurate acquisition time for each pixel inside SAR spatial coverage. In addition, geocentric state vector of the SAR satellite was essential in calculating the slant range and incidence angle of each pixel. The SAR satellite state vector contains position and velocity in geocentric coordinates, which describes the movement of satellite in a discrete, but periodic fashion. Ancillary data corresponding with the SAR image was obtained from the annotation file of the respective Sentinel-1 GRDH IW mode images, but separately rendered via GAMMA remote sensing software as corresponding parameter files for Cosmo-SkyMed Stripmap mode images.

Both SAR image and ancillary data were implemented; the SAR images were applied to match the real-time data of vessels and derive the bounding box of training data in a precise format, where the SAR ancillary data, especially the state

vector of SAR in geocentric coordinates, was implemented for restoration of the elliptic SAR satellite path. It successively mitigates the offset imprinted in SAR image to match the real-time vessel data into the precise location of the corresponding SAR image.

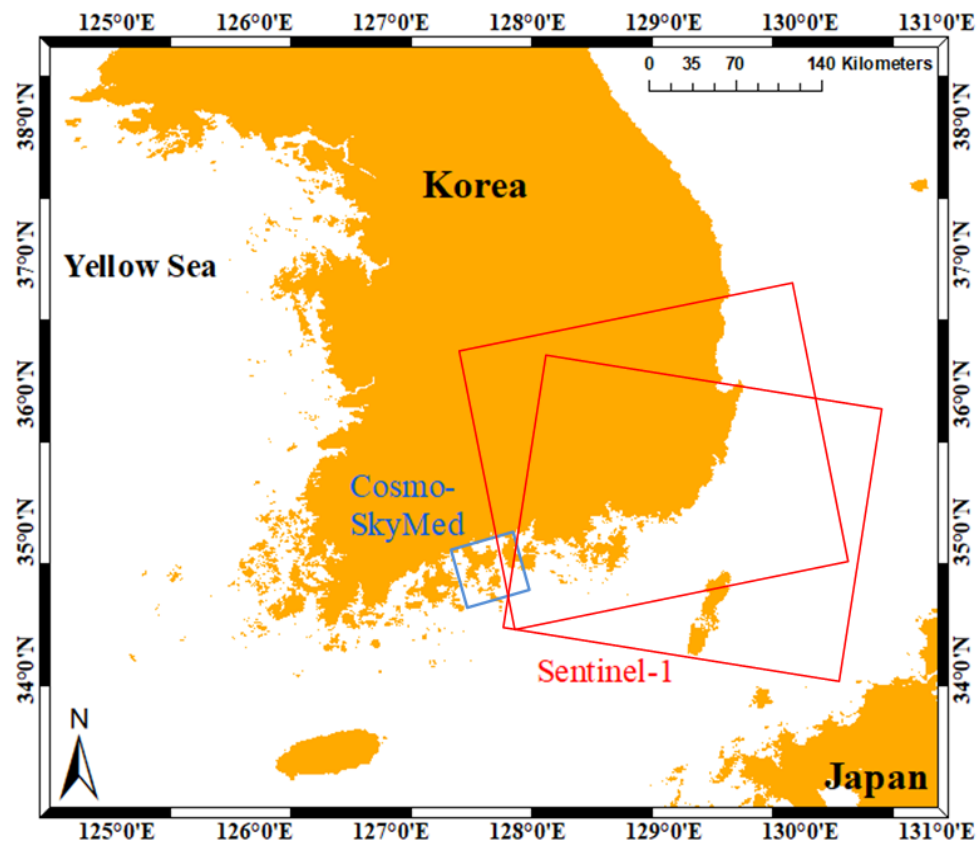


Figure 2-1 Spatial coverage of Sentinel-1 and Cosmo-SkyMed SAR data.



**Table 2-1 Acquisition time of SAR image data**

<b>Satellite &amp; Mode</b>	<b>Acquisition Time (UTC)</b>	<b>Region</b>
Sentinel-1A, IW	26/06/2018 09:23:00~09:23:29	Southeast Korea
Sentinel-1A, IW	08/07/2018 09:23:00~09:23:29	Southeast Korea
Sentinel-1A, IW	20/07/2018 09:23:01~09:23:30	Southeast Korea
Sentinel-1A, IW	01/08/2018 09:23:02~09:23:31	Southeast Korea
Sentinel-1A, IW	18/09/2018 09:23:04~09:23:33	Southeast Korea
Sentinel-1A, IW	30/09/2018 09:23:04~09:23:33	Southeast Korea
Sentinel-1A, IW	12/10/2018 09:23:05~09:23:34	Southeast Korea
Sentinel-1A, IW	24/10/2018 09:23:05~09:23:34	Southeast Korea
Sentinel-1A, IW	17/11/2018 09:23:04~09:23:33	Southeast Korea
Sentinel-1A, IW	29/11/2018 09:23:04~09:23:33	Southeast Korea
Sentinel-1A, IW	11/12/2018 09:23:03~09:23:32	Southeast Korea
Sentinel-1A, IW	23/12/2018 09:23:03~09:23:32	Southeast Korea
Sentinel-1A, IW	16/01/2019 09:23:02~09:23:31	Southeast Korea
Sentinel-1B, IW	12/09/2018 21:23:52~21:24:26	Southeast Korea
Sentinel-1B, IW	24/09/2018 21:23:53~21:24:26	Southeast Korea

Sentinel-1B, IW	18/10/2018 21:23:53~21:24:27	Southeast Korea
Sentinel-1B, IW	30/10/2018 21:23:53~21:24:27	Southeast Korea
Sentinel-1B, IW	11/11/2018 21:23:53~21:24:26	Southeast Korea
Sentinel-1B, IW	23/11/2018 21:23:53~21:24:26	Southeast Korea
Sentinel-1B, IW	05/12/2018 21:23:52~21:24:26	Southeast Korea
Sentinel-1B, IW	17/12/2018 21:23:52~21:24:25	Southeast Korea
CosmoSkyMed1, Stripmap, Himage	08/07/2018 21:08:08~21:08:15	Yeosu, Gwangyang
CosmoSkyMed2, Stripmap, Himage	10/03/2018 21:07:50~21:07:57	Yeosu, Gwangyang
CosmoSkyMed2, Stripmap, Himage	13/05/2018 21:07:59~21:08:06	Yeosu, Gwangyang
CosmoSkyMed2, Stripmap, Himage	13/03/2019 21:08:11~21:08:19	Yeosu, Gwangyang
CosmoSkyMed2, Stripmap, Himage	16/05/2019 21:08:20~21:08:27	Yeosu, Gwangyang
CosmoSkyMed4, Stripmap, Himage	09/01/2018 21:07:42~21:07:49	Yeosu, Gwangyang
CosmoSkyMed4, Stripmap, Himage	06/09/2018 21:08:08~21:08:15	Yeosu, Gwangyang
CosmoSkyMed4, Stripmap, Himage	09/11/2018 21:08:15~21:08:23	Yeosu, Gwangyang

CosmoSkyMed4,  
Stripmap, Himage

12/01/2019 21:08:12~21:08:20

Yeosu, Gwangyang

---

**Table 2-2 Specifications of Sentinel-1 IW GRDH mode**

<b>Parameter name</b>	<b>Parameter for Sentinel-1</b>	<b>Remark</b>
Sensor complement	C-Band SAR	
Central frequency	5.4GHz	
Polarization	VH, VV	Dual polarization
Look	Right	
Antenna size	$12.3 \times 0.821$ (m)	
Spatial Resolution	$20.4 \times 22.6$ (m)	
Pixel Spacing	$10 \times 10$ (m)	
Number of Looks	$5 \times 1$	Range $\times$ Azimuth
Bits per pixel	16	
Ground range coverage	251.8 (km)	

**Table 2-3 Specifications of Cosmo-SkyMed Stripmap Himage mode**

<b>Parameter name</b>	<b>Parameter for Cosmo-SkyMed</b>	<b>Remark</b>
Sensor complement	X-Band SAR	
Central frequency	9.6GHz	
Polarization	HH	Single polarization
Look	Right	
Spatial Resolution	3×3 (m)	
Swath Width	40 (km)	

## **2.2 Acquisition of AIS and VPASS Information**

AIS information for each Sentinel-1 SAR image was accordingly obtained to procure ship training data. The AIS dataset could be utilized as a means for vessel tracking apparatus, which has been widely accomplished in marine surveillance since vessels are required to address their AIS signals to either a ground station or the satellite [33]. Ships without AIS information therefore, were considered as unclassified.

AIS information was provided by the Ministry of Oceans and Fisheries, Korea (MOF) for the sake of the research. It could be classified into two different categories: dynamic and static AIS information. Dynamic AIS information contains real-time messages from the ship which is transmitted to the station. It is the discrete, but unevenly received data of which the interval between the adjacent messages is not constant. For each time of acquisition, dynamic AIS information offers the data which identifies the longitude and latitude in degrees and the ship movement with the corresponding ship identification number. Explanation of the maneuvering fashion of vessel is depicted in two parameters: course-over-ground (COG) and speed-over-ground (SOG). The COG denotes the ship's heading angle with respect to the direction towards the North Pole, while SOG denotes the ship velocity towards COG, usually expressed in knots. Conversely, static AIS information includes the constant specification of each ship, including the ship

identification number, ship type and dimensions indicating the internal allocation of AIS sensor. Figure 2-2 briefly describes the COG, SOG and dimension of each ship. Four dimensions, DimA, DimB, DimC and DimD respectively represent the distance from the AIS sensor to the vessel's bow, stem, port and starboard in meters. Black letters in Figure 2-2 explain information from dynamic AIS information (COG, SOG and position of AIS sensor), where white letters denote information from static AIS information (Dimensions).

Figure 2-3 indicates an abridged example of AIS information, both static and dynamic, received from the MOF. Dynamic AIS data includes MMSI number, which dictates Ship ID, exact acquisition time for each piece of AIS information, longitude and latitude of AIS sensor, SOG, COG and heading information. Static AIS data for each ship includes MMSI number, name and type of each ship, IMO number, call sign, dimension information expressed as DimA-D, draft and beam. Among these static AIS data constituents, MMSI number for matching static data to corresponding dynamic data, type of ship and dimensional information was implemented for the proposed algorithm.

The temporal span of the AIS information was 10 minutes which securely includes the SAR image acquisition time. The spatial coverage was assigned identically to the spatial coverage of the respective Sentinel-1 SAR image as presented in Table 2-1.

However, AIS information does not cover the entire amount of available vessel

information; small fishing boats are operating a different system named VPASS. The operation of VPASS system resembles that of AIS, containing location, SOG and COG of each fishing boat in an irregular and discrete manner in the case of dynamic information. The difference between AIS and VPASS information lies in static information, where static information only contains length and beam of each fishing boat, respectively corresponding to DimA+DimB and DimC+DimD in static AIS information. VPASS information was also truncated into 10 minute intervals including the SAR image acquisition time with conforming coverage of each image.

For Korean guidelines, an AIS sensor is required to be installed on fishing boats exceeding 10 tons, ships maneuvering in coastal regions over 50 tons and passenger ships exceeding 150 tons, while the VPASS sensor is attached to licensed fishing boats or those inside inland water bodies; fishing boats docked at the port are spared from VPASS information report [39, 40]. This implies that VPASS information is acquired from restricted number and type of ship (fishing boat) whereas AIS information is obtained from various vessel types and magnitudes.

In short, information related to position, velocity and dimensions of a vessel was sorted and implemented from dynamic and static information of real-time data. Within dynamic information, discrete latitude and longitude indicating the sensor's position along with COG and SOG elaborating the vessel's velocity were selected for interpolation within the corresponding SAR image. From static information, information which indicates the internal allocation of the real-time sensor of vessel, identified as dimensions, was updated for defining the training data bounding box in



an accurate and compact manner reflecting the genuine extent of the vessel.

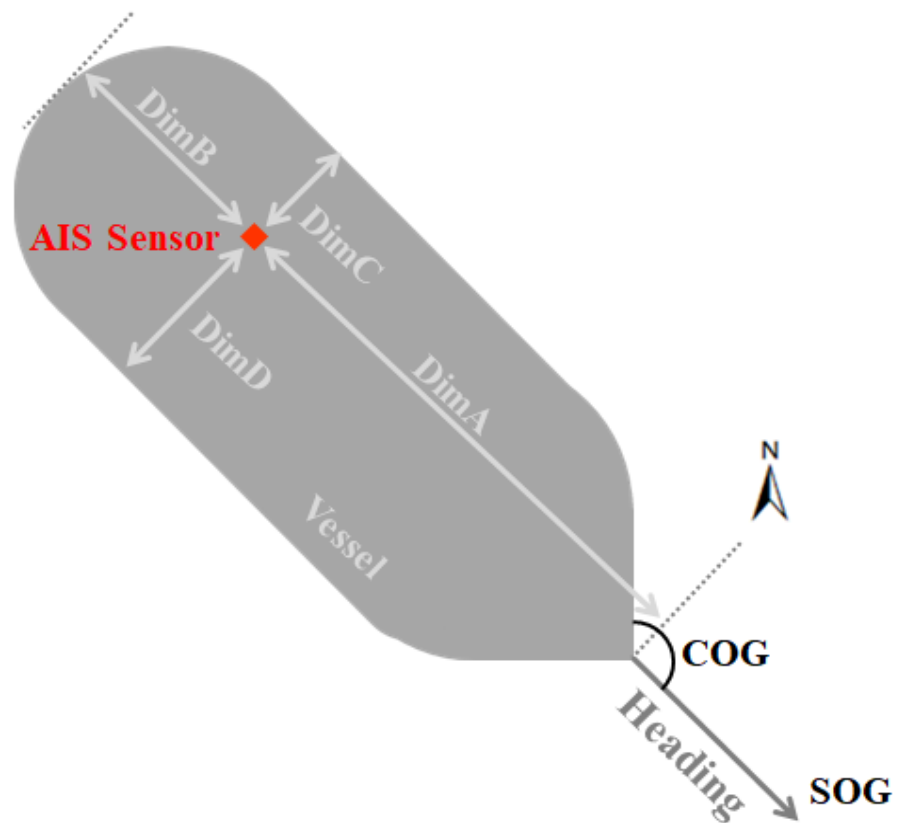


Figure 2-2 Illustration on individual maneuvering fashion of AIS sensor-installed vessel.

## Dynamic AIS

Date : 2018-09-06 00:00:00 ~ 2018-09-06 23:59:59

# of ships : 1886

MMSI,Time,Lat,Lon,SOG,COG,Heading

```
211367460,2018-09-06 18:20:04,35.61985,129.970073333333,11.8,206.5,207
211367460,2018-09-06 18:20:14,35.6194516666667,129.969823333333,11.8,206.5,207
211367460,2018-09-06 18:20:24,35.6188183333333,129.96944,11.8,206.5,207
211367460,2018-09-06 18:20:33,35.6183683333333,129.969173333333,11.8,206.5,207
211367460,2018-09-06 18:20:43,35.6178683333333,129.96889,11.8,206.5,207
211367460,2018-09-06 18:21:04,35.616835,129.968273333333,11.8,206,207
211367460,2018-09-06 18:21:14,35.616385,129.968006666667,11.8,206.5,207
211367460,2018-09-06 18:21:24,35.6159516666667,129.967741666667,11.8,206.5,207
211367460,2018-09-06 18:21:33,35.6155516666667,129.967506666667,11.8,206,207
211367460,2018-09-06 18:21:43,35.6150516666667,129.967206666667,11.8,206,207
211367460,2018-09-06 18:22:04,35.6139183333333,129.966525,11.8,206,207
211367460,2018-09-06 18:22:14,35.613385,129.966208333333,11.8,206,207
211367460,2018-09-06 18:22:24,35.612885,129.965906666667,11.8,206,207
211367460,2018-09-06 18:22:33,35.6125516666667,129.96569,11.8,206,207
211367460,2018-09-06 18:22:43,35.6120183333333,129.965356666667,11.8,206.5,207
211367460,2018-09-06 18:23:04,35.610985,129.964741666667,11.8,206.5,207
```

## Static AIS

MMSI,Shipname,Shipcode,IMO,Callsignal,DimA,DimB,DimC,DimD,draft,weight

```
0,,WIG,,@DSQ,0,0,0,0,0
1,00001,WIG,0,KUMHO,1,1,1,1,0,0
100000000,0,Fishing,0,,30,20,4,4,0,396
100000811,AISB,Fishing,,111111,12,12,4,4,0,41
100877090,52958,Fishing,,69365,0,0,0,0,0,0
100896576,,Fishing,0,,0,0,0,0,0,0
100900001,,Tanker(s),,16888,40,10,5,1,0,396
100900002,AIS_SHIPU,Cargo ships,0,,40,10,5,1,0,396
100900004,B,Fishing,,,40,10,5,5,0,396
100900011,JGT AIS TEST SHIP,Cargo ships,,YYYY,40,10,5,1,0,396
100900013,,Cargo ships,,YYYY,40,10,5,1,0,396
100900014,AD AIS TEST SHIP,Other types of ship,,,0,0,0,0,0,0
100900015,JGA AIS TEST SHIP,Cargo ships,,YYYY,40,10,5,1,0,396
100900016,K AIS TEST SHIP,Cargo ships,,YYYY,40,10,5,1,0,396
100900018,,Cargo ships,,YYYY,40,10,5,1,0,396
100900020,JGT AIS TEST SHIP,Other types of ship,,,0,0,0,0,0,0
100900021,,Cargo ships,,YYYY,40,10,5,1,0,396
100900023,AD AIS TEST SHIP,Other types of ship,,,0,0,0,0,0,0
100900030,,Cargo ships,,YYYY,40,10,5,1,0,396
100900031,AJ AIS TEST SHIP,Cargo ships,,YYYY,40,10,5,1,0,396
100900116,AIS TEST SHIP,Cargo ships,,YYYY,40,10,5,1,0,396
```

**Figure 2-3 Abridged example of Dynamic and Static AIS information received from MOF, Korea.**

## **Chapter 3.**

### **Methodology on Training Data Procurement**

In relation to rendering training data for machine learning object detection architecture, it is anticipated that it would be effective to create a training data bounding box which indicates the intrinsic character of vessel in appropriate size. The ship bounding box, therefore, should be constructed tightly with respect to each ship's exact size. Such an objective requires precise processing and execution of AIS information as much as possible. Conventional research handled similar procedure, projecting AIS data to position with respect to the target time and Doppler frequency shift calibration [38], but without explicit explanation which ensures high accuracy of performance. This study however, aims to keep the inaccurate and deficient training data from degrading the overall detection performance.

Since the major objective of this study was obtaining mass training data of ship to fundamentally ameliorate ship detection performance, this section concentrated on obtaining vessel training data. Automated procurement of vessel training data consisted of three stages: Interpolation of discrete AIS information with respect to acquisition time, mitigation of Doppler frequency shift caused by each ship's maneuvering fashion and direct derivation of training data in the form of a bounding box from calibrated AIS information. Sentinel-1 SAR images, as explained in the previous chapter, were implemented in the first stage of interpolation, accompanied

by dynamic AIS information and the portion of the SAR ancillary data related to the acquisition time of each image. The other portion of the SAR ancillary data including satellite state vector and interpolated AIS data were entered as input data for the second stage. Static information was used for the final stage, along with the COG from the first stage and precise AIS position from the second stage. The final output of this chapter contains a text file corresponding to the SAR image, following the conventional style of training data of object detection.

The schematic overview of flowchart is shown in Figure 3-1, describing the input data and the procedure of Chapter 3.

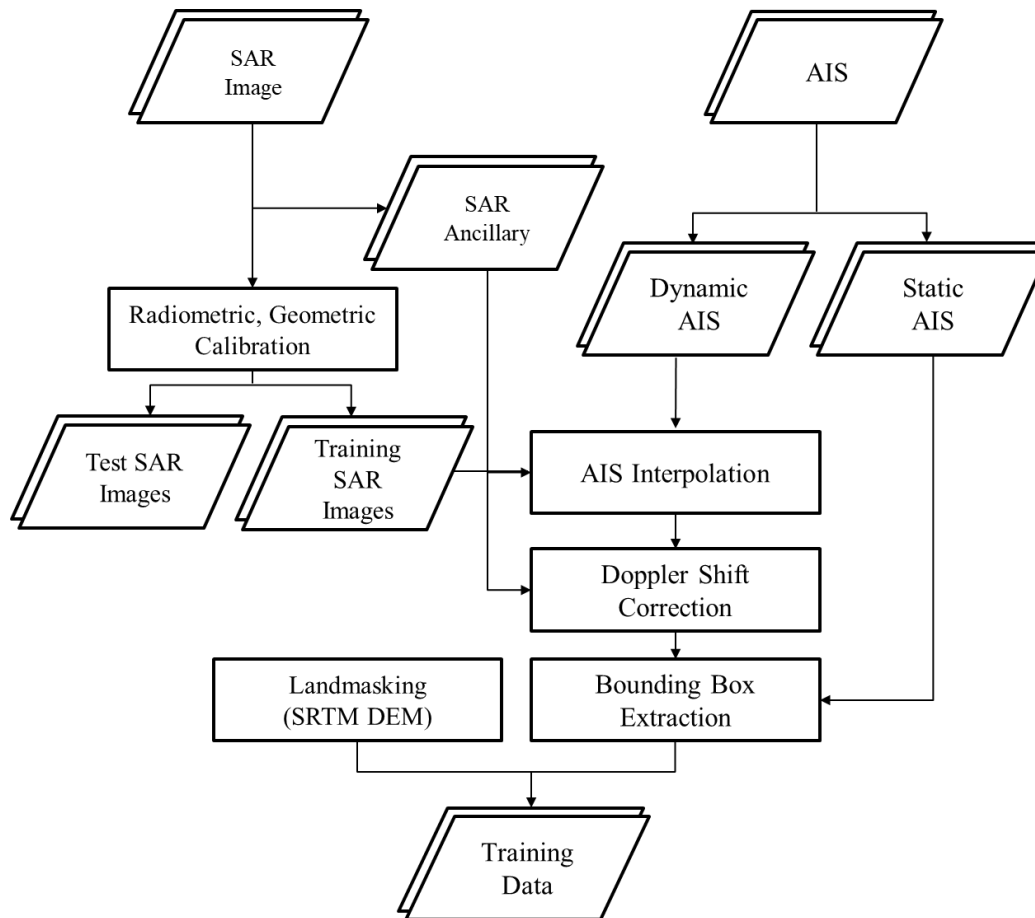


**Figure 3-1 Flowchart of the training data procurement algorithm for AIS information.**

## **3.1 Interpolation of Discrete AIS Data**

### **3.1.1 Estimation of Target Interpolation Time for Vessels**

This study implemented AIS information received from the ground station, offered in a discrete manner and rarely matched with the desired time. Accurate interpolation to remedy such issues was therefore required, which could ascertain the identical allocation of each ship. Apart from conventional photogrammetric images, SAR images are procured while the SAR antenna and satellite or aircraft carrying it are moving [7]. Owing to the acquisition conditions, each pixel inside the SAR image has different acquisition times.

The acquisition time of a pixel in the SAR image strongly depends on the pulse repetition frequency (PRF). The PRF is a parameter of the SAR antenna which identifies the number of pulse emissions per second [7, 8]. Pulses from the SAR antenna therefore, are emitted every  $1/\text{PRF}$  second, often declared as pulse repetition interval (PRI) [7]. Within a single pulse transmission taking place inside a PRI, both pulse transmission from the SAR antenna and subsequent echo retrieval from ground or ocean occur. Given that the difference in fast time in range direction is negligible to the difference in slow time in azimuth direction, it could be approximated that pixels in the azimuth line share an identical acquisition time [41].

The acquisition time of each azimuth line could be quantitatively speculated, provided that the SAR satellite system is a zero-Doppler geometry, which is the

case for the Sentinel-1 IW mode,

$$T_{az} = T_{start} + PRI \cdot N_{az} \cdot L \quad (1)$$

where  $T_{az}$ , the acquisition time of target azimuth line could be described by the SAR image acquisition start time,  $T_{start}$ , start time of SAR image acquisition time,  $N_{az}$ , the order of target azimuth line from the fastest acquired azimuth line, and  $L$ , number of looks.

Sentinel-1 SAR images acquired in IW, GRDH mode were preprocessed as radiometric and geometric calibration. Radiometric calibration in SAR image converts the digital number (DN) of each pixel into radar cross section (RCS), removing the path scattering and featuring the backscattering from the desired target [42]. Geometric calibration removes the geometric distortion of target scatterers owing to side-looking and turbulence of SAR platform itself, of which the conclusive objective lies on geocoding [43]. Such calibrations were applied to all SAR image input data, combining the incidence angle map with conventional dual-PolSAR images. With respect to (1), acquisition time of each SAR image pixel was speculated and conserved as separate data for subsequent use. The target time for interpolating AIS information should be deliberated for every vessel. Presentation of an iterative algorithm to define target interpolation time for each vessel was essential since acquisition time from (1) may not precisely describe the veritable AIS sensor location as the vessels passing through the SAR image pixels possess different acquisition times.



For each SAR image containing a number of ships, all of the AIS data were interpolated with respect to the average time of acquisition time span: mean of the initiation and termination of acquisition time. As the acquisition time map for every pixel in the corresponding SAR image was already acquired, the acquisition time of the grossly interpolated position was diversely driven. Subsequently, the referred acquisition time was shifted to temporary target interpolation time; two pieces of AIS information showing the least time interval with the target time were selected, each prior and after it, and the interpolation was conducted using these two AIS positions. After the second interpolation, the above procedure was operated in an iterative manner, repeating the interpolation using the nearest two AIS positions and applying the acquisition time for the desired position. Such iteration was terminated only when the interpolation and successive migration of AIS information were conducted inside a single spatial resolution. The referred acquisition time for decisive position was selected as conclusive target interpolation time, which was implemented for the next interpolation procedure. Figure 3-2 expresses a schematic outline of the iterative procedure of defining target interpolation time for each vessel.

In addition to determining of explicit target interpolation for each vessel, such procedure also conducts an interpolation on AIS information itself. Because the position and velocity interpolation was conducted, additional interpolation procedures may not be mandatory. In contrast, sensors including AIS often contain a measurement error term, which relies on the system of sensor and constantly

keeps the measurement from elaborating the precise state and location of the target. Hence, this study implemented another algorithm to eliminate the measurement error term and effectively uncover the veritable and genuine position and velocity of each vessel.

Vessels often maneuver at high-velocity in offshore conditions where implementing the proposed algorithm of target interpolation time estimation could be effective. Provided that the high-speed vessel at the azimuthal tip of the SAR image navigated in 20 knots (10.3 m/s), it may reduce approximately 150 m of interpolation offset which could have occurred when the average time of acquisition time span was used. Such quantity of interpolation offset would be reckoned as 7 to 8 pixels in the current Sentinel-1 IW GRDH mode SAR image where the case contaminates the training data of ship by improper bounding box position derivation.

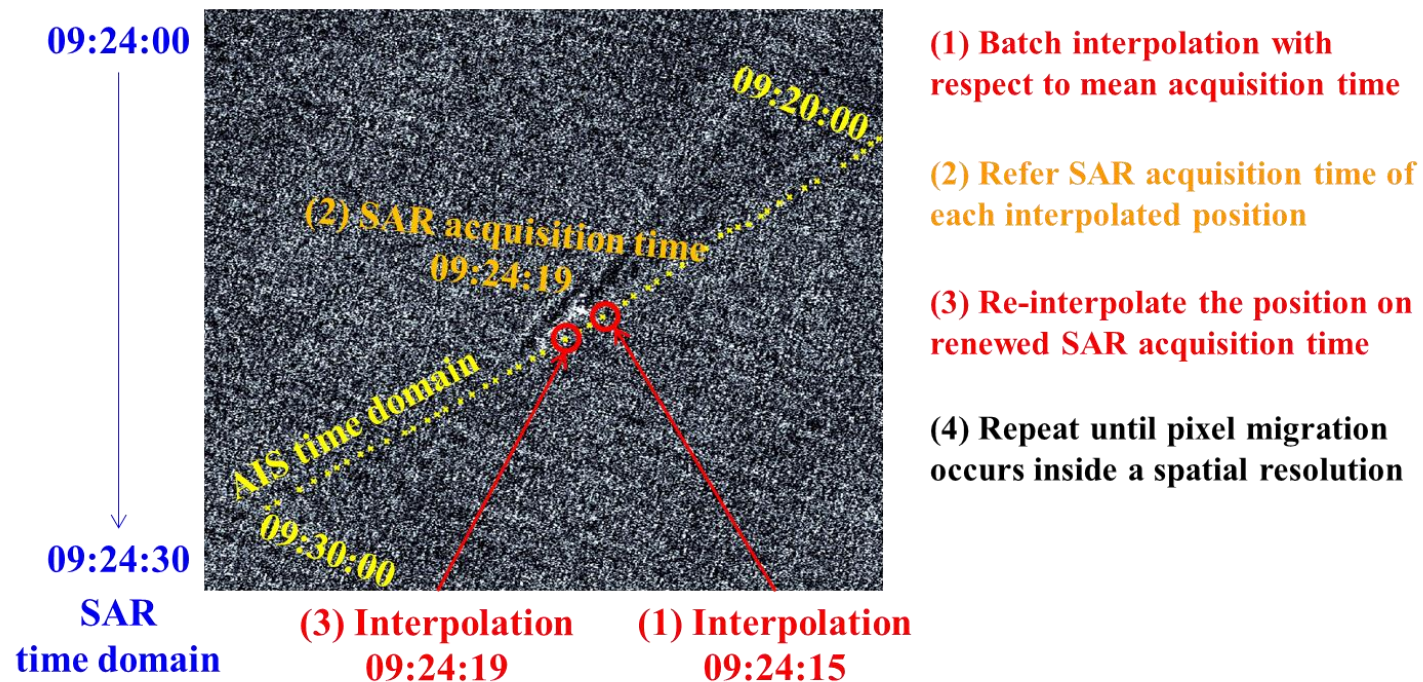


Figure 3-2 Schematic outline of defining target interpolation time for each vessel.

### **3.1.2 Application of Kalman Filter to AIS Data**

Previous studies attempted the AIS data interpolation on the desired position by applying different interpolation methodologies: linear interpolation, circular interpolation and cubic interpolation [32, 33]. Linear interpolation applies the twonearest points to speculate the desired position, where cubic interpolation implements quadratic or higher dimension functions for each path section in order to conduct the interpolation in a curvature. Circular interpolation assumes the maneuvering path of an object is an ideal circle, restoring the target path circle from three previous measurements.

This study determined that instead of applying conventional interpolation methodologies, a renewed approach that could perform both interpolation and measurement error elimination was suitable because every sensor, including the AIS sensor, was susceptible to measurement error terms [44]. For such an objective, a Kalman filter was implemented in order to anticipate the precise position and velocity of each vessel while eradicating the influence on AIS sensor from possible observational error terms. The Kalman filter was adopted as a state estimator first designed for a linear system containing Gaussian noise, but renowned to be performed as the best linear estimator even though the system contains non-Gaussian noise [45]. Because with such characteristics, a Kalman filter was widely implemented in traffic monitoring; given that the Kalman filter underwent several

modifications after it had been presented, a performance contrast on various Kalman filter algorithms was implemented [46], where another research was conducted regarding the macroscopic traffic model based on the Extended Kalman filter and its localized variation [47]. Another application of Kalman Filter was conducted in SAR signal processing; it significantly enhanced the performance of phase gradient autofocus for stripmap SAR data [48].

This study speculated that not only the implementation of Kalman filter on AIS information could be effective, but also applying an elementary Kalman filter without enhancement would suffice given the relatively low spatial resolution of the Sentinel-1 SAR images. A Kalman filter has been applied to calibrating AIS data, which was shown to outperform linear interpolation in terms of interpolation [32]. Moreover, as the style of input AIS data for the Kalman filter was already described [49], this study followed the data format previously presented.

The Kalman filter is an iterative procedure which requires the initial stage, output and estimation from AIS to be arranged as a tractable form called state vector. It is a  $4 \times 1$  vector which consists of the position of the ship in SAR image coordinates as  $(x; y)$  and velocity with respect to each direction calculated by COG and SOG of dynamic AIS data as  $(v_x; v_y)$ . The Kalman filter is a double-staged procedure each of which is named as prediction and estimation. Prediction stage of the Kalman filter provisionally determines the anticipated state vector of the successive iteration, from the time interval between the two adjacent stages as in (2). The style of each composition of the Kalman filter for AIS application followed the previous research

on AIS information [49],

$$\hat{x}_k^- = A \cdot \hat{x}_{k-1} + B \cdot u_k + w_{k-1} \quad (2)$$

From the initial state vector, or the previous stage state vector  $\hat{x}_{k-1}$ , the system implements a time interval between the current and the next adjacent AIS information, expressed as a transition matrix  $A$ . The acceleration of the system is denoted as  $B \cdot u_k$ , which acts as an additional term modifying the position and velocity. The process noise term in (2) is marked as  $w_{k-1}$ . Conventional explanations on components in (2) are described as in (3)-(6) [49], where (6) denotes the initial calculation form of  $\hat{x}_{k-1}$ .

$$A = \begin{bmatrix} 1 & 0 & \Delta t & 0 \\ 0 & 1 & 0 & \Delta t \\ 0 & 0 & 1 & 0 \\ 0 & 0 & 0 & 1 \end{bmatrix} \quad (3)$$

$$B \cdot u_k = \begin{bmatrix} \frac{a_x \cdot \Delta t^2}{2} \\ \frac{a_y \cdot \Delta t^2}{2} \\ a_x \cdot \Delta t \\ a_y \cdot \Delta t \end{bmatrix} \quad (4)$$

$$w_{k-1} = \begin{bmatrix} 0 \\ 0 \\ 0 \\ 0 \end{bmatrix} \quad (5)$$

$$\hat{x}_{k-1} = \begin{bmatrix} lon_{k-1} \\ lat_{k-1} \\ SOG \cdot \cos(COG) \\ SOG \cdot \sin(COG) \end{bmatrix} \quad (6)$$

The time interval between two adjacent AIS data was marked as  $\Delta t$ , acceleration with respect to longitude and latitude marked as  $a_x, a_y$  and  $(lon_{k-1}, lat_{k-1})$  states the position information from the dynamic AIS data in phase  $k - 1$ .

In addition to (2), the Kalman filter holds an additional procedure which revises the system implementing the state vector of the given time lapse; the iterative reflection on the maneuvering fashion of each vessel is conducted to the Kalman filter. A covariance matrix is adopted for such an objective, which is  $4 \times 4$  array composed of covariance between position and velocity in dynamic AIS data. The initial context of covariance matrix is described in (7) and its iterative amendment is described in (8).

$$P_{init} = \begin{bmatrix} \sigma_x^2 & cov(x, y) & cov(x, v_x) & cov(x, v_y) \\ cov(x, y) & \sigma_y^2 & cov(y, v_x) & cov(y, v_y) \\ cov(x, v_x) & cov(y, v_x) & \sigma_{v_x}^2 & cov(v_x, v_y) \\ cov(x, v_y) & cov(y, v_y) & cov(v_x, v_y) & \sigma_{v_y}^2 \end{bmatrix} \quad (7)$$

$$P_k^- = A \cdot P_{k-1} \cdot A^T + Q \quad (8)$$

Following the initial context previously proposed [49], the process noise covariance matrix  $Q$  was regarded as  $P_{k-1}$ . Transition matrix  $A$  is also used in order to reform covariance matrix  $P_{k-1}$ . In (2) and (8), the notation on  $\hat{x}_k^-$  and  $P_k^-$  implies the a priori state, which is the state before calibrated by covariance matrix  $P$ . The prediction of the Kalman filter is terminated after deriving the a priori state of the state vector and covariance matrix.

The successive procedure of estimation consists of modifying the a priori state using Kalman gain, which determines the influence of the following measurement on the conclusive state. The calculation of Kalman gain is performed from (9), where measurement transformation matrix  $H$  and measurement covariance matrix  $R$  are defined as (10) and (11),

$$K_k = P_k^- \cdot H^T \cdot (H \cdot P_k^- \cdot H^T + R)^{-1} \quad (9)$$

$$H = \begin{bmatrix} 1 & 0 & 0 & 0 \\ 0 & 1 & 0 & 0 \\ 0 & 0 & 1 & 0 \\ 0 & 0 & 0 & 1 \end{bmatrix} \quad (10)$$

$$R = \begin{bmatrix} \sigma_x^2 & 0 & 0 & 0 \\ 0 & \sigma_y^2 & 0 & 0 \\ 0 & 0 & \sigma_{v_x}^2 & 0 \\ 0 & 0 & 0 & \sigma_{v_y}^2 \end{bmatrix} \quad (11)$$

The Kalman gain derived by (9) modifies both the a priori state vector  $\hat{x}_k^-$  and covariance matrix  $P_k^-$  while additionally implementing the measurement, in this case the AIS information, from the next time step. Detailed modifications are expressed in (12) and (13), where the  $z_k$  stands for the measurement state vector from the next phase.

$$\hat{x}_k = \hat{x}_k^- + K_k \cdot (z_k - H \cdot \hat{x}_k^-) \quad (12)$$

$$P_k = (I - H \cdot K_k) \cdot P_k^- \quad (13)$$

The iteration proceeds as the a posteriori state vector  $\hat{x}_k$  and covariance matrix  $P_k$



respectively substitute  $\hat{x}_{k-1}$  and  $P_{k-1}$  in (2) and (8). As the Kalman gain  $K_k$  determines the influence of measurement on the a posteriori state, it was speculated that iterative application of the Kalman filter on AIS information could minimize the error and offset which are consistently imposed. Given that the measurement error of AIS information was left unchanged for 10 minutes of acquisition span, this study concluded that the error term from observation could be effectively diminished by using the Kalman filter.

The iterative Kalman filter was applied to dynamic AIS data which was obtained before the target interpolation time derived from the previous section of this study. Final stage speculation implements the a posteriori state vector and covariance matrix for the closest state of measurement before the target interpolation time with the interpolated position data obtained during the estimation of target interpolation time; this interpolated position data substitutes the measurement data for target stage, which is not available. The conclusive result in the state vector format precisely describes the position and velocity of the vessel with respect to the target interpolation time, minimizing the measurement error introduction from the AIS sensor.

## 3.2 Doppler Frequency Shift Correction

### 3.2.1 Theoretical Basis of Doppler Frequency Shift

The SAR image is acquired by synthesizing the echo received from the reflected wave on the scatterer in both range and azimuthal directions. The frequency in the SAR system is often called Doppler frequency, which is frequency susceptible to the variation of slant range [7]. As the major objective of this section was to establish a precise relationship between the vessel in the SAR image and corresponding AIS information, ascertaining the amount of the Doppler frequency shift caused by the instantaneous target movement was indispensable. This section describes and quantifies the Doppler frequency shift, referring to the conventional studies regarding the detection of the maneuvering target inside the SAR image [50-56].

Figure 3-3 illustrates the schematic geometry of SAR platform and the moving target object. The receiving antenna at the platform head is situated at  $(0,0,z_0)$ , where the target is maneuvering from  $(0,y_0,0)$  to  $(v_x\eta, y_0 + v_y\eta, 0)$  with separation of slow time  $\eta$ . An assumption was made that the transmitter was installed only at the head antenna with the receiver, where other antennas behind it only act as receivers [52]. The separation between the adjacent antenna sensors in an identical SAR platform is constant as  $d$ . The object delivers a constant

movement which is left unchanged for a given slow time interval  $\eta$ , both in range and azimuth direction:  $v_y$  and  $v_x$ . The velocity of the SAR platform is denoted as  $V_{sat}$ .

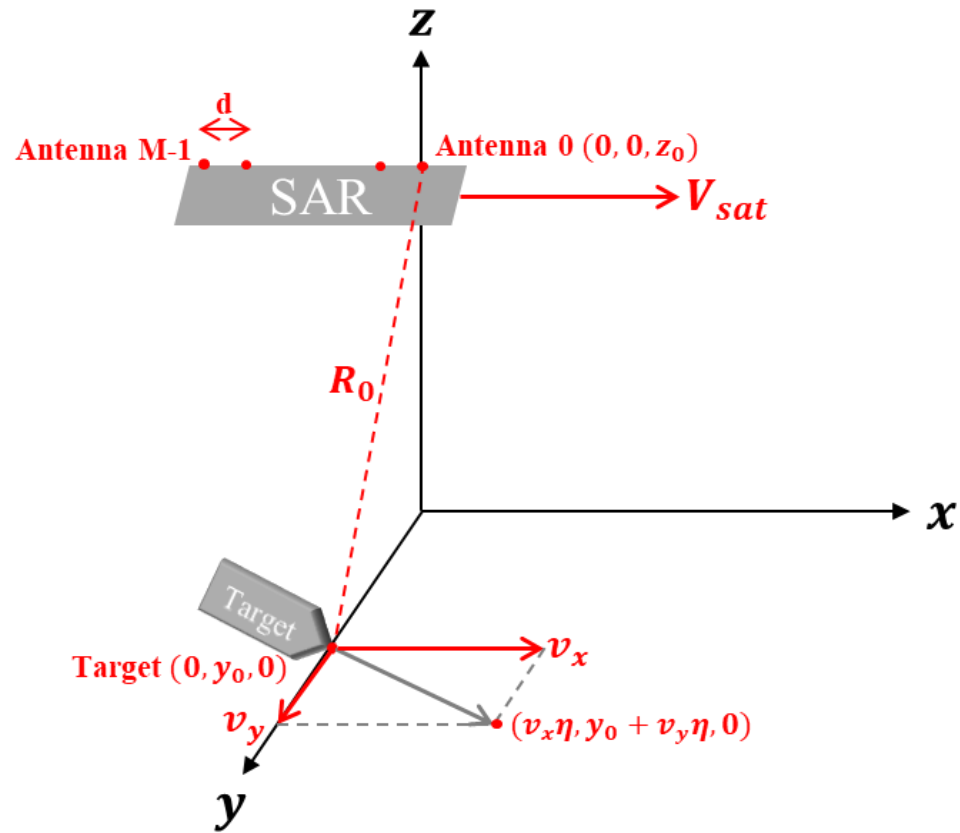


Figure 3-3 Geometry of SAR antenna and the maneuvering target object.

The round-trip slant range  $R_{0m}(\eta)$  could be decomposed as the slant range from the transmitter to the target  $R_0(\eta)$  and the slant range from the target to the receiver  $R_m(\eta)$ , provided that the wave could be received from multiple antennas [53]. From Figure 3-3,  $R_m(\eta)$  could be expressed as (14), where  $m$  describes the order of antenna from zero to  $M-1$ . In addition to (14), previous studies suggested that the Taylor expansion could be implemented with respect to slow time  $\eta$  as approximately expressed in (15) with an order of two [51, 53],

$$R_m(\eta) = \sqrt{((V_{sat} - v_x)\eta - md)^2 + (y_0 + v_y\eta)^2 + z_0^2} \quad (14)$$

$$R_{0m}(\eta) = R_0(\eta) + R_m(\eta) \approx 2R_0 + \eta \frac{2y_0v_y - (V_{sat} - v_x)md}{R_0} + \eta^2 \frac{(V_{sat} - v_x)^2 + v_y^2}{R_0} + \frac{(md)^2}{2R_0} \quad (15)$$

Suggestions were made that the approximated components in the right side of (15) could be substituted by Doppler frequency terms [53, 54]. The first and second order components of the approximation were illustrated as (16) and (17), where the first order term in (16) could be separated into Doppler frequency from antenna location  $f_0$  and that from the target's motion  $f_d$ . Doppler rate of the static target was denoted as  $f_r$  in (20), while that of the maneuvering target was denoted as  $f_{rT}$  in (17) [54],

$$f_{D,m} = -\frac{2y_0v_y - (V_{sat} - v_x)md}{\lambda R_0} = mf_0 + f_d \quad (16)$$

$$f_{rT} = -2\frac{(V_{sat} - v_x)^2 + v_y^2}{\lambda R_0} \quad (17)$$

$$f_0 = \frac{V_{sat} - v_x}{\lambda R_0} d \quad (18)$$

$$f_d = -2 \frac{v_y y_0}{\lambda R_0} \quad (19)$$

$$f_r = -2 \frac{V_{sat}^2}{\lambda R_0} \quad (20)$$

The response signal of the moving target was expressed as (21), after conducting preprocessing the echo signal from the target [52]. The complex image data was obtained for each receiver antenna such that the number of the signal became  $M$ .

$$S(m) = A \text{sinc} \left( B \left( \eta + \frac{\hat{f}_d}{f_r} \right) \right) \exp(-j\pi m \hat{f}_d \frac{d}{V_{sat}}) \quad (21)$$

$$f_d = \hat{f}_d + N_T \cdot PRF \quad (22)$$

Owing to the limitations of PRF, target Doppler frequency is left ambiguous, denoted as  $\hat{f}_d$  in (21). The relationship between  $f_d$  and  $\hat{f}_d$  is expressed in (22), where  $N_T$  designates the folding integer of time domain Doppler ambiguity. From (21), the target is focused while shifted from the conventional position owing to its motion; appearance of the target without velocity in azimuth time domain transpired in  $\eta = 0$ , while the target with motion emerged at  $\eta = -\frac{\hat{f}_d}{f_r}$ . Given the velocity of the SAR platform, the offset generated by the target's motion could be quantified by (23),

$$\delta_{off} = -\frac{\hat{f}_d}{f_r} V_{sat} \quad (23)$$

The majority of the studies on azimuth shift of the moving target concentrated on velocity extraction from the azimuth offset. In such a case, the estimated velocity obtained from the Doppler frequency possessed the ambiguity caused by the PRF limitation. Implementing (23) for reckoning the azimuth shift in this research however, the exact velocity and the Doppler frequency from such velocity could be determined from the dynamic AIS information. It was speculated that the ambiguity of Doppler frequency and the target velocity would be trivial in such a condition. Hence, (23) could be approximated for this research as (24),

$$\delta_{off} \approx -\frac{f_d}{f_r} V_{sat} = -\frac{v_y y_0}{V_{sat}} = -\frac{v_r}{V_{sat}} R_0 \quad (24)$$

The approximation in (24) was also implemented in conventional studies regarding the application of the moving target in SAR images, such as ocean surface waves [57] or measuring it from along-track interferometry (ATI) [58]. Instead of attempting the ascertainment of distance between the nadir and the target to reckon  $y_0$ , line-of-sight velocity  $v_r$  was introduced which could be elaborated as (25) [56].

$$v_r = v_y \frac{y_0}{R_0} \quad (25)$$

In order to calibrate the offset between the interpolated position from the Kalman filter and practical location of the vessel in SAR image, (24) was implemented along with precise measurement of  $v_r$ ,  $V_{sat}$  and  $R_0$ . Typical examples of the azimuth ship owing to the target motion are illustrated in Figure 3-4, describing the

focused vessel isolated from the corresponding AIS path.



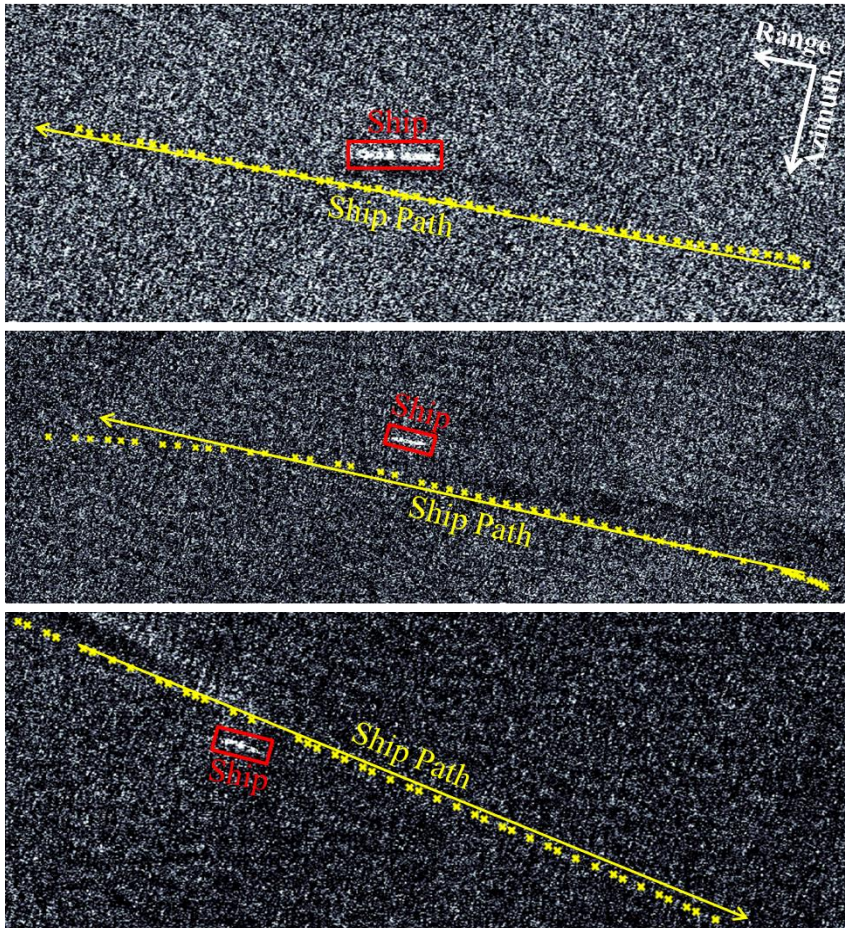


Figure 3-4 Offset between vessels and their paths from dynamic AIS data.

### 3.2.2 Mitigation of Doppler Frequency Shift

As the mitigation of Doppler frequency shift caused by the target motion is necessary, delineation of the three components of (24) ought to be accurately ascertained. This section describes the acquisition of  $v_r$ ,  $V_{sat}$  and  $R_0$  for each vessel.

The outcome of the Kalman filter consists of the style of 2-dimensional state vector which consists of vessel position and velocity in pixel coordinates. The zonal and meridional velocity components were transformed into COG and SOG, following the form of dynamic AIS information. As the expected velocity configuration is the projected velocity towards the SAR satellite, the velocity of the vessel towards COG required an alteration. Figure 3-5 illustrates the transformation of the target motion from the arrangements of COG and SOG to range-projected velocity  $v_y$ . Satellite heading angle is additionally required, which was usually fixed as constant for each SAR satellite. The detailed equation is elaborated in (26), where the SAR satellite heading angle is expressed as  $\theta_h$ . The positive velocity of  $v_y$  was assigned as velocity moving away from the SAR platform, which makes  $v_y$  negative in Figure 3-5.

$$v_y = SOG \cdot \sin(COG - \theta_h) \quad (26)$$

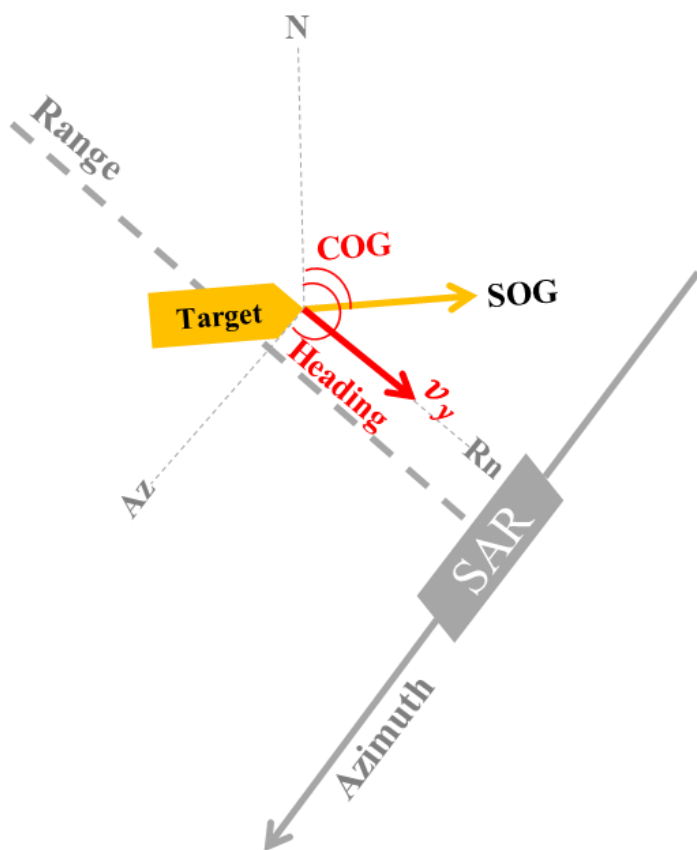


Figure 3-5 Transformation of target motion into range-projected velocity.

In contrast to the range-projected velocity which could be directly reckoned from the previously derived result, slant range and satellite velocity required additional calculation. Precise and accurate measurement of those two parameters required the geocentric 3-dimensional positions of both SAR satellite platform and interpolated AIS sensor. As AIS information contains the geocentric position of the object with respect to the target interpolation time, satellite position corresponding to the object was necessary. This study concluded that the satellite state vector in SAR ancillary data could be appropriate for accomplishing such an objective.

The SAR ancillary data, or annotation file of each SAR image data, contains basic information regarding the SAR platform movement and image acquisition; it contains the precise span of SAR image acquisition, the number of range and azimuth samples, heading angle of the SAR platform, pixel spacing, radar frequency, sampling rate of analog-to-digital converter (ADC), chirp bandwidth, PRF, semi major and minor axis of the Earth ellipsoid, satellite state vectors and the constant interval between them. Application of the satellite state vector for measuring slant range and satellite velocity significantly focused on satellite state vector, denoting the discrete 3-dimensional position and velocity of the SAR platform in geocentric coordinate for 7-8 moments in the case of Sentinel-1 SAR.

Given that each satellite state vector composed of six coordinates of position and velocity, each satellite state vector could be coordinated to an elliptic satellite path. For proper visualization, such an elliptic path was explained using six geometric parameters which were entitled as orbital elements or Kepler parameters [59, 60].

These six parameters include eccentricity ( $e$ ), semi-major axis ( $a$ ), inclination ( $i$ ), longitude of the ascending node ( $\Omega$ ), argument of periapsis ( $w$ ) and true anomaly ( $v$ ) at epoch ( $t_0$ ).

Examinations and analyses on orbital elements were widely conducted in the fields of engineering and orbital mechanics [61, 62]. Eccentricity determines the appearance of an elliptic satellite path, quantifies the amount of the discrepancy between the path and optimal circle. Semi-major axis is the longer axis among the two ellipse axes. Inclination is the offset angle between the elliptic path and the reference plane, assessed at the ascending node of the satellite path. Longitude of the ascending node is measured counterclockwise with respect to the direction of the vernal equinox point. Argument of the periapsis is determined by the angle between the elliptic periapsis and the ascending node. True anomaly denotes the location of the satellite at the target time called epoch  $t_0$ .

Because each satellite state vector consists of a single elliptic satellite path, six orbital elements corresponding to it are designated. Provided that the SAR satellite maneuvers in an ideal elliptic path as the orbital elements demonstrate, each set of elements denotes the presumed satellite path with respect to the corresponding point. Mitigation of the minor differences between the satellite paths is achieved via averaging each component of the orbital elements. This research supposed that this single averaged set of orbital elements and the satellite path delineated by it. Because the SAR satellite orbit includes the acquisition time span of the target SAR image, the satellite path was decomposed with respect to every slow time, azimuth

resolution and PRF; the output format of this procedure followed that of the satellite state vector. The platform velocity  $V_{sat}$  could be derived from the summation of three velocity components of each yielded state vector.

In order to measure slant range between the platform and the target, the interpolated position of each target vessel should be converted to the geocentric coordinate from radar coordinate. As the radiometric and geometric calibrations were implemented prior to the application to this study, it was possible to transform the position expressed as radar coordinates to geographic and geocentric coordinates. For such transformation, the World Geodetic System 1984 (WGS84) was implemented as a reference Earth ellipsoid system for global positioning. The slant range between the platform and the target  $R_0$  was calculated by measuring the distance between two coordinate points. The procedure presented in this chapter was completed by determining the azimuth shift for every ship from (24), and shifting the plotted location of the AIS sensor.

### 3.3 Retrieval of Training Data of Vessels

Precise positions of vessels in the SAR image were derived after interpolation and calibration along with their velocities. This research chapter aims to directly extract the training data for such vessels. Conventional studies implementing AIS information matching the corresponding vessels in SAR image applied dynamic AIS information for evaluating the performance of the detector [23], or complex algorithm such as CFAR [4]. This study, instead, implemented static AIS information containing the interior allocation of AIS sensor with respect to the type of each ship.

The training data for general CNN-based object detection often followed the style of rectangular bounding box. Each bounding box could be represented by four coordinate parameters delineating its position in image coordinates:  $(X, Y, W, H)$ . Locations  $X$  and  $Y$  represent the left-upper point of the bounding box, containing the minimum longitude and maximum latitude. Extents  $W$  and  $H$  denote the width and height of the bounding box, describing the ship span in longitude and latitude respectively. The training data procurement was enabled by deriving the four parameters for each target vessel.

For vessel-wise retrieval of training data, dimension information of each ship along with the interpolated and Doppler shift calibrated position of each AIS sensor and interpolated COG. The COG for each ship was introduced because the calculation varies by four cases, with respect to  $0^\circ$ ,  $90^\circ$ ,  $180^\circ$  and  $270^\circ$ . Correlation

between the dynamic AIS information including the position and COG, and the static AIS information including the dimension of each ship was fulfilled by the Maritime Mobile Service Identity (MMSI) number: an international ship identification number consisting of nine digits.

For all of the cases where  $0^\circ \leq \text{COG} < 90^\circ$ ,  $90^\circ \leq \text{COG} < 180^\circ$ ,  $180^\circ \leq \text{COG} < 270^\circ$  and  $270^\circ \leq \text{COG} < 360^\circ$  the equations implemented in order to derive the four coordinate parameters were presented as (27)-(30), (31)-(34), (35)-(38) and (39)-(42) respectively. *Lon* and *Lat* each describes the interpolated AIS position in longitude and latitude, where DimA-D denote the target ship dimensions.

$$X_{0-90} = \text{Lon} - \text{DimC} \cdot \cos(\text{COG}) - \text{DimB} \cdot \sin(\text{COG}) \quad (27)$$

$$Y_{0-90} = \text{Lat} + \text{DimA} \cdot \cos(\text{COG}) + \text{DimC} \cdot \sin(\text{COG}) \quad (28)$$

$$W_{0-90} = (\text{DimC} + \text{DimD}) \cdot \cos(\text{COG}) + (\text{DimA} + \text{DimB}) \cdot \sin(\text{COG}) \quad (29)$$

$$H_{0-90} = (\text{DimA} + \text{DimB}) \cdot \cos(\text{COG}) + (\text{DimC} + \text{DimD}) \cdot \sin(\text{COG}) \quad (30)$$

$$X_{90-180} = \text{Lon} - \text{DimB} \cdot \cos\left(\text{COG} - \frac{\pi}{2}\right) - \text{DimD} \cdot \sin\left(\text{COG} - \frac{\pi}{2}\right) \quad (31)$$

$$Y_{90-180} = \text{Lat} + \text{DimC} \cdot \cos\left(\text{COG} - \frac{\pi}{2}\right) + \text{DimB} \cdot \sin\left(\text{COG} - \frac{\pi}{2}\right) \quad (32)$$

$$W_{90-180} = (\text{DimA} + \text{DimB}) \cdot \cos\left(\text{COG} - \frac{\pi}{2}\right) + (\text{DimC} + \text{DimD}) \cdot \sin\left(\text{COG} - \frac{\pi}{2}\right) \quad (33)$$

$$H_{90-180} = (\text{DimC} + \text{DimD}) \cdot \cos\left(\text{COG} - \frac{\pi}{2}\right) + (\text{DimA} + \text{DimB}) \cdot \sin\left(\text{COG} - \frac{\pi}{2}\right) \quad (34)$$

$$X_{180-270} = \text{Lon} - \text{DimD} \cdot \cos(\text{COG} - \pi) - \text{DimA} \cdot \sin(\text{COG} - \pi) \quad (35)$$



$$Y_{180-270} = Lat + DimB \cdot \cos(COG - \pi) + DimD \cdot \sin(COG - \pi) \quad (36)$$

$$W_{180-270} = (DimC + DimD) \cdot \cos(COG - \pi) + (DimA + DimB) \cdot \sin(COG - \pi) \quad (37)$$

$$H_{180-270} = (DimA + DimB) \cdot \cos(COG - \pi) + (DimC + DimD) \cdot \sin(COG - \pi) \quad (38)$$

$$X_{270-360} = Lon - DimA \cdot \cos\left(COG - \frac{3\pi}{2}\right) - DimC \cdot \sin\left(COG - \frac{3\pi}{2}\right) \quad (39)$$

$$Y_{270-360} = Lat - DimD \cdot \cos\left(COG - \frac{3\pi}{2}\right) - DimA \cdot \sin\left(COG - \frac{3\pi}{2}\right) \quad (40)$$

$$W_{270-360} = (DimA + DimB) \cdot \cos\left(COG - \frac{3\pi}{2}\right) + (DimC + DimD) \cdot \sin\left(COG - \frac{3\pi}{2}\right) \quad (41)$$

$$H_{270-360} = (DimC + DimD) \cdot \cos\left(COG - \frac{3\pi}{2}\right) + (DimA + DimB) \cdot \sin\left(COG - \frac{3\pi}{2}\right) \quad (42)$$

After the bounding box derivation for each target vessels, all bounding boxes were expanded by a single pixel in four directions with respect to both latitude and longitude to keep the bounding box reduction from being rounded by the spatial resolution. In the case of removing the false AIS signals from the ground station such as the case illustrated in Figure 3-6, the Shuttle Radar Topography Mission (SRTM) DEM was implemented, eradicating the bounding boxes within the DEM coverage. This study assumed that the regions of interest were scarcely influenced by massive subsidence and reclamation. Figures 3-7, 3-8, 3-9 and 3-10 describe the visualization of calculating the four coordinate parameters of the bounding box. Ships that do not follow the rectangular shape could also be fitted inside a rectangular-shaped envelope as presented in Figures 3-7 to 3-10.

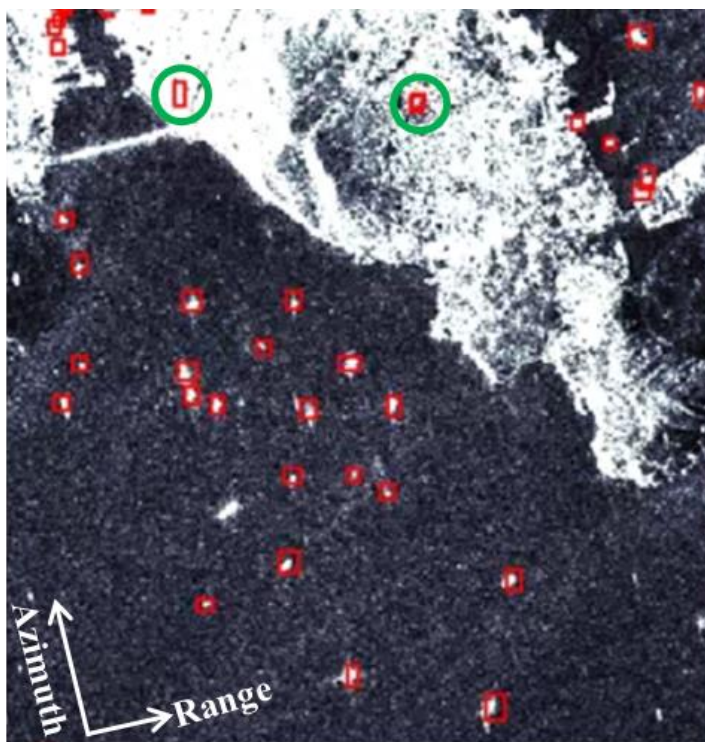


**Figure 3-6 Examples of false AIS signals from ground noted as green circle.**

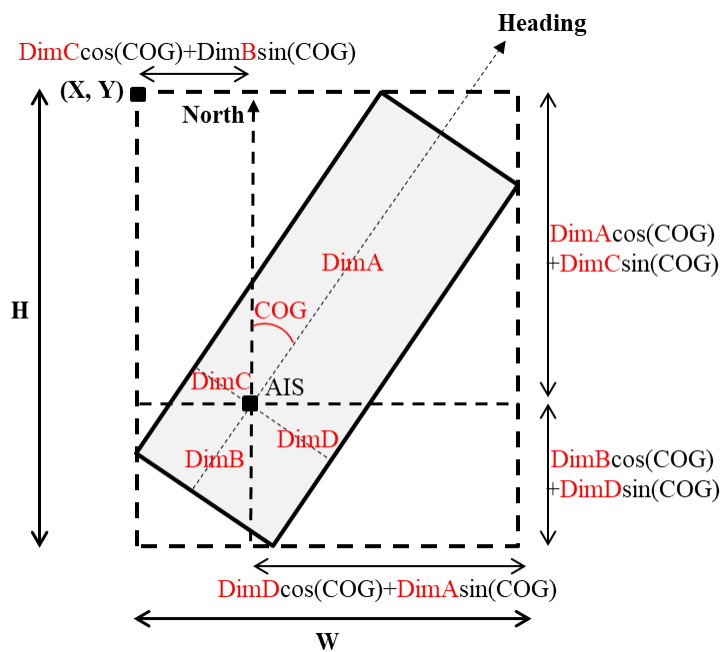


**Figure 3-7 Training data retrieval for the case  $0 \leq COG < \pi/2$ .**

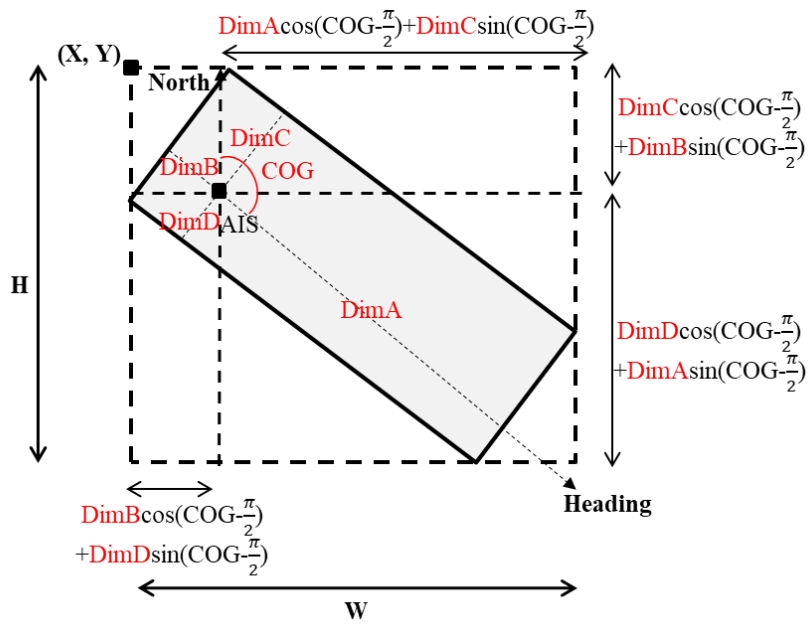


Figure 3-8 Training data retrieval for the case  $\pi/2 \leq COG < \pi$ .

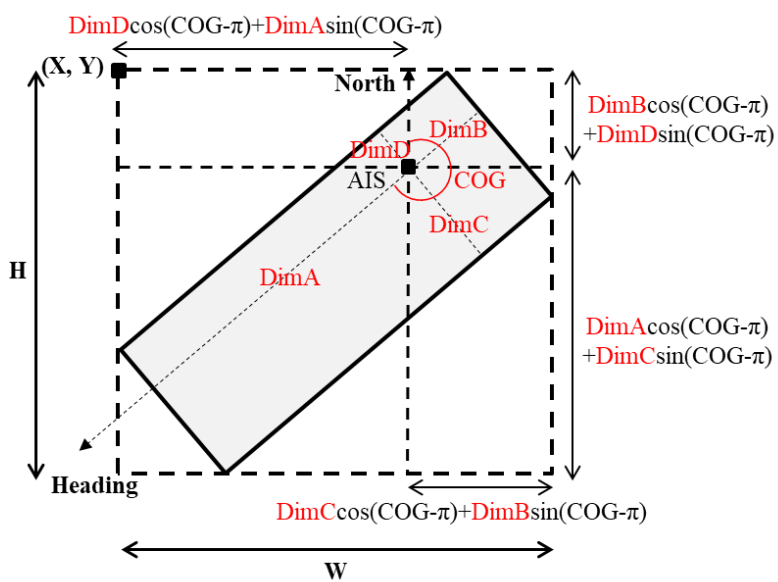


Figure 3-9 Training data retrieval for the case  $\pi \leq \text{COG} < 3\pi/2$ .

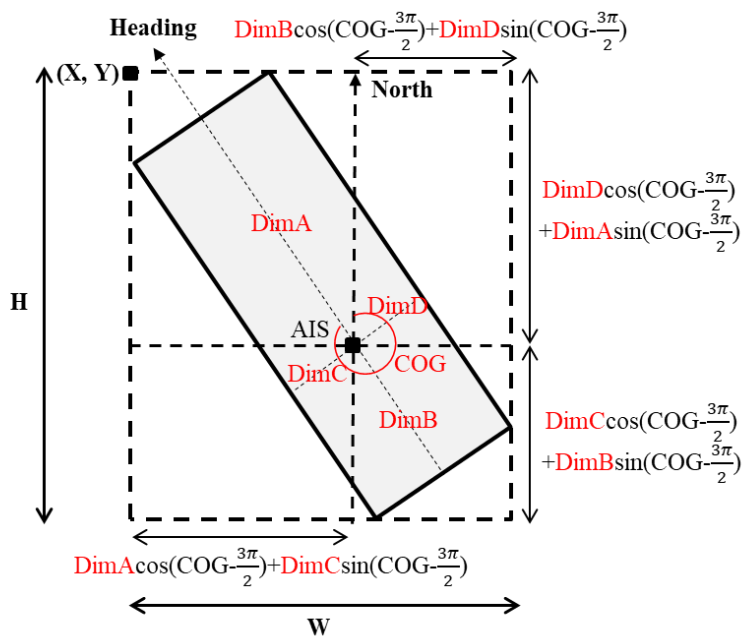


Figure 3-10 Training data retrieval for the case  $3\pi/2 \leq \text{COG} < 2\pi$ .

### **3.4 Algorithm on Vessel Training Data Acquisition from VPASS Information**

In the case of employing VPASS information to render training data targeting small fishing boats, this study devised a different algorithm owing to insufficient information for static VPASS data. As mentioned in Chapter 2, static VPASS data offers length and width of each fishing boats instead of specified information on internal deployment of the VPASS sensor. Owing to this reason and given that the ships are often illuminated as high backscattering coefficients compared to background oceanic conditions [9, 63], training data from VPASS information was acquired from strong radiance points of SAR image.

The training data retrieval algorithm for fishing boat implementing VPASS data followed the first two stages of the proposed algorithm: Interpolation and Doppler Frequency Shift Correction. The algorithm of the two stages could be shared because both dynamic AIS and dynamic VPASS data share an identical format, including MMSI, real-time location of each ship in latitude and longitude, real-time COG and SOG of corresponding ships. The 3<sup>rd</sup> stage, training data extraction from dimension of each ship should be replaced by alternative methodology owing to the lack of dimension information of static VPASS information. Devised from a previous threshold-based ship detection algorithm [64], a new algorithm was introduced based on a threshold, where each training data candidate was binarized by the threshold value of backscattering coefficient.

From interpolated, Doppler Shift calibrated position of each VPASS sensor, the bounding box candidate was derived with respect to the expansion coefficient of bounding box for all four directions, in this case 50 m. The derived interim bounding box was strongly expected to include the target fishing boat's signal, but was also expected to contain the background scatterers. Following the intention of the AIS-acquired training data, the bounding box which included the largest portion of the target fishing boat while having the least portion of the background signal was preferred. Because the pixels with high backscattering coefficient values were regarded as a requisite condition for a candidate ship, it was necessary to sort low-valued pixels from the interim bounding box. This operation was implemented by binarization, where the threshold value, empirically in this case  $\sigma_0 = -10dB$ , acted as a determinator; pixels higher than the threshold survived as a binarized value of 1, where those less than the threshold were eliminated as a binarized value of 0. The surviving pixels after binarization were treated as either target fishing boat signals, or ocean scattering features resembling the target ship.

The additional procedure involving the elimination of such ship-like features was conducted by small object removal. Provided that the ship-like scatterers were smaller than the target ships, the scatterers with magnitude less than the empirical threshold of 10 pixels were considered as oceanic scatterers and were excluded. As the output of this procedure demonstrated the binarized target ship inside the interim bounding box, the bounding box was reduced with respect to the size of the binarized target ship.



The result of the VPASS-based training data retrieval algorithm shared the identical framework of the AIS-based training data: (X, Y, W, H) coordinate marks. All the outputs underwent the DEM-making procedure in order to remove false VPASS signals from the ground.

Although VPASS information elaborated the verified signals from fishing boats under a given time span and spatial coverage, the training data obtained from VPASS information was reduced compared to that from AIS information. The related legislation confirms that not all types of fishing boats are obliged to install a VPASS sensor and their sensors could be silenced when inside harbors [40]. Such regulation conditions reduce the number of fishing boats marked in the desired region compared to the actual number of fishing boats. In this section of the manuscript, it was speculated that a number of fishing boats existed outside of the VPASS surveillance. Figure 3-11 illustrates the existence of a group of fishing boats aligned in an identical direction, but were mostly deprived of VPASS information where Figures 3-11 (a) and (c) covering identical regions of Yeosu. Figure 3-12 illustrates the schematic flowchart of the training data acquisition algorithm for fishing boats implementing dynamic VPASS information.

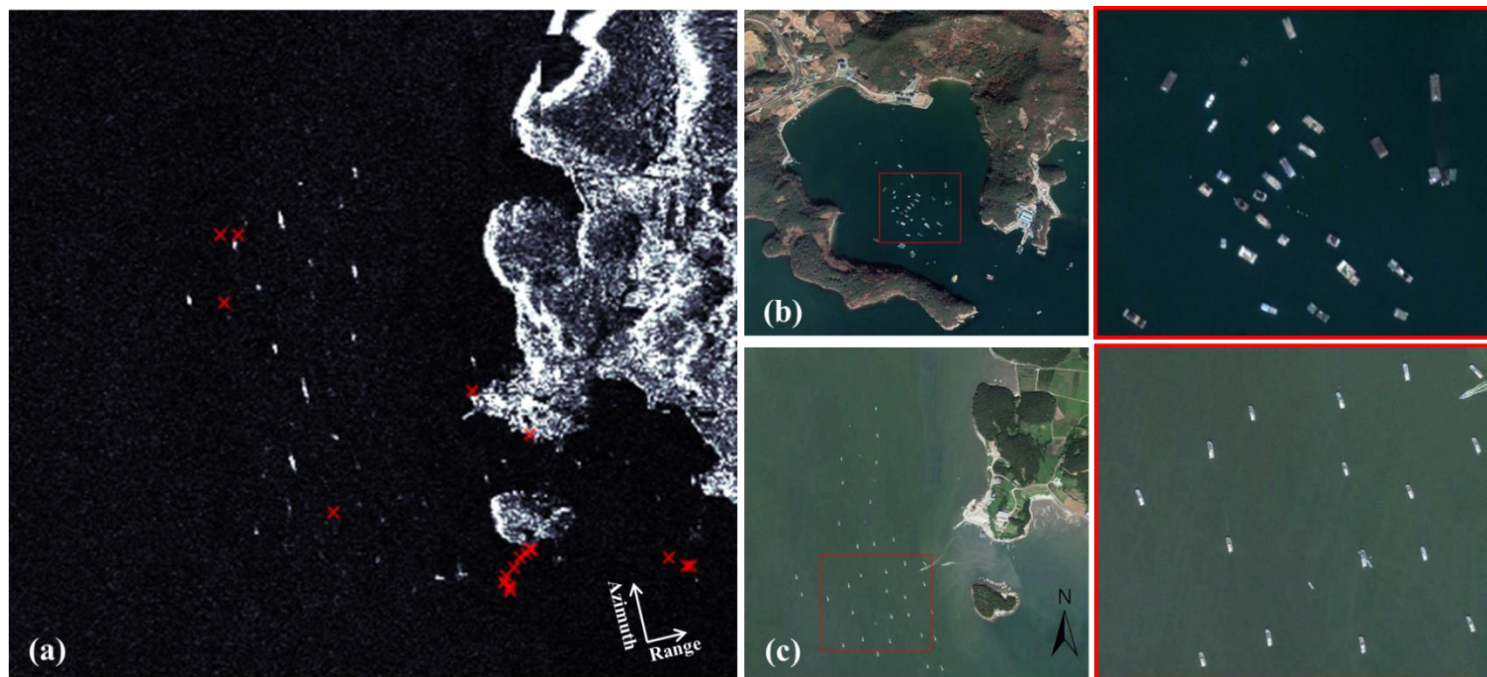


**Figure 3-11 Illustration on (a) VPASS information plotted to Cosmo-SkyMed SAR image, (b) group of non-fishing boats and (c) fishing boats in identical region in optical image from Google Earth.**

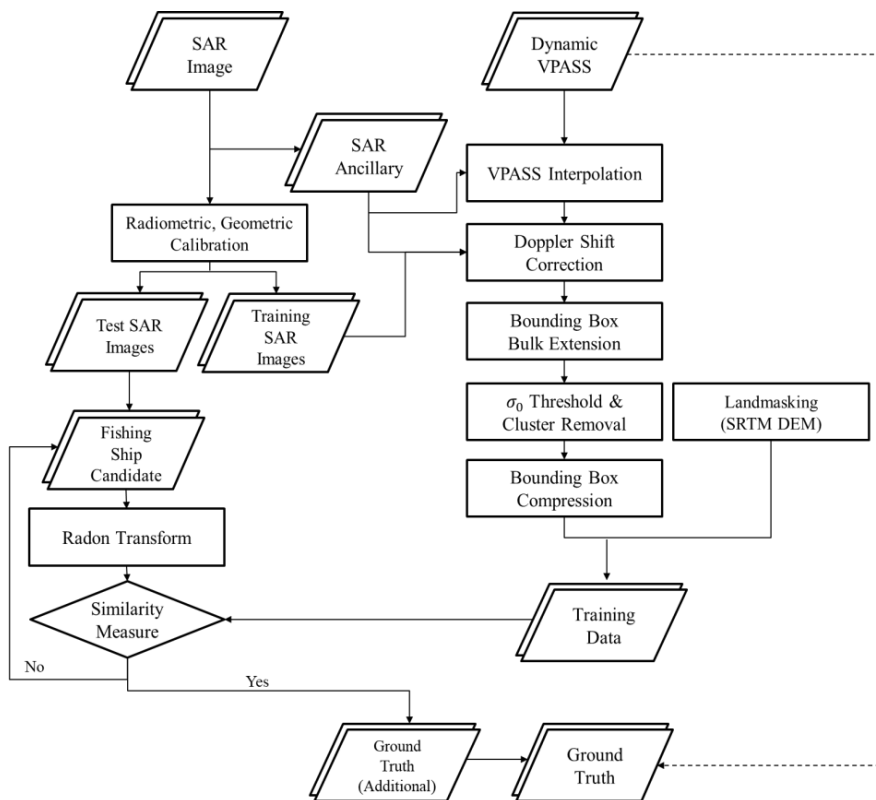


**Figure 3-12 Flowchart of the training data procurement algorithm for VPASS information.**

## **Chapter 4.**

### **Methodology on Object Detection Architecture**

This section of the dissertation elaborates the explicit algorithm of the object detection architecture for current research, which was conventionally proposed in computer vision [65]. Instead of directly implementing the architecture to the detection architecture, the architecture was modified to acquire high detection performance because the major objective of this research was to demonstrate the ameliorated detection performance of the training data from the proposed algorithm in Chapter 3 over the conventional training data obtained via visual inspection. Given such a condition, this study implemented a CNN-based object detector, noted for its efficiency in image interpretation and classification.

The CNN-based object detection algorithm implemented for ship detection is addressed as an Efficient and Accurate Scene Text Detector (EAST), originally proposed in 2017 [65]. As the title of the algorithm suggests, this architecture was originally constructed for detecting text regions inside photography. It was speculated however, that the text regions could also be regarded as objects inside image, which demonstrates a potential of detecting ships and small objects, inside full-sized SAR images. The supremacy of this algorithm over other object detectors claimed by the proposer is that EAST can detect objects of diverse sizes; it was designed as a detector for text regions, which have different sizes in an image depending on the perspective, obscurity and magnitude.

The object detector EAST consists of two major stems of feature extraction and

feature merging. The feature extraction stem literally extracts the characteristic features in each input image. The CNN-based object detector was appreciated for this stage, owing to the calculation of convolution as described in (43),

$$f(x) * g(x) = \int_{-\infty}^{\infty} f(\tau) \cdot g(x - \tau) d\tau \quad (43)$$

The convolution between two continuous functions could be demonstrated via multiplying the functions while moving one function over another. Performance of this calculation derives the correlation of two target functions; the regions in which the two functions are strongly linked with each other demonstrate high value of convolution, and vice versa. The application of (43) to a CNN-based neural network commences from the point where the convolution could be implemented to detecting similarities between two different functions. In a CNN-based neural network, the feature extraction can be conducted as demonstrated in Figure 4-1; when the image patch of which the characteristic feature was desired to be extracted was given as  $g(x)$  or often addressed as a kernel, the target image from which the pattern was to be obtained could be designated as  $f(x)$ . After conducting the convolution, the convolution results where  $f(x)$  demonstrated high value was regarded as the location demonstrating high similarity and correlation between  $f(x)$  and  $g(x)$ .

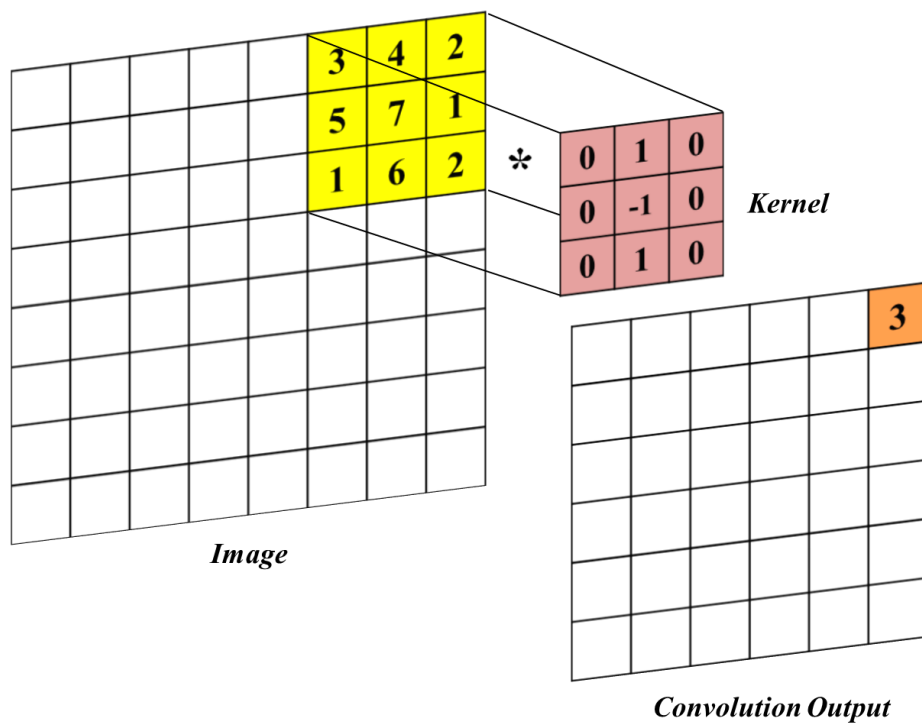


**Figure 4-1 Calculation of convolution in machine learning feature extraction.**

The CNN-based neural network and object detector repeatedly conducts this calculation to extract and compress the desired pattern inside the target image. The convolution layer is often followed by an activation function, which determines whether or not the summation of the input data provokes the activation [66]. This architecture implemented the activation function frequently applied to the CNN-based object detection algorithm: Rectified Linear Union (ReLU). Described as (44), it only activates the input data only when it is positive.

$$ReLU(x) = \begin{cases} x & (x \geq 0) \\ 0 & (x < 0) \end{cases} \quad (44)$$

The pooling layer where the objective is reducing the number of extracted features from the convolution and activation layers often follows the activation layer. An excessive number of features often indicates the hazard of overfitting, where the result of the extracted feature becomes image or case-dependent [67]. Such undesirable consequences could be avoided through reducing, or compressing the features. Reducing the features was mostly conducted through taking the maximum value inside the given window, or averaging the values inside the window; these are respectively addressed as maximum and average pooling. The convolution layer followed by activation and maximum pooling was repeated in order to accurately extract and acquire the features from the original image. Previous studies focusing on the generation of neural network architectures deliberated the combination and allocation of this convolution layer group [68, 69]. This algorithm implemented a feature extraction architecture regarded as obtaining high performance via residual learning architecture, is addressed as ResNet [27].

The accuracy and performance of the algorithm generally increased as the layer depth becomes deeper; however, the saturation of accuracy occurred after a certain depth and drastically decreased afterwards. This issue is referred to as degradation which hinders the optimization of the training architecture. It was claimed that the residual learning architecture of ResNet significantly mitigated such issues, where the layers directly connecting the input and output block labeled as short-cut connections reduce the influence of degradation [27].

The ResNet algorithm contains different variations with respect to the number of layers each one contains: ResNet18, ResNet34, ResNet50 and ResNet101. Its primary constituent included a number of convolutional groups, with each of them composed of three successive convolution layers including a residual structure. With a certain number of layers containing a  $1 \times 1$  kernel size followed respectively by a  $3 \times 3$  kernel size containing an identical number of layers and identical size of kernel with the layers four times larger than if it was composed of a single convolution group. The initiation and termination of each group were connected by a shortcut, named as a residual learning structure. Among feature extractors with residual learning structure, ResNet50 was implemented. ResNet50 consisted of four convolution blocks, each composed of multiple convolution blocks mentioned in the above paragraph.

The input layer of current feature extraction algorithm, ResNet50, was composed of an input layer which offers  $256 \times 256 \times 3$  or  $512 \times 512 \times 3$  as an input image, given that the algorithm was rendered for a 3-channel RGB image [70], slightly modified from the original ResNet50's input of  $224 \times 224 \times 3$ . After the algorithm



implemented a 64-layered convolution with a  $7 \times 7$  kernel, followed by a max-pooling layer and the 1<sup>st</sup> convolutional block was initiated consisting of three identical convolution groups. Each group of the 1<sup>st</sup> convolutional block was composed of convolution layers of 64, 64 and 256 classes, accompanied by a residual learning structure. When implementing the  $512 \times 512 \times 3$  image, the output magnitude of the 1<sup>st</sup> convolutional block would be  $128 \times 128$  with 256 channels.

The other three convolutional blocks consisted of four, six and three convolutional blocks each, of which the depth of the 1<sup>st</sup> layers was expanded to 128, 256 and 512 respectively. The output of each layers consisted of  $64 \times 64 \times 512$ ,  $32 \times 32 \times 1024$  and  $16 \times 16 \times 2048$ , respectively; the magnitude of the output decreased but their depth become deeper as the feature extraction proceeded. It was implied that the algorithmic output extracted in the front convolutional block identified information of small objects and that from the final convolutional block implied information of large objects [65]. As the magnitude of ships inside each SAR image varied, it was speculated that the algorithm should contain another structure which could merge these outputs into a single output.

The feature merging stage was therefore implemented, to merge those four features into a single algorithm. The EAST object detector contained such feature merging which concatenates the extracted output layers of each convolution blocks. However, because the output layers of the convolution box have different magnitude depending on which convolution box they were retrieved from, it would be necessary to unify the two desired output layer magnitudes for concatenation. This issue was mitigated via implementing the upsampling by a factor of two,

because the adjacent magnitudes of the output layers differed by a factor of two. The concatenation was followed by two convolution layers with  $1 \times 1$  and  $3 \times 3$  kernels where the number of layers were designed to reduce the number of the merged layer for the next concatenation.

After three concatenation procedures, the extracted features for both small and large ships were merged and reduced by the intended magnitude. The final layer including a bounding box and score map was separately demonstrated, following the expression of typical form of bounding box in  $(X, Y, W, H)$  for the bounding box and score map determining the class of the detected object. With respect to the number of classes, the score map is consisted of several elements such as (45); the element corresponding to a certain class which has the highest score was selected as the predicted class of the subject. The number of classes is recognized as  $n$  in (45), in case of single-classed ship detection,  $n = 1$ ,

$$x_1 + x_2 + \cdots + x_{n+1} = n \quad (45)$$

The schematic overview of the EAST-based object detection architecture applied in this study is described in Figure 4-2, implementing ResNet50 as the feature extraction stem.

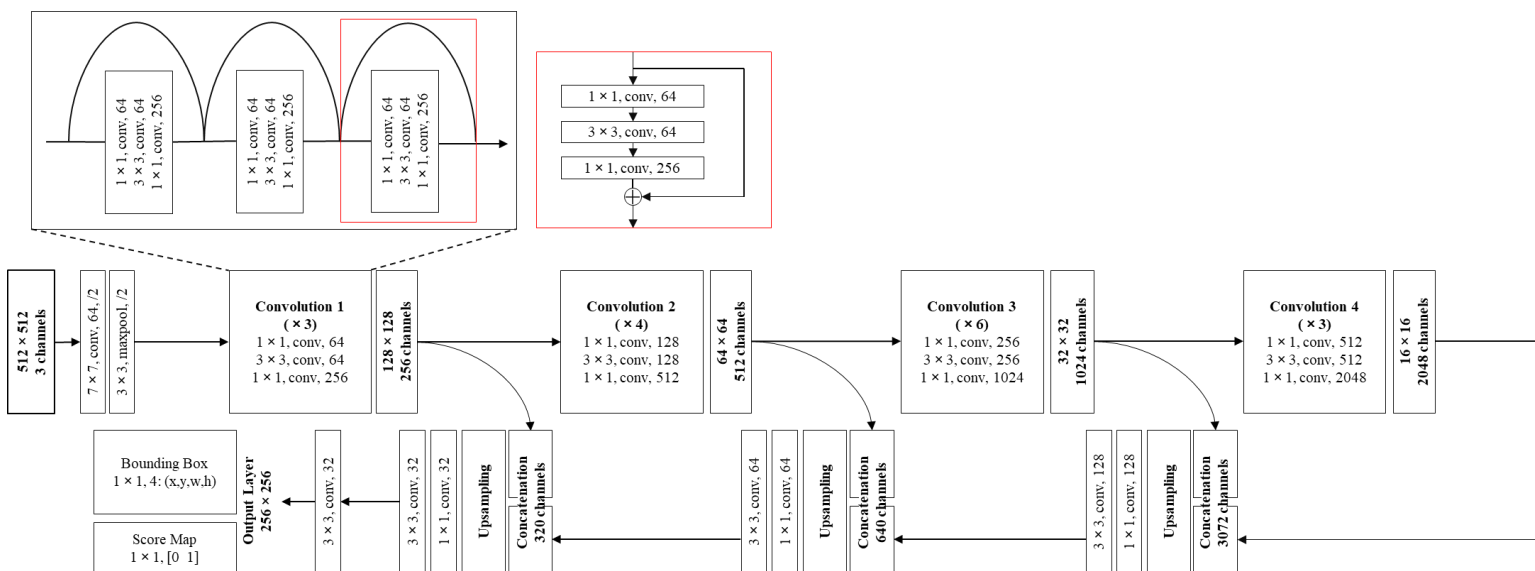


Figure 4-2 Schematic algorithm of EAST-based object detection architecture.

## **Chapter 5.**

### **Results**

This section demonstrates the assessment of the methodology in three parts. Assessment on training data itself without the implementation of the CNN-based detector was first proposed, followed by the AIS-based ship detection assessment comparing the performance between training data from the proposed algorithm and from visual inspection. Finally, the presented results indicated the evaluation from ship detection based on VPASS information.

#### **5.1 Assessment on Training Data**

The accuracy assessment of the training data itself was conducted before elaborating the detection results implementing the automated training data retrieval algorithm. The training data retrieved by the currently proposed training data retrieval algorithm was to substitute the intervention of visual interpretation over obtaining training data. Therefore, ships whose shapes and forms were undeniable both by visual interpretation and by AIS information were selected to ascertain whether the training data obtained from the proposed algorithm could effectively substitute the conventional visual inspection.

Ships that were clearly and visually observable were not contaminated by the ship-like or terrestrial signals, because both ships and those structures emit high backscattering signals towards the SAR satellite [5]. Four ships from the SAR

images acquired on 26/06/2018, 08/07/2018 and 20/07/2018 in the vicinity of southern Korea were chosen; the four isolated ships were chosen far outside the harbor and the contrasts from the background ocean were large enough to be clearly observable via visual investigation.

The algorithm from VPASS training data acquisition was modified to effectively and robustly obtain the visual inspected training data which were implemented as benchmark data. This procedure initiated from the training data obtained from the proposed automated algorithm. From the obtained training data, each bounding box was expanded by a factor of five with respect to each direction of dimension information: DimA-D. All of the four ships for the current algorithm were the ships in which the expanded bounding box included no other ships besides the target ship to remove ambiguity from visual inspection.

Each expanded bounding box went through a binarization. Given that the ships in SAR images are illuminated by high backscattering coefficients [5, 10], it was supposed that the binarization procedure could sort out the pixels not regarded as ships. Binarization divides the entire image into two classes with respect to the given threshold; the pixels that are lower than the threshold were renumbered as 0, the other as 1. The threshold for this procedure was empirically given as  $\sigma_0 = -10dB$ , which could effectively sort out the background signals. Signals from ships and bright ocean scatterers survived as pixel number 1 after this procedure.

Additional removal of ocean clusters was conducted via cluster removal. Ocean clusters in this research were considered as the scatterers connected by less than 15 pixels, because the selected ships in this procedure were clearly observable both in

size and brightness. As the surviving pixels only denote the signals from the target ship in each expanded bounding box, the median point on all of the surviving pixels was determined. From each median point, the bounding box with identical width and height identical to the original bounding box was constructed, referring the median point as its center.

The coverage similarity between the original bounding box and the box from binarization was quantified by Intersection over Union (IoU), a parameter indicating the contrast between the intersection area of two bounding boxes over that of union as expressed in (46), where  $A_{inter}$  explains the intersected area and  $A_{un}$  explains the union,

$$IoU = \frac{A_{inter}}{A_{un}} \quad (46)$$

Figure 5-1 illustrates the IoU-driven evaluation results of the target vessels in offshore region; sub-figures (a) denote the expanded bounding boxes after binarization and cluster removal, where sub-figures (b) describe two bounding boxes, from the automated training data acquisition algorithm in green, and from evaluation algorithm in red. The IoU evaluation parameters for four target ships were reckoned as 0.7522, 0.8182, 0.6970 and 0.7143. Given that the conventional threshold for object detection determining the detection was often offered as 0.5 [71], such evaluation values could be regarded as relatively low accuracy values. In contrast, in the case of the target ship of which the IoU parameter was 0.8182, the offset between two bounding boxes turned out to be two pixels horizontally, without any vertical offset. Such low evaluation was speculated to be caused by the spatial resolution of the Sentinel-1 SAR image. The low spatial resolution of Sentinel-1 IW

GRDH mode derived the small target size of the ship and susceptibility of IoU to offset between bounding boxes.

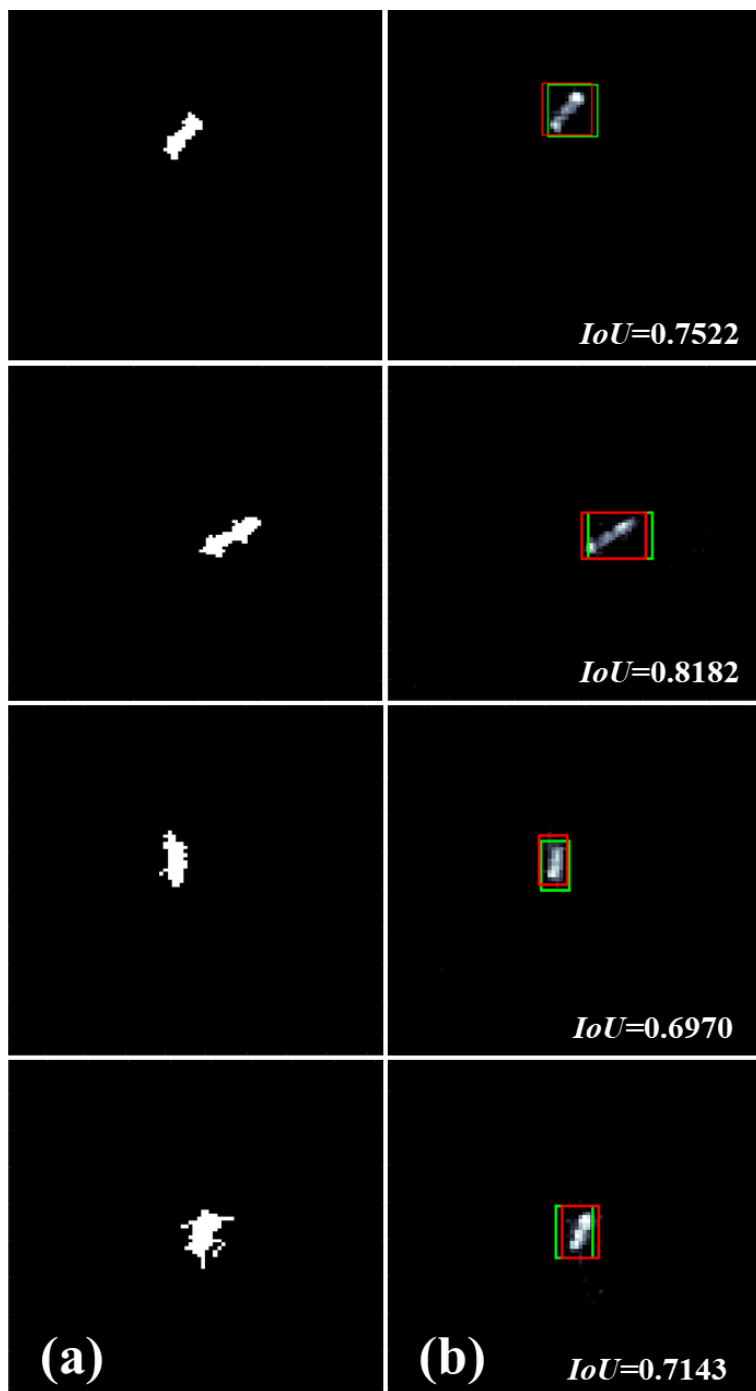


Figure 5-1 Illustration on training data assessment using bounding boxes from binarization and cluster removal.



## **5.2 Assessment on AIS-based Ship Detection**

The evaluation of the training data was once more conducted implementing the CNN-based ship detection architecture. Unlike the assessment from the previous section using binarization, this section focused on evaluating the detection accuracy of vessels in a full-sized SAR image. As the objective of the evaluation was to demonstrate the superiority and practicality of training data acquired from the automated training data procurement algorithm, a benchmark dataset obtained via visual interpretation was additionally constructed.

From the dataset of Sentinel-1 SAR images presented in Table 2-1, this section implemented the portion of it as presented in Table 5-1. The SAR images for ship detection consisted of 21 SAR images covering the southeastern part of the Korean peninsula, including the major harbors of South Korea such as Busan, Ulsan and Pohang. Among those images, 18 images containing 7489 vessels with AIS sensors were implemented for training image data, images from which the training data of ships were obtained, and three images obtained at 26/06/2018, 08/07/2018 and 20/07/2018 containing 1179 ships were selected as test image data, images implemented for testing the pre-trained detector.

**Table 5-1 SAR Images selected for ship detection assessment.**

<b>Satellite</b>	<b>Path direction</b>	<b>Type, Mode</b>	<b>Acquisition time (UTC)</b>	<b>Usage in detection</b>
Sentinel-1A	Ascending	GRDH, IW	26/06/2018 09:23:00~09:23:29	Test
Sentinel-1A	Ascending	GRDH, IW	08/07/2018 09:23:00~09:23:29	Test
Sentinel-1A	Ascending	GRDH, IW	20/07/2018 09:23:01~09:23:30	Test
Sentinel-1A	Ascending	GRDH, IW	01/08/2018 09:23:02~09:23:31	Training
Sentinel-1A	Ascending	GRDH, IW	18/09/2018 09:23:04~09:23:33	Training
Sentinel-1A	Ascending	GRDH, IW	30/09/2018 09:23:04~09:23:33	Training
Sentinel-1A	Ascending	GRDH, IW	12/10/2018 09:23:05~09:23:34	Training
Sentinel-1A	Ascending	GRDH, IW	24/10/2018 09:23:05~09:23:34	Training
Sentinel-1A	Ascending	GRDH, IW	17/11/2018 09:23:04~09:23:33	Training
Sentinel-1A	Ascending	GRDH, IW	29/11/2018 09:23:04~09:23:33	Training
Sentinel-1A	Ascending	GRDH, IW	11/12/2018 09:23:03~09:23:32	Training
Sentinel-1A	Ascending	GRDH, IW	23/12/2018 09:23:03~09:23:32	Training
Sentinel-1A	Ascending	GRDH, IW	16/01/2019 09:23:02~09:23:31	Training
Sentinel-1B	Descending	GRDH, IW	12/09/2018 21:23:52~21:24:26	Training
Sentinel-1B	Descending	GRDH, IW	24/09/2018 21:23:53~21:24:26	Training
Sentinel-1B	Descending	GRDH, IW	18/10/2018 21:23:53~21:24:27	Training
Sentinel-1B	Descending	GRDH, IW	30/10/2018 21:23:53~21:24:27	Training
Sentinel-1B	Descending	GRDH, IW	11/11/2018 21:23:53~21:24:26	Training

Sentinel-1B	Descending	GRDH, IW	23/11/2018 21:23:53~21:24:26	Training
Sentinel-1B	Descending	GRDH, IW	05/12/2018 21:23:52~21:24:26	Training
Sentinel-1B	Descending	GRDH, IW	17/12/2018 21:23:52~21:24:25	Training

Even though AIS information represents verified information on the location and velocity of each ship, the possibility lies that some ships do not contain AIS information especially those with clandestine objectives. Hence, additional annotation on three SAR images were considered beyond automated annotation from AIS information. An assumption was made that most of the ships in the SAR images contained AIS information; the non-automatic annotation was minimized because the incorrect annotation on ground truth data could severely depreciate the detection performance. Therefore, instead of capturing all of the ships in three SAR images without any exception, this study primarily focused on minimizing the imprecise enlargement of the ground truth dataset. Following the identical condition of the previous section, the object with high backscattering condition of which the threshold was defined as  $\sigma_0 = -10dB$  was tentatively selected. From the candidates, the objects whose length was more than twice longer than width was sorted, which was considered as a typical ship appearance. For removing radar scatterer interferometer (RFI) collectivities which show quite similar characteristic with ships, more than five scatterers with the same heading within 50 pixels were considered as RFI and eliminated from the ground truth dataset. Moreover, highly illuminated scatterers in the SAR image render azimuth ambiguity signals in given distances as expressed in (47) [31]. More than two signals in identical pattern from a strong primary scatterer separated by a distance in (47) were regarded as ambiguous signals and were also removed from the ground truth dataset.

$$\Delta_{amb} = \frac{n \cdot PRF \cdot R_0 \cdot \lambda}{2V_{sat}} \quad (47)$$

In (51),  $n$  denotes the order of azimuth ambiguity and  $\lambda$  denotes the wavelength of the SAR system. The examples of the azimuth ghost signals in a portion of the SAR image are illustrated in Figure 5-2, where the distances between the ship and its azimuth ghosts were calculated from (47). The circles in Figure 5-2 denote the ambiguity signals, where green boxes denote the original signals from ships.

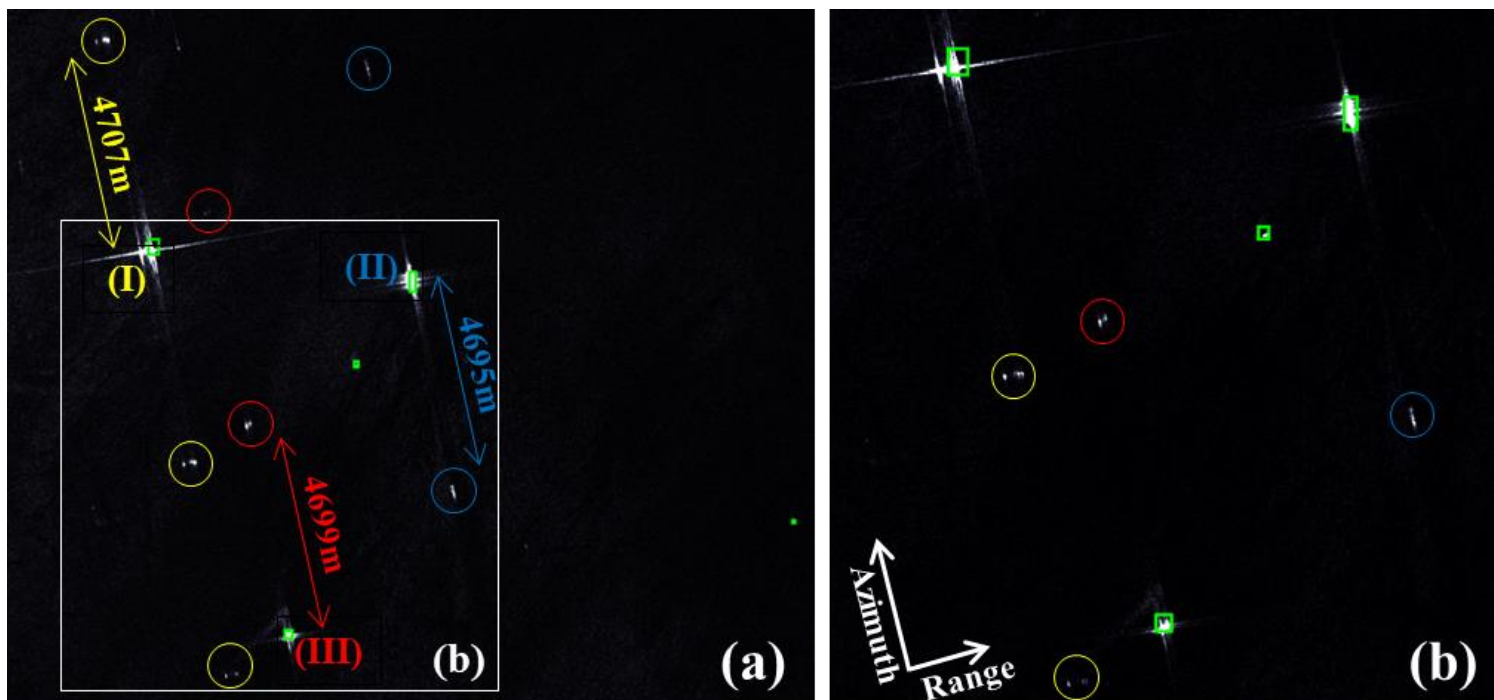


Figure 5-2 (a) Original and (b) enlarged azimuth ambiguity signals and their distance from the original ship scatterers

Regardless of the object's form, it was speculated that the V-shaped wake could only be generated from the movement of ship. The bright scatterer allocated near the converging point of the V-shaped wake was selected as a ship.

In contrast to the additional annotation of AIS-deprived ships in ground truth dataset, benchmark dataset was manually constructed in somewhat different manner. Manual annotation of ship-like structures having high backscattering coefficients higher than  $\sigma_0 = -10dB$  was conducted, in addition to those with V-shaped converging wakes behind them. This benchmark data however, did not consider the appearance of bright scatterer because ships with small magnitude may have a chance of being approximated into a few pixels. In littoral regions or in where artificial structures in the vicinity such as piers and jetties could contaminate the signal from ships, benchmark training data was not annotated. The number of benchmark training data was maintained similar to that of the automatically procured data to keep the number of training data from influencing the detection performance.

The evaluation parameters implemented to quantify the detection performance were precision, recall and F1 score as denoted in (48), (49) and (50);  $N_{acc}$ ,  $N_{det}$  and  $N_{gt}$  each denotes the number of accurately detected vessels, total detection and total ground truth. These three parameters were frequently and conventionally applied parameters for the object detection algorithm, also including the ship detection [29, 65],

$$Precision = \frac{N_{acc}}{N_{det}} \quad (48)$$

$$Recall = \frac{N_{acc}}{N_{gt}} \quad (49)$$

$$F1\ score = 2 \cdot \frac{Precision \cdot Recall}{Precision + Recall} \quad (50)$$

The overall detection performance was represented by the F1 score, which could be driven by the harmonic mean of precision and recall. As precision and recall are in a trade-off relationship with each other [72], their harmonic mean has been applied as a representative detection score.

The parameter to confirm the detection was identically selected as the parameter used in the previous IoU training data assessment chapter. In general, the threshold value for accurate detection was expressed as 0.5 [30]. However, given the low spatial resolution and the susceptibility of training data, it was contemplated that small vessels expressed as a few pixels in the SAR image could have a high possibility of plummeting in IoU even with a trivial discrepancy in the detection result. Therefore, the IoU threshold for deciding whether the detection results match the ground truth was resolved as 0.2.

Training datasets were both trained by the model for 18 images and tested using three images corresponding to the usage of Figure 5-1. As described in Figure 5-2, the ship detection algorithm was trained from automatically retrieved training data demonstrating 80.28% of precision, 74.22% of recall and 77.13% of F1 score, accurately detecting 875 ships from the 1179 ground truth data and detection of 1090 ships. The model trained via training data from visual inspection obtained 59.03% of precision, 66.24% of recall and 62.43% F1 score, precisely detecting 781 ships from 1323 predictions.

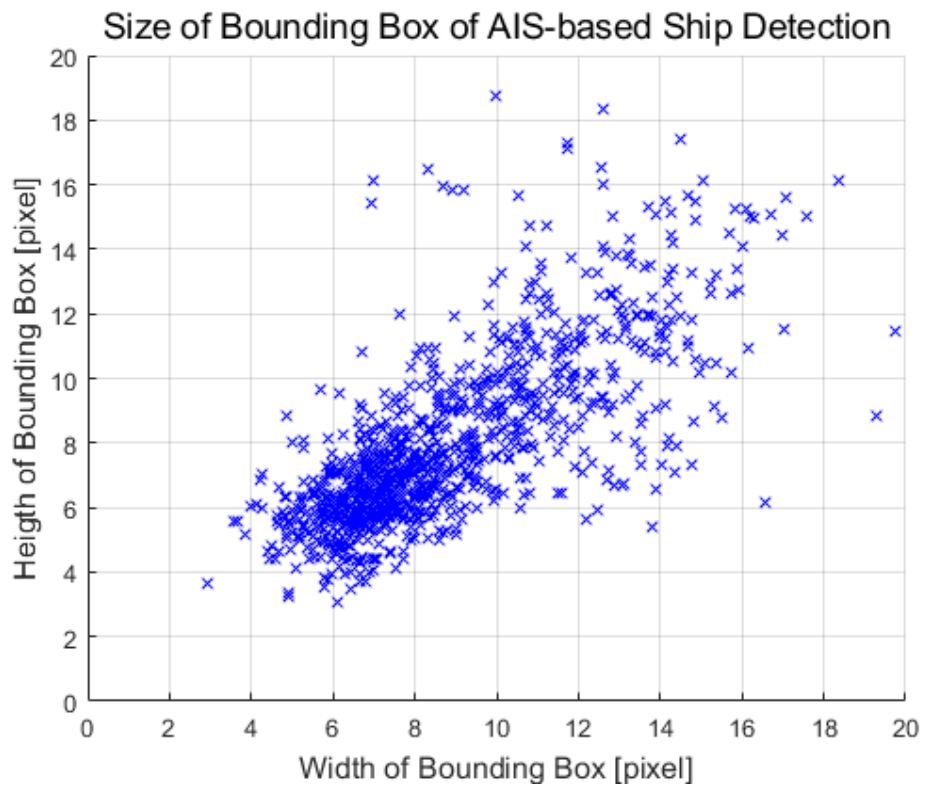


Figure 5-3 illustrates the distribution of bounding box in magnitude, demonstrating the width and height comparison. The minimum width and height of detected bounding box was 58.3057 m and 61.7230 m respectively, where the maximum width and height was 435.2393 m and 480.5878 m respectively.

From the detection results marked in Figure 5-3, the length of each detected ship was inversely estimated, given that the detected bounding box was tightly confined to the actual magnitude of the target ship. After the heading angle estimation, the length of ship was determined by reflecting the heading angle to width of the target bounding box. Figure 5-4 describes a statistical distribution of the length of the ship, where the estimated minimum length of the detected ship was surmised as 80.3056m.

**Table 5-2 AIS-based ship detection performances on two different training datasets.**

Dataset	Acquisition	Precision (%)	Recall (%)	F1 score (%)
Automated	<i>Overall</i>	<b>80.28</b>	<b>74.22</b>	<b>77.13</b>
	26/06/2018	79.62	71.75	75.48
	08/07/2018	82.31	76.25	79.16
	20/07/2018	78.74	74.26	76.43
Manual	<i>Overall</i>	<b>59.03</b>	<b>66.24</b>	<b>62.43</b>
	26/06/2018	69.50	66.95	68.20
	08/07/2018	68.69	64.61	66.59
	20/07/2018	46.42	67.33	54.95



**Figure 5-3 Distribution of width and height of detected bounding box from AIS-based ship detection.**

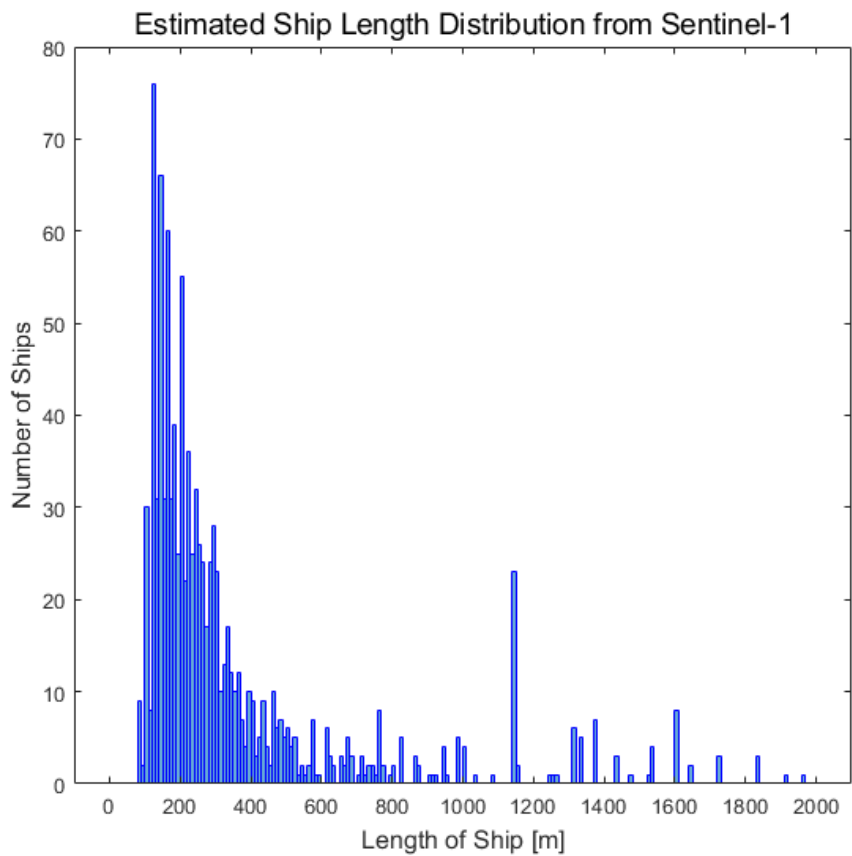


**Figure 5-4 Distribution of estimated length of the detected ships from Sentinel-1 SAR images.**

### **5.3 Assessment on VPASS-based Fishing Boat Detection**

This section on VPASS-based fishing boat detection implemented the portion of SAR images in Table 2-1 as presented in Table 5-3. It includes the ports of Yeosu and Gwangyang, which face the southern coast of the Korean peninsula.

As the operation of one of the real-time sensor was mandatory for vessels [39, 40], fishing boats of which the mass exceeds a certain value have the possibility of attaching an AIS system instead of the VPASS system; this implies that the number of vessel under control of the VPASS system is intrinsically smaller than that of the AIS system. Nevertheless, precise annotation of ground truth data was imperative in deriving reliable and accurate detection performance. An algorithm was devised to define accurate ground truth data for fishing boats using the spectral character of fishing boats.

Spectral comparison of fishing boats for ground truth annotation was initiated by launching a fishing boat database. Its components, signals of fishing boats, were collected from those containing VPASS signals, which could be completely verified as fishing boats. For precise statistical analysis of the fishing boat database, all fishing boats with VPASS information should be aligned into a unified direction. The collected VPASS-based signals were rotated with respect to the angle of interpolated COG, which was derived from the procedure proposed in Chapter 3. Figure 5-5 and 5-6 respectively illustrates the spectral energy ratio of fishing boats accompanied by VPASS information and ships accompanied by AIS information. The chips from Figures 5-5 and 5-6 were respectively obtained from

CSKS2\_SCS\_B\_HI\_04\_HH\_RA\_SF\_20180310210750\_20180310210757 and  
S1A\_IW\_GRDH\_1SDV\_20180801T092302\_20180801T092331\_023051\_0280A4  
\_0E2C SAR images. It is obvious that the energy ratio distribution of the fishing  
boats in Figure 5-5 is smaller and less broadly distributed than that of the ships in  
Figure 5-6.

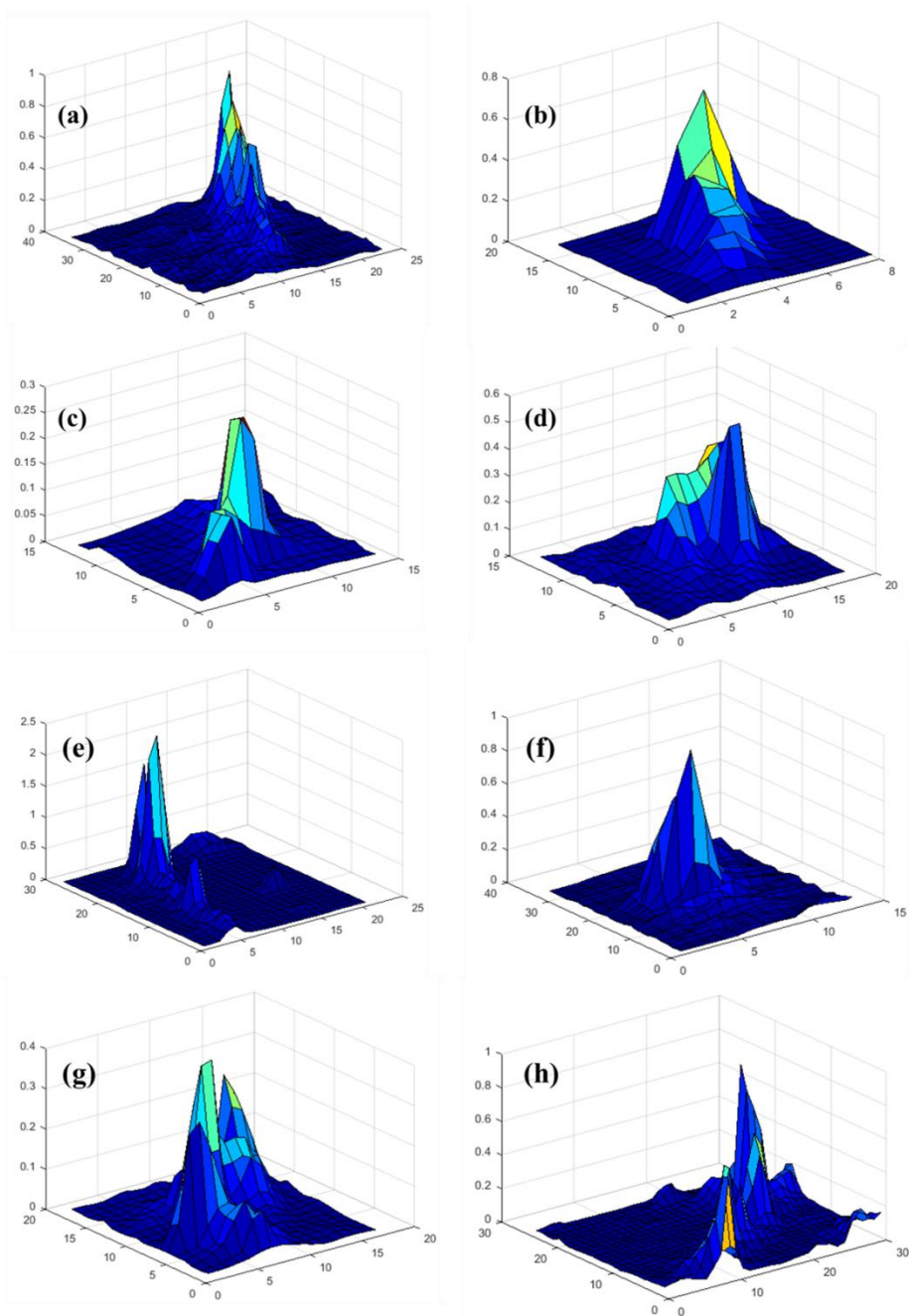


**Figure 5-5 Spectral distribution of training data on fishing boats from VPASS information.**

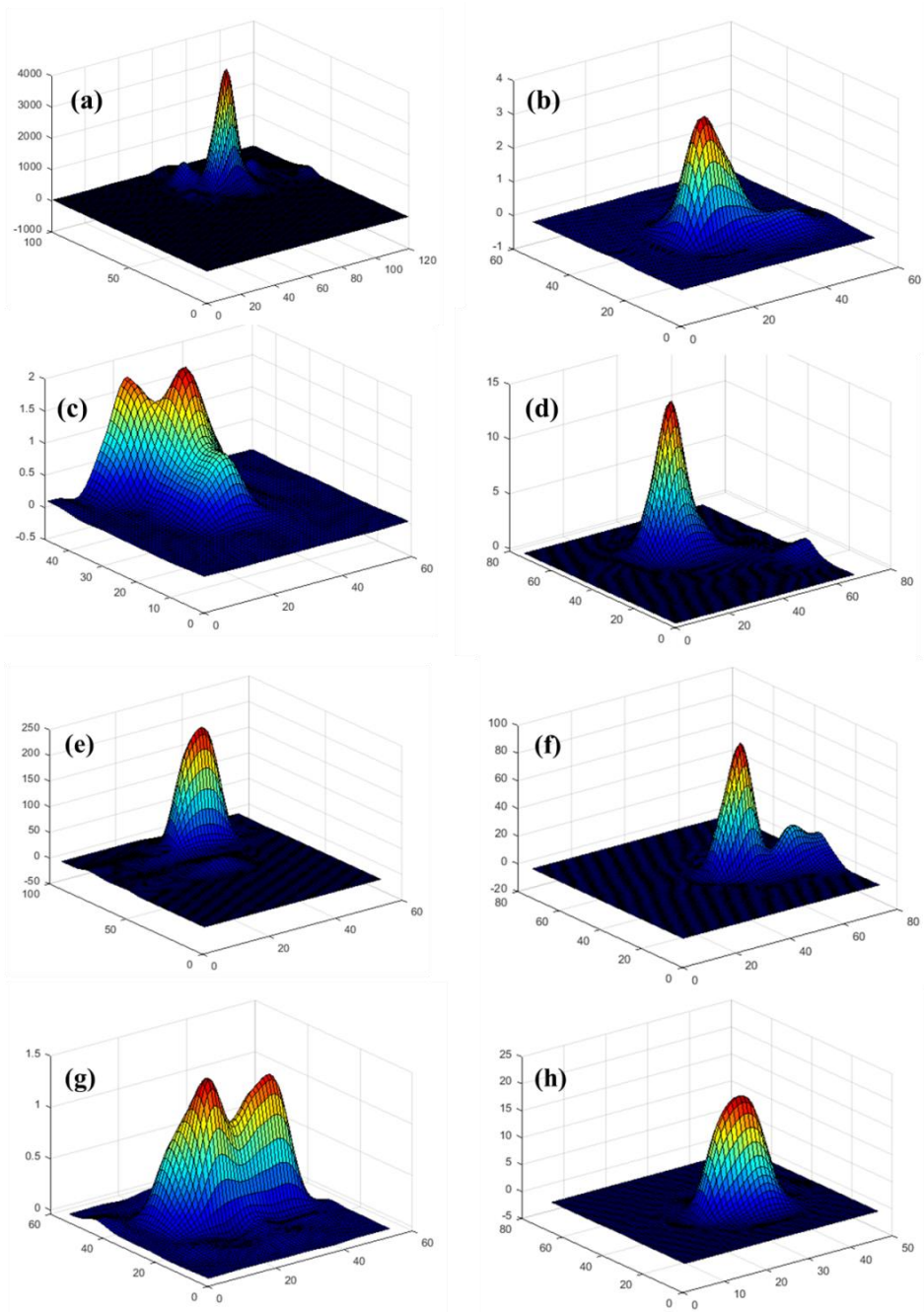


**Figure 5-6 Spectral distribution of training data on ships from AIS information.**



For facile comparison, all signals of fishing boats in the database were resized into  $25 \times 25$  pixels. Whenever a fishing boat candidate is procured, spectral and statistical comparison was conducted after aligning the candidate chip with respect to its maneuvering angle. However, as the candidate was lacking any real-time information on its maneuvering fashion, Radon transform was implemented to estimate the target angle.

Radon transform is the transform that converts images into image line-projection [73]. It selects the line of projection, a linear bin which records the accumulation of image pixels with respect to the orthogonal line of the linear bin. The domain of the initial imagery configured as  $f(x,y)$ , the transformed projection could be demonstrated as  $Rf(x_p, \theta)$ , where  $x_p$  denotes the projected linear bin and  $\theta$  denotes the counterclockwise angle of orthogonal line of projection with respect to the y-axis of the initial imagery. As the projection bin rotates by its angle  $\theta$ , line integration is implemented to initial images by assembling the projected points to the  $x_p$  domain. The exact description of the Radon transformation is described in (51) and Figure 5-7, where  $\delta$  stands for the Dirac delta function and a boundary condition of  $0 \leq \theta < 2\pi$  [73, 74],

$$Rf(x_p, \theta) = \int_{-\infty}^{\infty} \int_{-\infty}^{\infty} f(x, y) \delta(x_p - x \cos \theta - y \sin \theta) dx dy \quad (51)$$

As the output of (51) derives information of projection of the linear feature via peaks of the  $x_p$  domain, Radon transform was frequently implemented in order to discriminate linear features inside the target image such as ship wake, road

centerline, or SAR signal processing [73-77]. In this section, Radon transform was applied to measure the heading angle of each ship owing to the substantial contrast of backscattering of the ship and ocean background.

Provided that all fishing boats are longer in length than width, it was able to measure COG of ship directly from the cropped image via Radon transform. Unlike the previous study of wake detection where the wake was not significantly discernable from the background ocean, the edge detection conducted in advance of the Radon transform was omitted.

After converting the cropped image of ship from the image domain of  $f(x, y)$  to Radon domain of  $Rf(x_p, \theta)$ , the angle  $\theta$  which was perpendicular to the heading angle of the vessel illustrated the highest value because the largest number of signal from the ship was accumulated. The angle  $\theta$  with the largest integration was selected for the estimated heading as the red mark of Figure 5-7 (c); this angle was estimated in the counterclockwise direction while COG was measured clockwise. In addition, it was uncertain whether the ship was facing front or backwards towards the COG. Both cases were considered therefore, rendering two cropped images for examination by rotating the image with respect to measured COG and  $\text{COG} + \pi$  respectively followed by resizing the image into  $25 \times 25$  pixels in order to test the similarity against the fishing boat database.

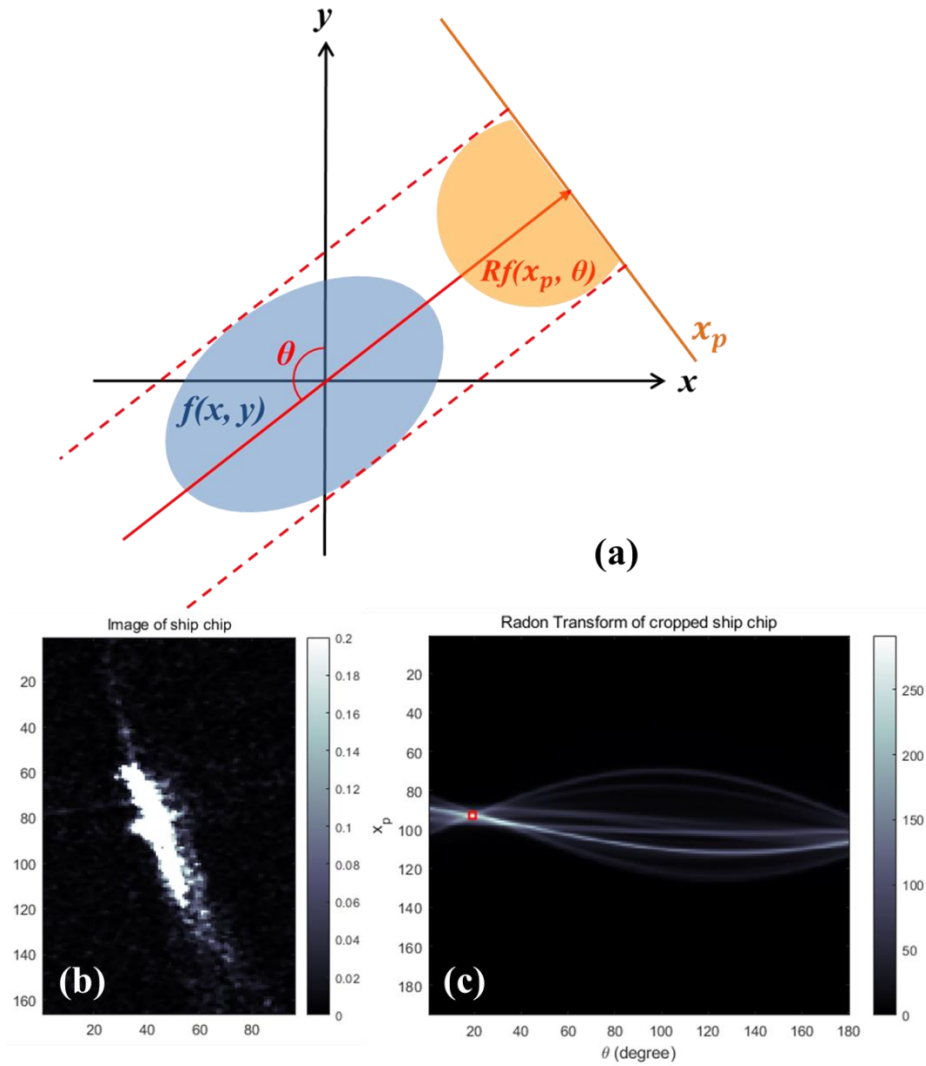


**Figure 5-7** Illustration of (a) schematic description of Radon transform, (b) cropped image of fishing boat candidate and (c) Radon transform of the cropped image.

The similarity between the two fishing boat candidate images and VPASS-based fishing boat database was evaluated by three parameters: structural similarity, root mean square error and correlation coefficient. The structural similarity index (SSIM) is an index to measure image resemblance by estimating luminance, contrast and structure [78]. Identical images would have maximum SSIM of one, dropping as the two images diversify. With simplification and presumption to a certain degree [78], the SSIM could be calculated as (52), where  $\mu$  addressing the mean intensity of image  $x$  and  $y$ ,  $\sigma$  denoting the variance and  $C$  denoting the constant which depends on the dynamic range of pixels,

$$SSIM(x, y) = \frac{(2\mu_x\mu_y + C_1)(2\sigma_{xy} + C_2)}{(\mu_x^2 + \mu_y^2 + C_1)(\sigma_x^2 + \sigma_y^2 + C_2)} \quad (52)$$

The root mean square error (RMSE) estimates the average of pixel difference of two images as described in (53), where similar image pairs demonstrate lower square error values [79]. The total number of image pixels of images  $x$  and  $y$  is described as  $n$ ,

$$RMSE(x, y) = \sqrt{\frac{1}{n} \sum_{i=1}^n (x_i - y_i)^2} \quad (53)$$

The correlation coefficient evaluates the degree of relation between the image pair of  $x$  and  $y$ , measuring similarity of the disposition of pixels implementing (54) [80]. The identical pair would have the correlation coefficient of 1, while the value decreases as the image pair patterns diversify.

$$Corr = \frac{\sum_i \sum_j ((x_{ij} - \mu_x)(y_{ij} - \mu_y))}{\sqrt{\sum_i \sum_j (x_{ij} - \mu_x)^2} \sqrt{\sum_i \sum_j (y_{ij} - \mu_y)^2}} \quad (54)$$

It was assumed that as the fishing boats have identical usage, they would demonstrate similar internal structures and scattering characteristics. According to such an assumption, the candidate chip should demonstrate high affinity in three evaluation parameters on more than a single fishing boat in the database. Hence, it was necessary to select the proper threshold value for three parameters to determine whether the candidate chip belonged to the fishing boat database.

From inside the fishing boat database with VPASS information, three evaluation parameters were evaluated for each chip with the others. For each chip, the maximum value of SSIM and correlation, with a minimum value of RMSE was respectively selected and median values among all fishing boats in the database were estimated. The chips from nine Cosmo-SkyMed SAR images derived the critical value of SSIM as 0.73477, RMSE as 0.037782 and correlation coefficient as 0.79. If the candidate chip exceeds all three evaluation parameters, the target ship was regarded as emitting comparable scattering signal to conventional fishing boats and selected as a fishing boat.

Figure 5-8 illustrates the performance of the annotation algorithm from Cosmo-SkyMed SAR image evaluated by the three parameters of (52), (53) and (54). The green bounding box represents the training data obtained from VPASS information, while the red circle illustrates the position of a chip in the SAR image. For the tested fishing boat having similar scattering characteristics with the other fishing boat in the database demonstrated high value for all three parameters comparable to the threshold value. In contrast, when the large non-fishing boat exhibiting distinctive internal structure and character was tested, it failed to surpass the

threshold by a large margin.

Figure 5-9 describes the assessment of the annotation algorithm on artificial scatterers similar to fishing boats, acquired in the vicinity of the Yeosu airport. It includes 14 airplane landing lights aligned in the inshore ocean, as marked by yellow boxes in Figures 5-9 (a) and (b). According to the proposed annotation algorithm via comparison on scattering characteristics, it left two false annotation as fishing boats by a red circle, while accurate discrimination of 12 objects in blue cross marks.

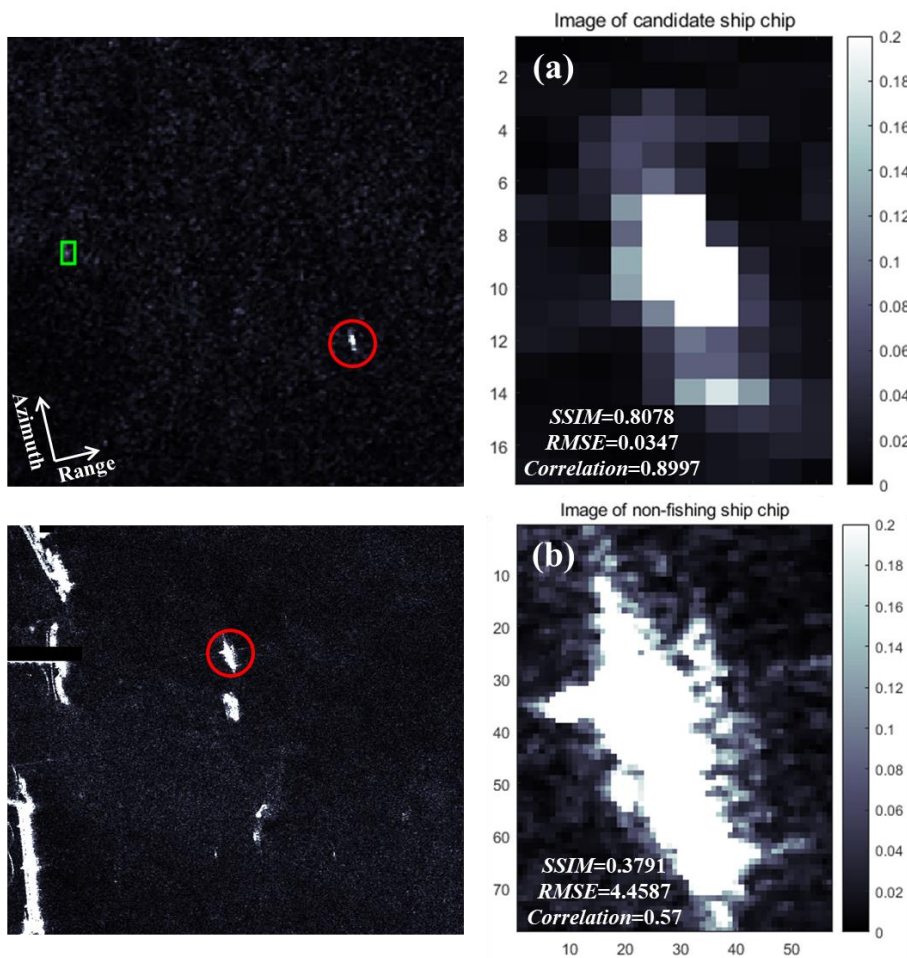


**Figure 5-8 Description of annotation assessment and database-based evaluation on a (a) fishing boat chip and (b) non-fishing boat chip.**

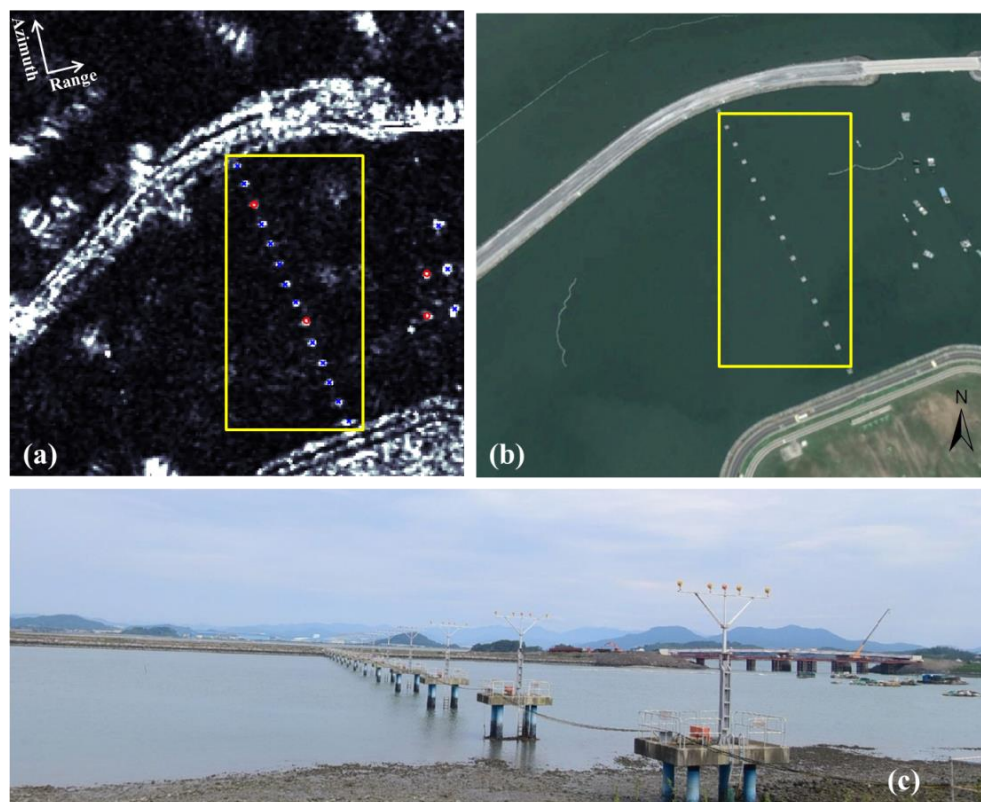


**Figure 5-9 Assessment on annotation algorithm on airplane landing lights (a) in Cosmo-SkyMed SAR image with (b) cropped image from Google Earth and (c) photographic road view on the identical region.**



A major difference between the two detection cases of AIS-based ship detection and VPASS-based fishing boat detection was the magnitude of the bounding box. Owing to the diversity of the type of ship, the magnitude of AIS-driven training data is varied. However, as VPASS data contains exclusive information on fishing boats, the diversity of the bounding box scope is lower than that from AIS information. Under such conditions, the importance of training data rises because the object detector was required not only to discern ship-like scatterers as in Chapter 5.2, but also to discriminate ships with different objectives other than fishing.

As the Cosmo-SkyMed SAR images in this study were single-banded, the HH-polarized SAR image was duplicated as a mimic of the double-band SAR image of Sentinel-1 with incidence angle to match the desired form of the ship detector. This led the SAR images for VPASS-based fishing boat detection to have an identical format with that implemented for the AIS-based ship detection.

**Table 5-3 SAR Images selected for fishing boat detection assessment.**

<b>Satellite</b>	<b>Path direction</b>	<b>Type, Mode</b>	<b>Acquisition time (UTC)</b>	<b>Usage in detection</b>
CSK1	Ascending	Stripmap, Himage	08/07/2018 21:08:08~21:08:15	Training
CSK2	Ascending	Stripmap, Himage	10/03/2018 21:07:50~21:07:57	Test
CSK2	Ascending	Stripmap, Himage	13/05/2018 21:07:59~21:08:06	Test
CSK2	Ascending	Stripmap, Himage	13/03/2019 21:08:11~21:08:19	Training
CSK2	Ascending	Stripmap, Himage	16/05/2019 21:08:20~21:08:27	Training
CSK4	Ascending	Stripmap, Himage	09/01/2018 21:07:42~21:07:49	Training
CSK4	Ascending	Stripmap, Himage	06/09/2018 21:08:08~21:08:15	Training
CSK4	Ascending	Stripmap, Himage	09/11/2018 21:08:15~21:08:23	Training
CSK4	Ascending	Stripmap, Himage	12/01/2019 21:08:12~21:08:20	Training

The three evaluation parameters for AIS-based ship detection, precision, recall and F1 score, were additionally implemented to fishing boat detection as it was determined that both AIS-based ship detection and VPASS-based fishing boat detection were intrinsically regarded as object detection in SAR images. The object detector algorithm for fishing boat detection followed the identical algorithm as the AIS-based ship detection in order to determine the detection performance under similar equipment conditions.

As previously mentioned in Chapter 3.4, the additional annotation for fishing boats was applied in order to construct the precise ground truth data for accuracy assessment. Implementing seven SAR images from Table 5-3 containing 2061 chips, the object detection algorithm ascertained its performance of fishing boat detection in two SAR images respectively containing 498 ships for the SAR image taken on 10/03/2018 and 683 ships for that taken on 13/05/2018. The IoU constraint for accurate detection was diminished from 0.2 for AIS-based detection to 0.15, given the smaller magnitude of fishing boats. From the image obtained on 10/03/2018, the detector identified 687 objects as fishing boats where 334 of them were accurate and in the case of the image from 13/05/2018, 833 objects were identified where 454 of them were regarded as precise detections. The precision, recall and F1 score from SAR images acquired in 10/03/2018 and 13/05/2018 respectively demonstrated 48.62%, 67.07%, 56.37% and 54.50%, 66.47%, 59.89% as seen in Table 5-4.

Figure 5-10 demonstrates the bounding box distribution for fishing boats in magnitude, demonstrating the width and height comparison. The minimum width

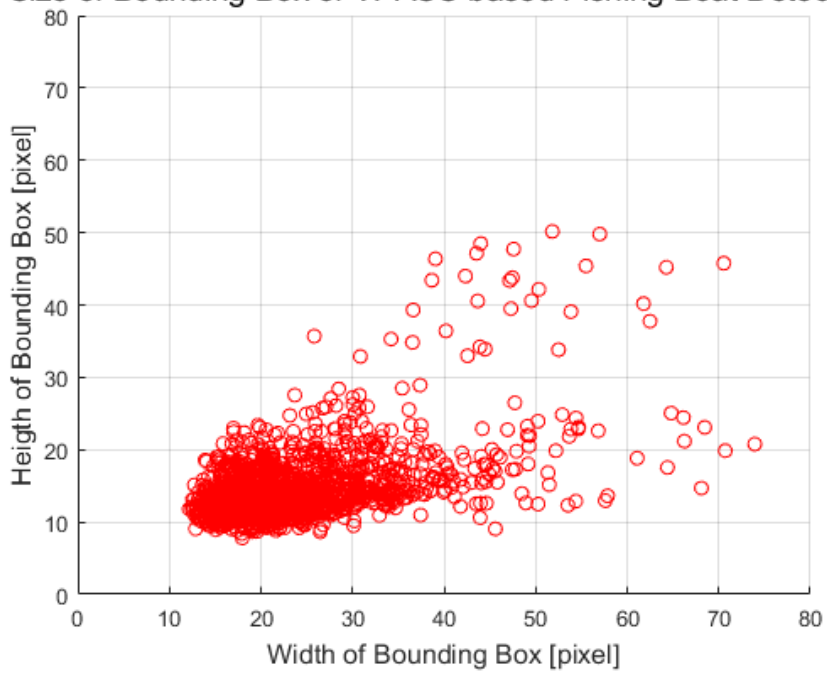
and height of the detected bounding box was respectively 36.4950 m and 23.3954 m, where the maximum width and height was respectively 346.1446 m and 262.2244 m.

Figure 5-11 elaborates the distribution of length of the detected fishing boats, acquired from the identical procedure deriving Figure 5-4. The estimated minimum length of the detected fishing boat was measured as 37.5315 m.

**Table 5-4 VPASS-based fishing boat detection performances.**

	<i><b>Overall</b></i>	<b>10/03/2018</b>	<b>13/05/2018</b>
Precision (%)	<b>51.84</b>	48.62	54.50
Recall (%)	<b>66.72</b>	67.07	66.47
F1 score (%)	<b>58.35</b>	56.37	59.89
Accurate Detection	788	334	454
Total Detection	1520	687	833
Ground Truth	1181	498	683

Size of Bounding Box of VPASS-based Fishing Boat Detection



**Figure 5-10 Distribution of width and height of detected bounding box from VPASS-based fishing boat detection.**

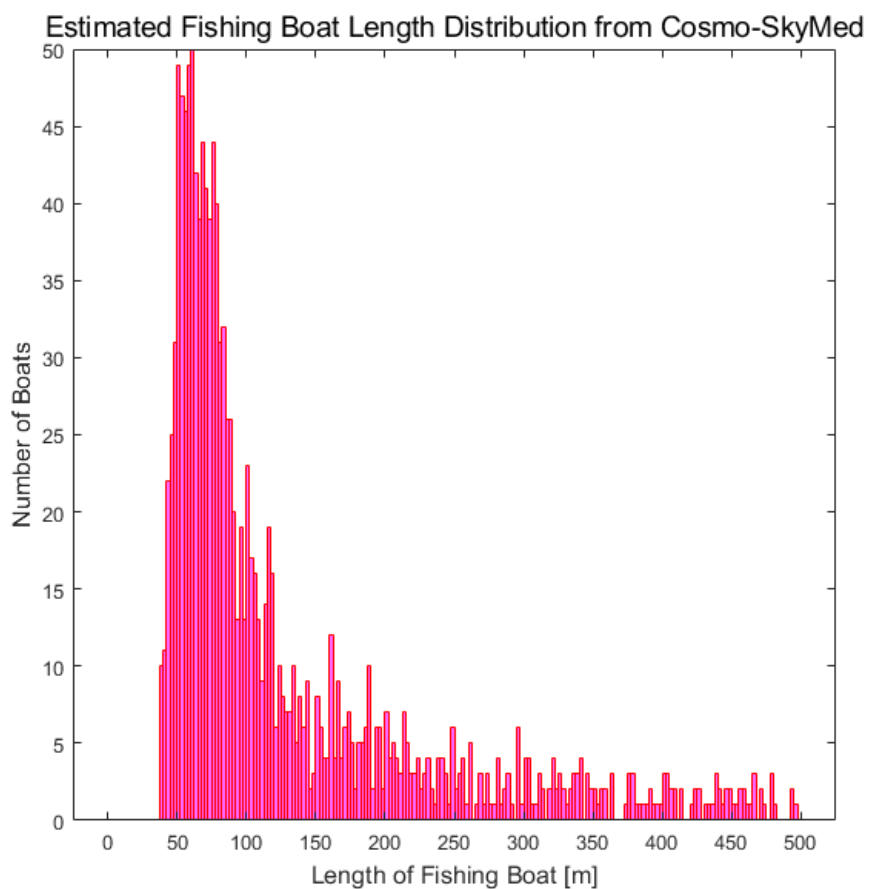


**Figure 5-11 Distribution of estimated length of the detected fishing boats from Cosmo-SkyMed SAR images.**

## **Chapter 6.**

### **Discussions**

This section was separately elaborated for ship detection high detection accuracy of automatically procured training data and fishing boat detection illustrating the possibility of application to monitoring unclassified vessels.

#### **6.1 Discussion on AIS-Based Ship Detection**

Owing to the difficulties in profoundly obtaining ships in SAR images, a substantial majority of studies on this issue focused on modifying the CNN-based object detection architecture [23, 29, 30, 81, 82]. In such conventional studies, training dataset of ships for ascertaining the performance of a recently developed model was obtained without scientific determination and through visual inspection. It was noted that complete reliance on visual interpretation could obstruct the application of such technique to practical purposes. This study attempted to fundamentally remedy such issue by procuring robust and verified training data that indicates the location and velocity of each ship: AIS information. It not only improves upon the previous attempt to construct the database of ships by cropping the SAR images containing them [38], but also robustly and precisely retrieves the scattering pixels of ships as described in Chapter 5, via the use of AIS information on ascertaining the detection performance. Previous studies regarding the projection



of AIS information on SAR images often used complex domain transfer [36] or statistical calculations [83] because the majority of them focused on dynamic AIS information. Here, implementing both dynamic and static information, this study managed to establish a simple and direct connection between AIS information and ship signals in SAR images. Additional discussion on exact interpolation time was conducted in order to ascertain the precise allocation of each ship.

Table 5-2 presents the ship detection performance contrast between two different training databases. It is clear that the ship detection model trained from the database acquired from the proposed algorithm apparently exceeds that acquired from visual inspection: 77.13% overall and 79.16% in a typical image versus 62.43% overall and 68.20% in a typical image. Previous ship detections were conducted under much more hospitable conditions compared to those in this research: clear superstructure of vessels owing to advanced spatial resolution [82], sparse vessel allocation between one another owing to offshore coverage of SAR image [74] and minimal coverage containing fewer vessels [23]. Given those conditions, ship detection models achieved detection performances greater than 90% [23, 74, 82]. In contrast, as this research on ship detection intended to generate a robust algorithm which could operate without image-dependency, focused on rendering a verified training data and managed to obtained complementary detection performance with the study using Sentinel-1 SAR test images with 1348 ships and the newly proposed detection model [29]. Hence, it was deduced that the detection performance similar to [29] was from the training dataset using the proposed training data procurement algorithm.

The typical illustration of the ship detection result is shown in Figure 6-1. The specified region of interest was magnified to the inshore region and the post with azimuth ghost signals from ships around them. The originality of the training data procurement algorithm lies at these two regions in which the training architecture effectively detected the ships docked in port and evaded the ghost signals from detection, of which the detection result substantially exceeding that from visual inspection. Green, red and orange boxes in Figure 6-1 each denotes the ground truth, detection results and magnified regions respectively, where sub-figures (a) and (b) respectively display the detection results from SAR images acquired in 08/07/2018 and 20/07/2018. Sub-figures (d) and (g) display the results from training data obtained via proposed algorithm, where (e) and (h) display the results from training data obtained from visual interpretation. Yellow circles in sub-figure (f) identify the azimuth ghost signals.

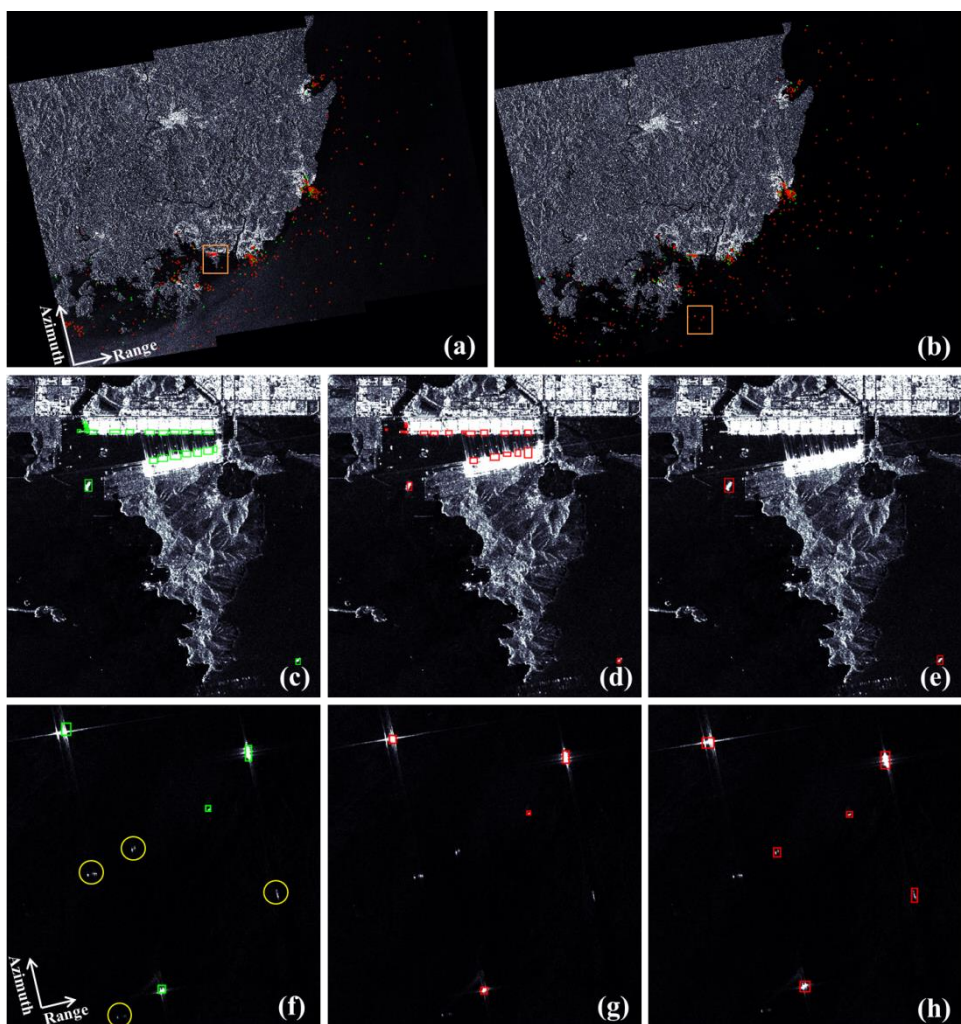


**Figure 6-1 Typical illustration results of contrast between two different training datasets of AIS-based ship detection.**

Analogous academic obstacles between previous studies related to ship detection could be categorized into four issues: monitoring of AIS deprived vessels, mitigating ship detection performance where ships were densely allocated, controlling the detector from detecting ship-like structure and acquiring massive and accurate training data for ship detection architecture. Monitoring ships without AIS information was successfully accomplished via AIS-annotated vessels. There were vessels with the positioning system turned off, regardless of the type, superstructure and magnitude; instead, this often depended upon the clandestine purpose of the vessel, illegal fishing and martial operations [84]. Therefore, it was concluded that models trained via AIS information could successfully detect the AIS-deprived ships. Detecting vessels in ship-compacted regions demonstrated high detection performance because AIS-annotated training data was procured in inshore regions, as briefly illustrated in Figure 6-1. Unlike the conventional training data via visual inspection, training data from the automated training data acquisition algorithm effectively trained the detector to discriminate the ships with each other. It also demonstrated the model's competence in discerning the vessels' sign from the artificial structures from littoral regions, such as harbor jetties, minor islands and sea clutters. As seen in Figures 6-1 (d) and (e), training data from AIS annotation demonstrated substantially high performance compared to that from visual interpretation. In addition, ambiguous signals in the vicinity of strong backscattering objects can cause performance to plummet in ship detection, as demonstrated in Figure 6-1 (h). The azimuth ambiguity ghost signals with similar but weaker signals than the main signal never included AIS information and were

disregarded by AIS-based annotation training database. As the detection results in Figure 6-1(g) suggest, the detector could effectively evade such signals from detection. Eventually, by implementing AIS information and SAR images with wide coverage, this study managed to construct a database both verified via referenced information and a significant quantity containing more than 7000 ship chips from SAR images. This study therefore could apply this database as a training data, unlike the conventional ship detection training data of which the number was often less than or approximately one hundred [23, 82, 85]. Owing to the quantity of training data, the results in Table 6-2 and Figure 6-1 were regarded as robust and image-independent. The ship detection study revealed that acquiring training data for CNN-based object detection algorithm could be achieved without any mediation of manual and artificial procedures.

## **6.2 Application on Determining Unclassified Vessels**

As transmittance of AIS and VPASS information to the ground station is compulsory for ships over 50 tons in the vicinity of littoral regions [39], ships whose AIS and VPASS data are not acquired from the station could be regarded as unclassified. This section is intended to propose a supplementary algorithm which could effectively discern unclassified vessels in the SAR coverage implementing the detection results introduced in Chapter 5. The preliminary pursuit of merging the two different datasets of AIS and satellite image data was previously conducted [86], which overlapped the ship detection results with AIS information. The conventional determination algorithm from [86] derived the detection results from CFAR detector and subsequently implemented a brief operation of AIS interpolation and matching. The dissertation proposed a sophisticated algorithm for matching ships in the SAR image with AIS information; it would be possible to derive an ameliorated algorithm for unclassified vessel determination for both AIS and VPASS information. In this section, it could be applied to sort out unclassified vessels, ships and fishing boats, from the detection results.

Determination of each unclassified vessel could only be demonstrated on accurately detected vessels. In the case of AIS-based ship detection from Table 5-1, three SAR images of which the usages were testing, acquired on 26/06/2018, 08/07/2018 and 20/07/2018 were implemented for such application. Respectively indicating 75.48%, 79.16% and 76.43% of overall detection in the F1 score, the

precisely detected ship was separately arranged from the gross prediction. Subsequently, dynamic AIS information corresponding to the temporal and spatial coverage of the target SAR image was referenced. It followed the identical procedure described in Figure 3-1; the specific procedure including AIS interpolation and Doppler frequency shift correction. As all AIS signals were arranged to appropriate position, bounding boxes were established from the AIS positions while assigning those positions as the center of the rectangular bounding box. Comparing the AIS-based bounding box with every accurate prediction of the ship, prediction without any superposition of AIS information could be regarded as ships that lack AIS transmittance to the ground station.

The algorithm elaborating this section is described as Figure 6-2, indicating the comparison between real-time information of ship and prediction results. The proportion of unclassified vessels over the precise ship detection is presented in Table 6-1 for three SAR images, where Figure 6-3 demonstrates the typical determination indicating unclassified ships as red and the others as green. Among the three Sentinel-1 SAR images in Table 6-1, the proportion of unclassified ships reached 15%, regardless of their location in inshore and offshore. Given the regulation on AIS attachment on middle to large vessels [39], these 15% ships are unclassified and could be penalized by the respective legislations.

An identical algorithm was implemented for the VPASS-based fishing boat detection by substituting the dynamic AIS information with dynamic VPASS information. Following the procedure conducted in Chapter 3, dynamic VPASS information was interpolated and Doppler shift-corrected, followed by the

construction of bounding box for comparison. After sorting out the defective detections, the remaining output would indicate the accurate detection results of fishing boats. Figure 6-4 and Table 6-1 additionally elaborates the determination of fishing boats from two Cosmo-SkyMed SAR images acquired on 10/03/2018 and 13/05/2018; it revealed that the majority of fishing boats extinguished the VPASS signals while maneuvering in coastal regions. Given the large output difference between the AIS-attached ship and VPASS-attached fishing boats, it could be assumed that the large-scaled vessels tended to strictly adhere to the attachment regulation.



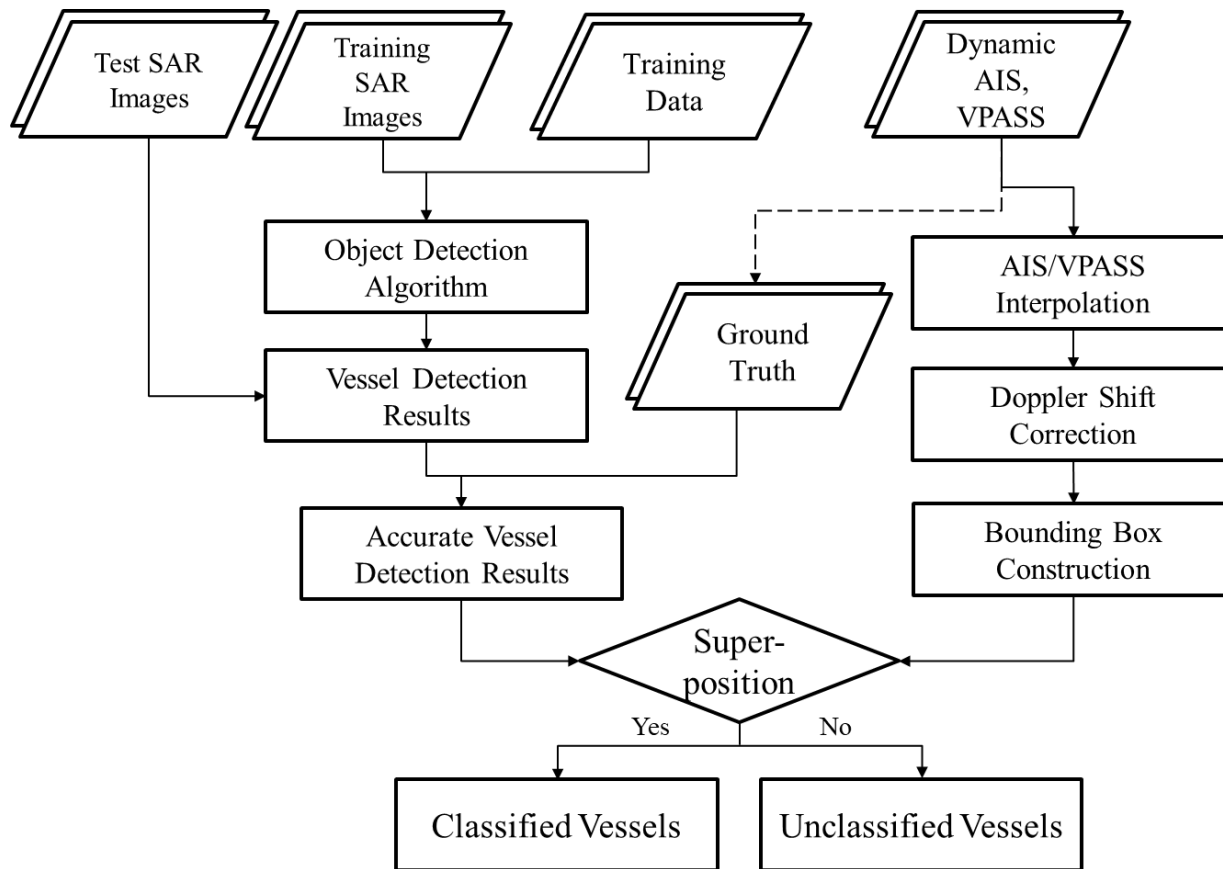


**Figure 6-2 Flowchart of discrimination of unclassified vessels from vessel detection results and dynamic AIS and VPASS information.**

With the advent of machine learning applications on satellite imagery, this proposed technique could have considerable effects on real-time monitoring of ships in different aspect. Conventional usage of real-time ship surveillance highly relied on information from the target itself, including AIS and VPASS information. Surveillance of targets via information sent from those very targets could be challenging when facing the lack of information. Moreover, as AIS and VPASS information is transferred to the ground station in discrete, numerical manner, an intrinsic impediment keeping the user from intuitive comprehension on the distribution of the data exists. In contrast, ship detection on SAR imagery could be appropriate for long-term monitoring on trade or inaccessible harbors owing to its wide coverage and periodic acquisition. Implementing SAR images, especially satellite SAR however, could be regarded as improper for real-time and high-speed monitoring of ships because the SAR data is not procured by an hourly basis.

The consecutive algorithms proposed in this dissertation could be practical in sorting out unclassified ships in both coastal and seaward regions when concurrently implemented with rapidly-obtained SAR imagery. On such SAR images, a machine learning based ship detection algorithm using the training data retrieved from the algorithm in Figures 3-1, 3-12 and 3-13 would effectively be able to detect and visualize the ships inside the image coverage. After the detections are completed, by comparing the output with AIS or VPASS information via the algorithm of Figure 6-2, unclassified vessels could be sorted out.

The application would be applicable illegal fishing surveillance by expeditiously acquired airborne SAR image, where the targets are smaller than other vessel types

and demands an expeditious response. When accompanied by (i) rapidly acquired satellite or airborne SAR image data, (ii) vessel detection output with higher accuracy and (iii) precise information on position and velocity of each vessel, it would be possible to establish a real-time module for an illegal vessel monitoring system.

**Table 6-1 Determination of unclassified vessels on SAR images for testing.**

Satellite Dataset	Acquisition Date	Accurate Detection	Illegal Ships	Proportion of Illegality (%)
	<b>Overall</b>	<b>977</b>	<b>140</b>	<b>14.33</b>
Sentinel-1	26/06/2018	319	35	12.87
	08/07/2018	341	54	15.84
	20/07/2018	317	51	16.09
	<b>Overall</b>	<b>803</b>	<b>675</b>	<b>84.06</b>
Cosmo-SkyMed	10/03/2018	346	310	89.60
	13/05/2018	457	365	79.87

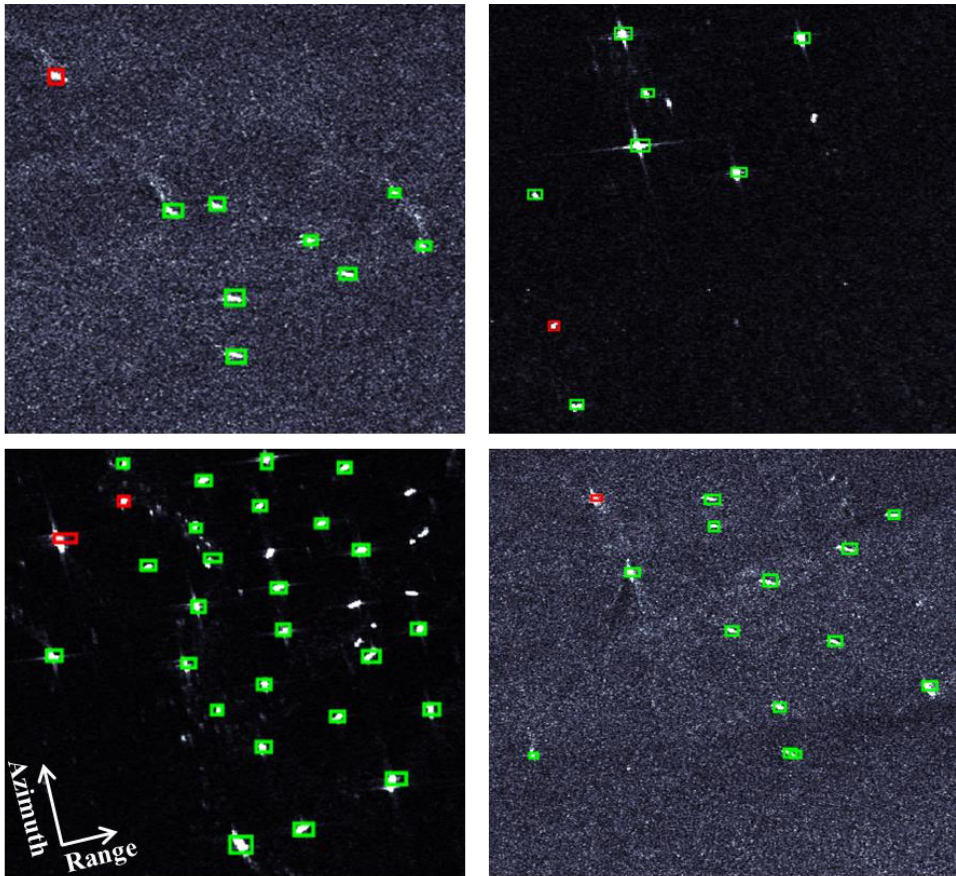


**Figure 6-3 Typical examples of determination of unclassified ships from Sentinel-1 SAR images.**

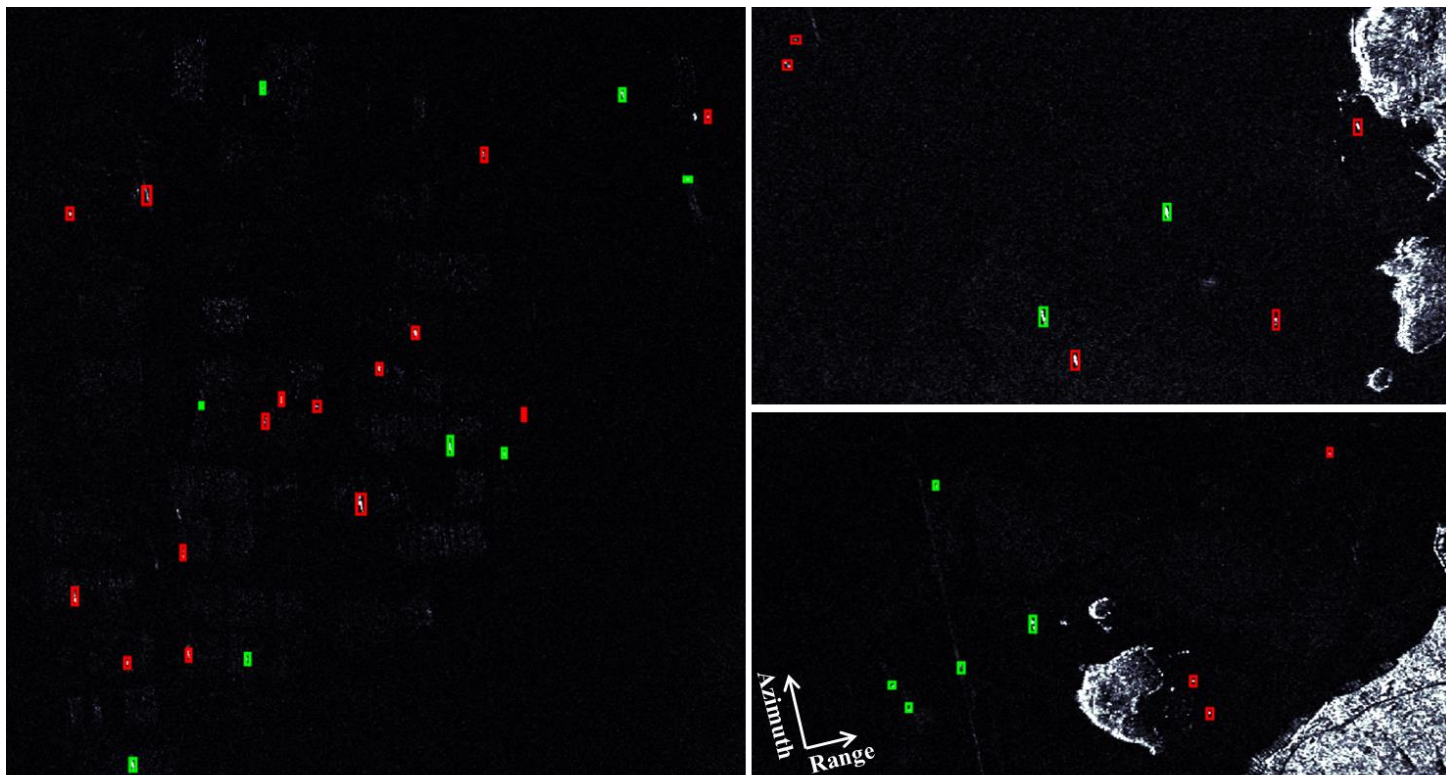


**Figure 6-4 Typical examples of determination of unclassified fishing boats from Cosmo-SkyMed SAR images.**

## **Chapter 7.**

### **Conclusion**

Monitoring vessels in the ocean using different methods was regarded as essential for preservation of maritime resources; implementation of individual equipment presented several limitations. As a mitigation, this study proposed and implemented an automated algorithm for acquiring training data from SAR images using AIS and VPASS information to reduce the interference from artificial interpretation and appropriately applied the proposed algorithm to ship detection. This automated algorithm contains the methodology of (i) precise interpolation of AIS and VPASS information, including an explicit algorithm of target interpolation time determination and minimization of the measurement error via a Kalman filter, (ii) Doppler frequency shift calibration by an accurate measurement of the slant range between the target vessel and the satellite, and (iii) direct acquisition of training data from the interpolated position from static AIS information, which could be substituted by binarization in case of implementing VPASS information. Bounding box expansion and DEM-masking was conducted in order to remedy the rounding from each vessel and eradicate the false ground signals. Subsequent differentiation of fishing boats in ground truth images was conducted by comparing scattering characteristics between the fishing boat candidates and fishing boats from VPASS signals, which were categorized in the database.

For AIS-based ship detection, applying the conventional CNN-based object

detection algorithm, 21 Sentinel-1 SAR images in the vicinity of the southeastern Korean peninsula were implemented. The model trained via 18 SAR images containing 7489 training data was tested with the other three images, obtaining an overall detection performance of 77.13%, as harmonic mean of precision and recall. For VPASS-based fishing boat detection, identical architecture was implemented to seven Cosmo-SkyMed SAR images for training and the two SAR images for testing; an overall detection performance of 58.35% was obtained.

Both detection results were applied to AIS and VPASS information for determination of unclassified ships and fishing boats given that the legal vessels were required to activate their respective sensors. Applying a superposition between the vessel detection output and AIS or VPASS information corresponding to the detection, the non-transmitting vessels were determined. This methodology determined that the fishing boats had significant chances of extinguishing the sensors while operating compared to that of ships. For robust and stable algorithmic construction of unclassified vessel discrimination, amelioration of detection accuracy and mitigation of efficiency of the determining unclassified ships and fishing boats is required.

Nevertheless, this study has a few limitations with regard to constructing ground truth data for fishing boat detection. It would be necessary to render a logically undeniable procedure for additional ground truth annotation methodology based on each boat's scattering characteristics. In the future, a study where the training data is directly procured from simulation of the target fishing boat could be pursued. If successfully implemented, it could fundamentally remove of the dependence on



both quantity and quality of training data in SAR image-based fishing boat detection. Last but not least, both AIS information and VPASS information could be implemented in a single SAR target image. A part of AIS data contains information from fishing ships; a combined vessel detection method based on two information datasets could be effective in advancing detection performance.

## 국문 요약문

전천후 지구 관측 위성인 SAR를 통한 선박 탐지는 해양 자원의 확보와 해상 안전 보장에 매우 중요한 역할을 한다. 기계 학습 기법의 도입으로 인해 선박을 비롯한 사물 탐지의 정확도 및 효율성이 향상되었으나, 이와 관련된 다수의 연구는 탐지 알고리즘의 개량에 집중되었다. 그러나, 탐지 정확도의 근본적인 향상은 정밀하게 취득된 대량의 훈련자료 없이는 불가능하기에, 본 연구에서는 선박의 실시간 위치, 속도 정보인 AIS 자료를 이용하여 인공 지능 기반의 선박 탐지 알고리즘에 사용될 훈련자료를 자동적으로 취득하는 알고리즘을 제안하였다.

이를 위해 이산적인 AIS 자료를 SAR 영상의 취득시각에 맞추어 정확하게 보간하고, AIS 센서 자체가 가지는 오차를 최소화하였다. 또한, 이동하는 산란체의 시선 속도로 인해 발생하는 도플러 편이 효과를 보정하기 위해 SAR 위성의 상태 벡터를 이용하여 위성과 산란체 사이의 거리를 정밀하게 계산하였다. 이렇게 계산된 AIS 센서의 영상 내의 위치로부터 선박 내 AIS 센서의 배치를 고려하여 선박 탐지 알고리즘의 훈련자료 형식에 맞추어 훈련자료를 취득하고, 어선에 대한 위치, 속도 정보인 VPASS 자료 역시 유사한 방법으로 가공하여 훈련자료를 취득하였다.

AIS 자료로부터 취득한 훈련자료는 기존 방법대로 수동 취득한 훈련자료와 함께 인공 지능 기반 사물 탐지 알고리즘을 통해 정확도를 평가하였다. 그 결과, 제시된 알고리즘으로 취득한 훈련 자료는 수동 취득한 훈련 자료 대비 더 높은 탐지 정확도를 보였으며, 이는 기존의 사물 탐지 알고리즘의 평가 지표인 정밀도, 재현율과 F1 score를 통해 진행되었다. 본 연구에서 제안한 훈련자료 자동 취득 기법으로 얻은 선박에 대한 훈련자료는 특히 기존의 선박 탐지 기법으로는 분별이 어려웠던 항만에 인접한 선박과 산란체 주변의 신호에 대한 정확한 분별 결과를 보였다. 본 연구에서는 이와 함께, 선박 탐지 결과와 해당 지역에 대한 AIS 및 VPASS 자료를 이용하여 선박의 미식별성을 판정할 수 있는 가능성 또한 제시하였다.

**주요어** : SAR, AIS, VPASS, Training data, Machine learning, Vessel detection

## Bibliography

- [1] Y. Wang, Z. Zhang, N. Li, F. Hong, H. Fan, X. Wang, "Maritime Surveillance with Undersampled SAR," *IEEE Geoscience and Remote Sensing Letters*, vol. 14, no. 8, pp. 1423-1427, 2017.
- [2] D. J. Crisp, *The State-of-the-Art in Ship Detection in Synthetic Aperture Radar Imagery*. Edinburgh, South Australia, 2004, pp. 2165-2168.
- [3] Z. Zhao, K. Ji, X. Xing, H. Zou, S. Zhou, "Ship Surveillance by Intergration of Space-Borne SAR and AIS-Review of Current Research," *Journal of Navigation*, vol. 67, pp. 177-189, 2013.
- [4] R. Pelich, N. Longép  , G. Mercier, G. Hajduch, R. Garello, "AIS-Based Evaluation of Target Detectors and SAR Sensors Characteristics for Maritime Surveillance," *IEEE Journal of Selected Topics on Applied Earth Observations and Remote Sensing*, vol. 8, no. 8, pp. 3892-3901, 2015.
- [5] P. W. Vachon, J. W. M. Campbell, C. A. Bjerkelund, F. W. Dobson, M. T. Rey, "Ship Detection by the RADARSAT SAR: Validation of Detection Model Predictions," *Canadian Journal of Remote Sensing*, vol. 23, no. 1, pp. 48-59, 1997.
- [6] Q. Li, L. Mou, Q. Liu, Y. Wang, X. Zhu, "HSF-Net: Multiscale Deep Feature Embedding for Ship Detection in Optical Remote Sensing Imagery," *IEEE Transactions on Geoscience and Remote Sensing*, vol. 56, pp. 7147-7161, 2018.
- [7] I. G. Cumming, F. H. Wong, *Digital Processing of Synthetic Aperture Radar Data: Algorithms and Implementation*. Norwood, MA, USA: Artech House, 2005.
- [8] S. Soumekh, *Synthetic Aperture Radar Signal Processing with MATLAB Algorithms*. New York, NY: John Wiley & Sons, Inc, 1999.
- [9] H. Li, W. Perrie, Y. He, S. Lehner, S. Brusch, "Target Detection on the Ocean with the Relative Phase of Compact Polarimetry SAR," *IEEE Transactions on Geoscience and Remote Sensing*, vol. 51, no. 6, pp. 3299-3305, 2013.
- [10] M. Jeremy, J. W. M. Campbell, K. Matter, T. Potter "Ocean Surveillance with Polarimetric SAR " *Canadian Journal of Remote Sensing*, vol. 27, no. 4, pp. 328-344, 2001.

- [11] K. Eldhuset, "An Automatic Ship and Ship Wake Detection System for Spaceborne SAR Images in Coastal Regions," *IEEE Transactions on Geoscience and Remote Sensing*, vol. 34, no. 4, pp. 1010-1019, 1996.
- [12] L. Hongbo, S. Yiyang, L. Yongtan, "Estimation of Detection Threshold in Multiple Ship Target Situations with HF Ground Wave Radar," *Journal of Systems Engineering and Electronics*, vol. 18, no. 4, pp. 739-744, 2007.
- [13] W. C. Morchin, *Airborne Early Warning Radar*. Boston, MA, USA: Artech House Inc, 1990.
- [14] J. Zhu, X. Qiu, Z. Pan, Y. Zhang, B. Lei, "An Improved Shape Contexts Based Ship Classifications in SAR Images," *Remote Sensing*, vol. 9, no. 2, p. 145, 2017.
- [15] A. Marino, M. J. Sanjuan-Ferrar, I. Hajnsek, K. Oushi, "Ship Detection with Spectral Analysis of SAR: A Comparison of New and Well-Known Algorithms," *Remote Sensing*, vol. 7, no. 5, pp. 5416-5439, 2015.
- [16] M. Jiang, X. Yang, Z. Dong, S. Fang, J. Meng, "Ship Classification Based on Superstructure Scattering Features in SAR Images," *IEEE Geoscience and Remote Sensing Letters*, vol. 13, no. 5, pp. 616-620, 2016.
- [17] G. Margarit, J. J. Mallorqui, J. Fortuny-Guasch, C. Lopez-Martinez, "Phenomenological Vessel Scattering Study Based on Simulated Inverse SAR Imagery," *IEEE Transactions on Geoscience and Remote Sensing*, vol. 47, no. 4, pp. 1212-1223, 2009.
- [18] G. Margarit, A. Tabasco, "Ship Classification in Single-Pol SAR Images Based on Fuzzy Logic," *IEEE Transactions on Geoscience and Remote Sensing*, vol. 49, no. 8, pp. 3129-3138, 2011.
- [19] W. B. Silva, C. C. Freitas, S. J. S. Sant'Anna, A. C. Frery, "Classification of Segments in PolSAR Imagery by Minimum Stochastic Distances Between Wishart Distributions," *IEEE Journal of Selected Topics on Applied Earth Observations and Remote Sensing*, vol. 6, no. 3, pp. 1263-1273, 2013.
- [20] G. E. Atteia, M. J. Collins, "On the Use of Compact Polarimetry SAR for Ship Detection," *ISPRS Journal of Photogrammetry and Remote Sensing*, vol. 80, pp. 1-9, 2013.
- [21] D. Velotto, F. Nunziata, M. Migliaccio, S. Lehner, "Dual-Polarimetric TerraSAR-X SAR Data for Target at Sea Observation," *IEEE Geoscience and Remote Sensing Letters*, vol. 10, no. 5, pp. 1114-1118, 2013.

- [22] T. Zhang, J. Ji, X. Li, W. Yu, H. Xiong, "Ship Detection From PolSAR Imagery Using the Complete Polarimetric Covariance Difference Matrix," *IEEE Transactions on Geoscience and Remote Sensing*, vol. 57, no. 5, pp. 2824-2839, 2019.
- [23] J. Hwang, H. Jung, "Automatic Ship Detection Using the ANN and SVM from X-band SAR Satellite Images," *Remote Sensing*, vol. 10, no. 2, p. 1799, 2018.
- [24] S. K. Joshi, S. V. Baumgartner, A. B. C. da Silva, G. Krieger, "Range-Doppler Based CFAR Ship Detection with Automatic Training Data Selection," *Remote Sensing*, vol. 11, no. 11, p. 1270, 2019.
- [25] J. Ai, X. Yang, F. Zhou, Z. Dong, L. Jia, H. Yan, "A Correlation-Based Joint CFAR Detector Using Adaptively-Truncated Statistics in SAR Imagery," *Sensors*, vol. 17, no. 4, p. 686, 2017.
- [26] J. Hwang, S. Chae, D. Kim, H. Jung, "Application of Artificial Neural Networks to Ship Detection from X-Band Kompsat-5 Imagery," *Applied Sciences*, vol. 7, no. 9, p. 961, 2017.
- [27] K. He, X. Zhang, S. Ren, J. Sun, "Deep Residual Learning for Image Recognition," presented at the IEEE Conference on Computer Vision and Pattern Recognition, Las Vegas, NV, USA, 2016.
- [28] Y. Huang, J. Xu, Q. Wu, Z. Zheng, Z. Zhang, J. Zhang, "Multi-Pseudo Regularized Label for Generated Data in Person Re-Identification," *IEEE Transactions on Geoscience and Remote Sensing*, vol. 28, no. 3, pp. 1391-1403, 2019.
- [29] Z. Lin, K. Ji, X. Leng, G. Kuang, "Squeeze and Excitation Rank Faster R-CNN for Ship Detection in SAR Images," *IEEE Geoscience and Remote Sensing Letters*, vol. 16, no. 5, pp. 751-755, 2019.
- [30] T. Zhang, X. Zhang, "High-Speed Ship Detection in SAR Images Based on a Grid CNN," *Remote Sensing*, vol. 11, no. 10, p. 1206, 2019.
- [31] J. Wang, T. Zheng, P. Lei, X. Bai, "A Hierarchical CNN-Based Ship Target Detection Method in Spaceborne SAR Imagery," *Remote Sensing*, vol. 11, no. 6, p. 620, 2019.
- [32] A. Czapiewska, J. Sadowski, "Algorithms for Ship Movement Prediction for Location Data Compression," *The International Journal on Marine Navigation and Safety of Sea Transportation*, vol. 9, no. 1, pp. 75-81, 2015.

- [33] V.-S. Nguyen, N. Im, S. Lee, "The Interpolation Method for the Missing AIS Data of Ship," *Journal of Navigation and Port Research*, vol. 39, no. 5, pp. 377-384, 2015.
- [34] S. Brusch, S. Lehner, T. Fritz, M. Soccorsi, A. Soloviev, B. van Schie, "Ship Surveillance with TerraSAR-X," *IEEE Transactions on Geoscience and Remote Sensing*, vol. 49, no. 3, pp. 1092-1103, 2011.
- [35] Y. Xu, H. Lang, L. Niu, C. Ge, "Discriminative Adaptation Regularization Framework-Based Transfer Learning for Ship Classification in SAR Images," *IEEE Geoscience and Remote Sensing Letters*, vol. 16, no. 11, pp. 1-5, 2019.
- [36] H. Lang, H. Wu, Y. Xu, "Ship Classification in SAR Images Improved by AIS Knowledge Transfer," *IEEE Geoscience and Remote Sensing Letters*, vol. 15, no. 3, pp. 439-443, 2018.
- [37] M. D. Graziano, A. Renga, A. Moccia, "Integration of Automatic Identification System (AIS) Data and Single-Channel Synthetic Aperture Radar (SAR) Images by SAR-Based Ship Velocity Estimation for Maritime Situational Awareness," *Remote Sensing*, vol. 11, no. 19, p. 2196, 2019.
- [38] L. Huang, B. Liu, B. Li, W. Guo, W. Yu, Z. Zhang, W. Yu, "OpenSARShip: A Dataset Dedicated to Sentinel-1 Ship Interpretation," *IEEE Journal of Selected Topics on Applied Earth Observations and Remote Sensing*, vol. 11, no. 1, pp. 195-208, 2018.
- [39] *Vessel Facility Standard*, K. Ministry of Ocean and Fisheries 108, 2014.
- [40] *Public Notice on the Installation Criteria and Operation of VPASS Device*, K. C. Guard 3-6, 2017.
- [41] P. Capaldo, F. Fratarcangeli, A. Nascetti, A. Manzoni, M. Porfiri, M. Crespi, "Centimeter Range Measurement Using Amplitude Data of TerraSAR-X Imagery," in *Proceedings of the ISPRS Commission VII Symposium*, Istanbul, Turkey, 2014, pp. 55-61.
- [42] P. Guccione, M. Scagliola, D. Giudici, "Low-Frequency SAR Radiometric Calibration and Antenna Pattern Estimation by Using Stable Point Targets," *IEEE Transactions on Geoscience and Remote Sensing*, vol. 56, no. 2, pp. 635-646, 2018.
- [43] T. M. Lillesand, R. W. Kiefer, J. W. Chipman, *Remote Sensing and Image Interpretation*, 7 ed. John Wiley & Sons, 2015.

- [44] S. K. Chaturvedi, C.-S. Yang, K. Ouchi, P. Shanmugan, "Ship Recognition by Integration of SAR and AIS," *The Journal of Navigation*, vol. 65, no. 2, pp. 323-337, 2012.
- [45] D. Simon, "Kalman Filtering with State Constraints: A Survey of Linear and Nonlinear Algorithms," *IET Control Theory and Applications*, vol. 4, no. 8, pp. 1303-1318, 2010.
- [46] C. Antoniou, M. Ben-Akiva, H. N. Koutsopoulos, "Nonlinear Kalman Filtering Algorithms for On-Line Calibration of Dynamic Traffic Assignment Models," *IEEE Transactions on Intelligent Transportation Systems*, vol. 8, no. 4, pp. 661-670, 2007.
- [47] C. P. I. J. van Hinsbergen, T. Schreiter, F. S. Zuurbier, J. W. C. van Lint, h. J. van Zuylen, "Localized Extended Kalman Filter for Scalable Real-Time Traffic State Estimation," *IEEE Transactions on Intelligent Transportation Systems*, vol. 13, no. 1, pp. 385-394, 2012.
- [48] Y. Li, S. O'Young, "Kalman Filter Disciplined Phase Gradient Autofocus for Stripmap SAR," *IEEE Transactions on Geoscience and Remote Sensing*, vol. 58, no. 9, pp. 6298-6308, 2020.
- [49] K. Jaskolski, "AIS Dynamic Data Estimation Based on Discrete Kalman Filter Algorithm," *Scientific Journal of Polish Naval Academy*, vol. 4, no. 211, pp. 71-87, 2017.
- [50] G. Li, J. Xu, Y.-N. Peng, X.-G. Xia, "Location and Imageing of Moving targets Using Nonuniform Linear Antenna Array SAR," *IEEE Transactions on Aerospace and Electronic Systems*, vol. 43, no. 3, pp. 1214-1220, 2007.
- [51] G. Li, J. Xu, Y.-N. Peng, X.-G. Xia, "Bistatic Linear Antenna Array SAR for Moving Target Detection, Location and Imaging with Two Passive Airborne Radars," *IEEE Transactions on Geoscience and Remote Sensing*, vol. 45, no. 3, pp. 554-565, 2007.
- [52] Z.-Z. Huang, Z.-G. Ding, J. Xu, T. Zeng, L. Liu, Z.-R. Wang, C.-H. Feng, "Azimuth Location Deambiguity for SAR Ground Moving Targets via Coprime Adjacent Arrays," *IEEE Journal of Selected Topics on Applied Earth Observations and Remote Sensing*, vol. 11, no. 2, pp. 551-561, 2018.
- [53] J. Xu, Z.-Z. Huang, Z.-R. Wang, Z.-R. Wang, L. Xiao, X.-G. Xia, T. Long, "Radial Velocity Retrieval for Multichannel SAR Moving Targets with Time-Space Doppler Deambiguity," *IEEE Transactions on Geoscience and Remote Sensing*, vol. 56, no. 1, pp. 35-48, 2018.



- [54] J. Xu, Y. Zuo, B. Xia, X-G. Xia, Y.-N. Peng, Y.-L. Wang, "Ground Moving Target Signal Analysis in Complex Image Domain for Multichannel SAR," *IEEE Transactions on Geoscience and Remote Sensing*, vol. 50, no. 2, pp. 538-552, 2012.
- [55] M. A. Sletten, L. Rosenberg, S. Menk, J. V. Toporkov, R. W. Jasen, "Maritime Signature Correction with the NRL Multichannel SAR," *IEEE Transactions on Geoscience and Remote Sensing*, vol. 54, no. 11, pp. 6783-6790, 2016.
- [56] S. V. Baumgartner, G. Krieger, "Simultaneous High-Resolution Wide-Swath SAR Imaging and Ground Moving Target Indication: Processing Approaches and System Concepts," *IEEE Journal of Selected Topics on Applied Earth Observations and Remote Sensing*, vol. 8, no. 11, pp. 5015-5029, 2015.
- [57] P. W. Vachon, J. W. M. Campbell, A. L. Gray, F. W. Dobson, "Validation of Along-Track Interferometric SAR Measurements of Ocean Surface Waves," *IEEE Transactions on Geoscience and Remote Sensing*, vol. 37, no. 1, pp. 150-162, 1999.
- [58] D.-J. Kim, W. M. Moon, D. Moller, D. A. Imel, "Measurements of Ocean Surface Waves and Currents Using L- and C-Band Along-Track Interferometric SAR," *IEEE Transactions on Geoscience and Remote Sensing*, vol. 41, no. 12, pp. 2821-2832, 2003.
- [59] O. Montenbruck, "An Epoch State Filter for Use with Analytical Orbit Models of Low Earth Satellites," *Aerospace Science and Technology*, vol. 4, no. 4, pp. 277-287, 2000.
- [60] P. Sengupta, S. R. Vadali, K. T. Alfriend, "Satellite Orbit Design and Maintenance for Terrestrial Coverage," *Journal of Spacecraft and Rockets*, vol. 47, no. 1, pp. 177-187, 2010.
- [61] A. Hanafi, M. Karim, E.-K. Hachem, T. Rachidi, M. Sahmoudi, "Perturbation Effects in Orbital Element of CubeSats," presented at the 3rd International Conference on Advanced Technologies for Signal and Image Processing Fez, Morocco, 22-24 May 2017, 2017.
- [62] H. Min, Z. Guoqiang, S. Junling, "Optimal Collision Avoidance Maneuver for Formation Flying Satellites Using Relative Orbital Elements," in *International Conference on Mechatronics and Automation*, Xi'an, China, 4-7 Aug 2010 2010: IEEE.
- [63] R. Touzi, "On the Use of Polatimetric SAR Data for Ship Detection," in

*IEEE International Geoscience and Remote Sensing Symposium*, Hamburg, Germany, 28 June-2 July 1999 1999: IEEE.

- [64] G. Gao, "A Parzen-Window-Kernel-Based CFAR Algorithm for Ship Detection in SAR Images," *IEEE Geoscience and Remote Sensing Letters*, vol. 8, no. 3, pp. 557-561, 2010.
- [65] X. Zhou, C. Yao, H. Wen, Y. Wang, S. Zhou, W. He, J. Liang, "EAST: An Efficient and Accurate Scene Text Detector," presented at the IEEE Conference on Computer Vision and Pattern Recognition, Honolulu, HI, USA, 2017.
- [66] G. Lin, W. Shen, "Research on Convolutional Neural Network Based on Improved ReLU Piecewise Activation Function," *Procedia Computer Science*, vol. 131, pp. 977-984, 2018.
- [67] N. Srivastava, G. Hinton, A. Krizhevsky, I. Sutskever, R. Salakhutdinov, "Dropout: A Simple Way to Prevent Neural Networks from Overfitting," *The Journal of Machine Learning Research*, vol. 15, no. 1, pp. 1929-1958, 2014.
- [68] A. Krizhevsky, I. Sutskever, G. E. Hinton, "ImageNet Classification with Deep Convolutional Neural Networks," *Advances in Neural Information Processing Systems*, vol. 25, pp. 1097-1105, 2012.
- [69] J. Redmon, S. Divvala, R. Girshick, A. Farhadi, "You Only Look Once: Unified, Real-Time Object Detection," in *IEEE Conference on Computer Vision and Pattern Recognition*, Las Vegas, NV, USA, 2016: IEEE, pp. 779-788.
- [70] Y. Sun, W. Zuo, M. Liu, "RTFNet: RGB-Thermal Fusion Network for Semantic Segmentation of Urban Scenes," *IEEE Robotics and Automation Letters*, vol. 4, no. 3, pp. 2576-2583, 2019.
- [71] S. Gidaris, N. Komodakis, "Locnet: Improving Localization Accuracy for Object Detection," presented at the IEEE Conference on Computer Vision and Pattern Recognition, Las Vegas, NV, USA, 2016.
- [72] M. Gordon, M. Kochen, "Recall-precision Trade-off: A Derivation," *Journal of the American Society for Information Science*, vol. 40, no. 3, pp. 145-151, 1989.
- [73] Q. Zhang, I. Couloigner, "Accurate Centerline Detection and Line Width Estimation of Thick Lines Using the Radon Transform," *IEEE Transactions on Image Processing*, vol. 16, no. 2, pp. 310-316, 2007.

- [74] K. Kang, D.-J. Kim, "Ship Velocity Estimation from Ship Wakes Detected Using Convolutional Neural Networks," *IEEE Journal of Selected Topics on Applied Earth Observations and Remote Sensing*, vol. 12, no. 11, pp. 4379-4388, 2019.
- [75] W. Li, Y. Huang, J. Yang, J. Wu, L. Kong, "An Improved Radon-Transform-Based Scheme of Doppler Centroid Estimation for Bistatic Forward-Looking SAR," *IEEE Geoscience and Remote Sensing Letters*, vol. 8, no. 2, pp. 379-383, 2011.
- [76] F. Biondi, "A Polarimetric Extension of Low-Rank Plus Sparse Decomposition and Radon Transform for Ship Wake Detection in Synthetic Aperture Radar Images," *IEEE Geoscience and Remote Sensing Letters*, vol. 16, no. 1, pp. 75-79, 2019.
- [77] M. T. Rey, J. K. Tunaley, J. T. Folinsbee, P. A. Jahans, J. A. Dixon, M. R. Vent, "Application Of Radon Transform Techniques To Wake Detection In Seasat-A SAR Images," *IEEE Transactions on Geoscience and Remote Sensing*, vol. 28, no. 4, pp. 553-560, 1990.
- [78] Z. Wang, A. C. Bovik, H. R. Sheikh, E. P. Simoncelli, "Image Quality Assessment: From Error Visibility to Structural Similarity," *IEEE Transactions on Image Processing*, vol. 13, no. 4, pp. 600-612, 2004.
- [79] J.-S. Lee, J.-C. Chen, "A Single Scatter Model for X-ray CT Energy Spectrum Estimation and Polychromatic Reconstruction," *IEEE Transactions on Medical Imaging*, vol. 34, no. 6, pp. 1403-1413, 2015.
- [80] F. Zhu, D. R. Gonzalez, T. Carpenter, M. Atkinson, J. Wardlaw, "Lesion Area Detection Using Source Image Correlation Coefficient for CT Perfusion Imaging," *IEEE Journal of Biomedical and Health Informatics*, vol. 17, no. 5, pp. 950-958, 2013.
- [81] J. Ai, R. Tian, Q. Luo, J. Jin, B. Tang, "Multi-Scale Rotation-Invariant Haar-Like Feature Integrated CNN-Based Ship Detection Algorithm of Multi-Target Environment in SAR Imagery," *IEEE Transactions on Geoscience and Remote Sensing*, vol. 57, no. 12, pp. 10070-10087, 2019.
- [82] M. Ma, J. Chen, W. Liu, W. Yang, "Ship Classification and Detection Based on CNN Using GF-3 SAR Images," *Remote Sensing*, vol. 10, no. 12, p. 2043, 2018.
- [83] D. Velotto, C. Bentes, B. Tings, S. Lehner, "First Comparison of Sentinel-1 TerraSAR-X Data in the Framework of Maritime Targets Detection: South Italy Case," *IEEE Journal of Oceanic Engineering*, vol. 41, no. 4, pp. 993-

1006, 2016.

- [84] N. Longép , G. Hajduch, R. Ardianto, R. de Joux, B. Nhunfat, M. I. Marzuki, R. Fablet, I. Hermawan, O. Germain, B. A. Subki, R. Farhan, A. D. Muttaqin, P. Gaspar, "Completing Fishing Monitoring with Spaceborne Vessel Detection System (VDS) and Automatic Identification System (AIS) to Assess Illegal Fishing in Indonesia," *Marine Pollution Bulletin*, vol. 131, pp. 33-39, 2018.
- [85] X. Zhang, H. Wang, C. Xu, Y. Lv, C. Fu, H. Xiao, Y. He, "A Lightweight Feature Optimizing Network for Ship Detection in SAR Image," *IEEE Access*, vol. 7, pp. 141662-141678, 2019.
- [86] A. A. Kurekin, B. R. Loveday, O. Clements, G. D. Quartly, P. I. Miller, G. Wiafe, K. A. Agyekum, "Operational Monitoring of Illegal Fishing in Ghana through Exploitation of Satellite Earth Observation and AIS Data," *Remote Sensing*, vol. 11, no. 3, p. 293, 2019.